Nanoscale

ROYAL SOCIETY OF CHEMISTRY

REVIEW

View Article Online
View Journal | View Issue

Cite this: *Nanoscale*, 2025, **17**, 5526

Self-assembled inorganic nanomaterials for biomedical applications

Miguel T. Campos,[a,b,c,d] Laura S. Pires,[a,b] Fernão D. Magalhães,[a,b] Maria J. Oliveira[c,d] and Artur M. Pinto *[a,b,c,d]

Received 30th October 2024,
Accepted 10th January 2025

DOI: 10.1039/d4nr04537h

rsc.li/nanoscale

Controlled self-assembly of inorganic nanoparticles has the potential to generate complex nanostructures with distinctive properties. The advancement of more precise techniques empowers researchers in constructing and assembling diverse building blocks, marking a pivotal evolution in nanotechnology and biomedicine. This progress enables the creation of customizable biomaterials with unique characteristics and functions. This comprehensive review takes an innovative approach to explore the current state-of-the-art self-assembly methods and the key interactions driving the self-assembly processes and provides a range of examples of biomedical and therapeutic applications involving inorganic or hybrid nanoparticles and structures. Self-assembly methods applied to bionanomaterials are presented, ranging from commonly used methods in cancer phototherapy and drug delivery to emerging techniques in bioimaging and tissue engineering. The most promising *in vitro* and *in vivo* experimental results achieved thus far are presented. Additionally, the review engages in a discourse on safety and biocompatibility concerns related to inorganic self-assembled nanomaterials. Finally, opinions on future challenges and prospects anticipated in this evolving field are provided.

1. Introduction

As the global population ages, the incidence of cancer and other aging-related diseases becomes a growing concern.[1,2] Traditional cancer treatments such as chemotherapy, radiotherapy, and surgery can sometimes be not as effective as desired, especially in more advanced stages, or lead to side effects, with new alternative approaches being able to comp-

---

[a] *LEPABE, Faculdade de Engenharia, Universidade do Porto, Rua Roberto Frias, 4200-465 Porto, Portugal. E-mail: arturp@fe.up.pt*
[b] *ALiCE – Associate Laboratory in Chemical Engineering, Faculdade de Engenharia, Universidade do Porto, Portugal*
[c] *i3S – Instituto de Investigação e Inovação em Saúde, Universidade do Porto, Rua Alfredo Allen 208, Porto 4200-135, Portugal*
[d] *INEB – Instituto de Engenharia Biomédica, Universidade do Porto, Rua Alfredo Allen 208, Porto 4200-135, Portugal*

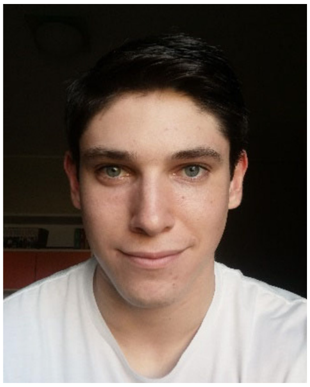

Miguel T. Campos

Miguel Campos graduated in Biomedical Engineering, obtaining his MSc degree from Faculty of Engineering – University of Porto (FEUP). He completed his BSc in Bioengineering at Catholic University of Porto, Portugal. Miguel is a Biomedical Engineering PhD Student at FEUP and at i3S – Institute for Research and Innovation in Health. His research activity is focused on new nanomaterials production and optimization of their properties for biomedical applications, including cancer photothermal therapy and drug delivery.

Laura S. Pires

Laura Pires is a MSc graduate in Micro and Nanotechnology Engineering from NOVA University of Lisbon, Portugal. Her research activity focuses on the development of nanomaterials aimed at biomedical applications. Her master's thesis culminated with the development of a conductive polymer-based scaffold aimed at the regeneration of peripheral nerves.

lement those and eventually provide a more selective targeted effect.[3–7] Inorganic nanoparticles are emerging as innovative, stimuli-responsive drug delivery systems in theranostics, bioimaging, photothermal and photodynamic therapy (PTT/PDT), and tissue engineering.[8,9] Notably, they offer the potential for precise tuning to deliver localized treatments that are more efficient and selective in targeting tumors and cancer cells while sparing healthy tissues.[10–12] These inorganic nanoparticles serve various roles, acting as agents for localized and selective drug delivery, as well as contributors to photothermal therapy (PTT), photodynamic therapy (PDT), or magnetic hyperthermia therapy for cancer treatment.[13–15] In bioimaging, inorganic nanoparticles enable the visualization of biological structures and processes, aiding diagnosis and disease treatment. Superparamagnetic, ferromagnetic, and paramagnetic inorganic nanoparticles function as strong T_2 MRI contrast agents. Likewise, they enhance the resolution in computed tomography (CT) and aid in other imaging techniques.[16,17] Leveraging the self-assembly of inorganic nanomaterials, more efficient drug delivery has been achieved with heightened spatial and temporal resolution in bioimaging, thus enhancing the precision of chemotherapy by delivering drugs specifically to the targeted tissues. Hybrid nanomaterials, modified with targeting factors, play a crucial role in achieving this precise specificity.[18,19] Beyond drug delivery and bioimaging, inorganic nanoparticles find applications in biomedical applications for tissue regeneration and biosensing.[8,20–24] Their versatility and adaptability position them as promising contributors to the advancement of therapeutic and diagnostic strategies in the evolving landscape of medical science.

Inorganic nanomaterials showcase a wide range of dimensions and geometrical configurations.[18,25] Zero-dimensional (0D) inorganic nanoparticles commonly exhibit spherical, pseudo-spherical, dodecahedral, tetrahedral, octahedral, or cubic shapes. One-dimensional (1D) inorganic nanoparticles take the form of nanotubes, nanoneedles, nanorods or nanowires, nanoshuttles, nanocapsules, or hollow structures. Two-dimensional (2D) inorganic nanoparticles adopt geometrical configurations such as round disks, hexagonal, triangular, or quadrangular plates or sheets, belts, mesoporous-hollow nanospheres, and hollow rings.[26] Three-dimensional (3D) inorganic nanomaterials include structures such as nanoporous powders, nanowire or nanotube bundles, and nanolayers, among others.[27]

0D nanomaterials encompass a variety of types, including inorganic fullerenes, quantum dots (QDs), magnetic nanoparticles (MNPs), noble metal nanoparticles, upconversion nanoparticles (UCNPs), and polymer dots (Pdots).[25] Inorganic fullerene nanoparticles can be synthesized by chemical or physical methods, with the latter involving the folding of inorganic materials (such as MoS_2, SnS_2, or $NiBr_2$) into hollow quasi-spherical shells, often exhibiting desirable UV-visible absorption.[28,29] Inorganic QDs typically consist of atoms from groups II-IV or III–V of the periodic table, with diameters ranging from 2 to 20 nm. Common examples include CdTe, CdSe, and InP, known for their unique optical properties and suitable for various biomedical applications, including bioimaging, biosensing, and phototherapy.[25] The nanoscale sizes of QDs facilitate molecular-level interactions with proteins and cellular membranes, enhancing cellular uptake and improving detection specificity and sensitivity.[30,31] Inorganic MNPs are composed of atoms and materials with high saturation magnetization, such as Fe, Co, Ni, Fe_3O_4, and $CoFe_2O_4$, among others. MNPs find applications in hyperthermia treatment, biosensing, and drug delivery.[25] Noble metal 0D nanoparticles have ultrafine structures with properties distinct from non-

Fernão D. Magalhães

Fernão D. Magalhães obtained his PhD in Chemical Engineering from University of Massachusetts at Amherst, USA, in 1997. He is currently Associate Professor at FEUP, and Director of the Bachelor and the Master in Chemical Engineering programs. He is also the Director of the ARCP Collaborative Laboratory. His research interests include graphene-based materials for biomedical applications, high-performance coatings, and synthetic and natural adhesives for wood and cork-based composites. A large part of his research work is done in the context of industry-driven processes. He teaches classes on Polymer Materials, Process Control, and Industrial Automation.

Maria J. Oliveira

Maria José Oliveira is Principal Researcher, Coordinator of the Tumor and Microenvironment Interactions Group at i3S – Institute for Research and Innovation in Health, and Associated Invited Professor at the Institute Biomedical Sciences Abel Salazar, University of Porto. Her group is currently focused at understanding the role of the tumor microenvironment, particularly of immune cells, adipocytes and extracellular matrix components, on the modulation of cancer cell invasion and metastasis. Conversely, they are also dedicated at understanding how cancer cells modulate the microenvironment, sustaining invasion and escaping the immune surveillance, and foresee translational applications by identifying novel targets and designing more efficient therapies.

noble metals. Noble metal nanoparticles have been utilized in various biomedical applications, with silver and gold nanoparticles being among the most common. These materials share characteristics including ease of functionalization, enhanced scattering, efficient light absorption, and diameters ranging from 2 to 20 nm.[25]

Nanotubes constitute a significant class of 1D nanomaterials, characterized by hollow formations with the potential for single or multiple layers and diameters spanning 1 to 100 nm. The thickness of these nanotubes depends upon the number of layers assembled, ranging from a few nanometers to micrometers. Their distinctive shape, amphiphilic surface (if functionalized), and diminutive size afford them the capability to traverse biological membranes or barriers.[29,32] Carbon or oxide metals are frequently employed as primary building blocks during synthesis. Structures commonly investigated for biomedical applications include nanorods, nanowires, and nanofibers.[27] Inorganic nanorods, a well-explored studied subset of 1D nanostructures, can be composed of both metallic and non-metallic materials, such as carbon, zinc oxide, gold, or copper. Various synthetic methods exist for forming nanorods, where lengths between 10 to 120 nm are achieved.[33] The extensive utilization of 1D nanostructures in diverse biomedical applications, such as tissue engineering, wound healing, photothermal therapy, and photodynamic therapy, underscores their significance.[20]

Graphene and other two-dimensional nanomaterials (2DnMat), including black phosphorus, transition metal carbides, nitrides and carbonitrides (MXenes), transition metal dichalcogenides (TMDs), among others, have garnered increased attention in the biomedical field.[34,35] The nanoscale properties of these materials deviate from their bulk counterparts, primarily due to the high volume-to-surface ratios observed on smaller scales. These higher volume-to-surface ratios facilitate easier surface functionalization, which, in turn, stabilizes the nanomaterials under physiological conditions, enhances their biocompatibility, and improves their photothermal conversion ability. The bandgap of 2DnMat is layer-dependent, allowing for the fine-tuning of radiation absorption to meet specific application requirements.[35,36] The fabrication of 2DnMat for bioapplications primarily employs top-down methods, with liquid-phase exfoliation (LPE) being the most successful among them. Nevertheless, bottom-up techniques, particularly self-assembly, have also been reported for the production of these materials. LPE stands out for its adaptability, cost-effectiveness, and scalability potential. Operating conditions are easily achievable, as they do not necessitate high pressures or temperatures, making it particularly suitable for producing exfoliated 2DnMat sheets in a liquid medium.[36–38] Over the years, various techniques have been developed to improve the efficiency of LPE in different settings, such as exfoliation *via* sonication, high-shear mixing, or microfluidization.[38]

3D nanomaterials include powders and polycrystalline materials, often arising from the assembly of 0D, 1D, or 2D nanomaterials that establish contact with each other, forming interfaces and giving rise to more intricate structures.[39] This characteristic results in structures exhibiting unique architectures, as the building blocks of each structure establish macro or mesopores that effectively prevent aggregation and restacking.[40] Carbon-based nanomaterials, distinguished by their remarkable mechanical, electrical, and optical properties and easy surface functionalization, hold a prominent position in the field of 3D nanomaterials.[41] Carbon-based 3D nanomaterials have demonstrated extensive utility in a range of biomedical applications, spanning phototherapy, imaging, drug delivery, tissue engineering, and biosensing.[42] Additionally, metals such as iron, silver, and metal oxides, among others, have been assembled as 3D nanomaterials, particularly for the aforementioned biomedical applications.[40]

Biomedical applications necessitate nanomaterials that exhibit stability in water and under physiological conditions, ideally showcasing attributes of biocompatibility, biodegradability, or excretability. Particularly, when employed in phototherapy, drug delivery, imaging, or tissue engineering, these nanomaterials should also be responsive to various stimuli, including light, acidity, magnetic fields, or different concentrations of specific molecules. Such responsiveness enhances efficiency and reduces the required concentration of the nanomaterial, thereby promoting increased biocompatibility. Hydrophobic nanomaterials often tend to form aggregates and precipitate in aqueous solutions. To circumvent this issue, covalent, non-covalent functionalization, and other forms of surface modification can be implemented. These strategies should be chosen judiciously to ensure that the key properties of the nanomaterials remain intact, such as photoabsorption or biocompatibility.

Covalent functionalization involves the chemical bonding of selected compounds to the nanoparticles. For instance,

Artur M. Pinto

Artur M. Pinto graduated in Pharmaceutical Sciences, obtaining his PhD in Biomedical Engineering from Faculty of Engineering – University of Porto (FEUP), visiting U. Washington (USA). Afterward, Artur has been appointed as a Post-Doctoral Researcher at Eindhoven University of Technology, the Netherlands. Following his Post-doc, Artur has been awarded a long-term Researcher position at LEPABE-FEUP. He is the Principal Investigator of collaborative projects between FEUP, i3S (Institute for Research and Innovation in Health), and UT Austin (USA) focused on developing new 2D-nanomaterials and adjusting their properties for biomedical applications, such as phototherapy and magnetic hyperthermia of cancer, involving chemotherapy and immunotherapy, and 3D-printing.

surface oxidation can be employed to introduce reactive oxygen species (ROS)-generating moieties at the surface, creating pathways for forming covalent bonds with hydrophilic polymers, drugs and genes, or targeting ligands.[29] Polyethylene glycol (PEG) is often regarded as the gold standard for improving the biocompatibility of various nanomaterials, including graphene oxide (GO) and other nanosheets. PEG is typically integrated onto the surface of the nanomaterial *via* covalent functionalization, leading to improved photothermal efficiency properties of GO when functionalized with PEG through covalent bonding.[43] It is important to note that covalent functionalization may alter the original structure of nanomaterials, potentially resulting in a decrease in key characteristics by disrupting delocalized π–π systems.[44]

Non-covalent functionalization relies on interactions such as hydrophobic and hydrophilic, electrostatic forces, π–π stacking, van der Waals forces, or hydrogen bonding.[29] These non-covalent interactions enable the modification of a particle's surface through conjugation with various molecules if sufficient physical affinity exists. For instance, DNA and tRNA have been attached to chitosan nanoparticles through hydrogen bonding and electrostatic interactions using G–C and A–U base pairs.[45] In the case of amphiphilic molecules, the hydrophobic part is non-covalently anchored to the surface of hydrophobic nanomaterials, while the hydrophilic end extends into the solution, enhancing stability.[29] While non-covalent functionalization does not alter delocalized π–π systems, the assembled structures are typically considerably weaker. For example, the non-covalent functionalization of gold nanoparticles has been employed to improve biocompatibility, water stability, and specificity by binding to hyaluronic acid multilayers.[46] Fig. 1 illustrates common functionalization methods, self-assembly types, and examples of biomedical applications for various inorganic nanomaterials.

The most extensively researched inorganic nanomaterials for nanomedicine primarily include metals and their oxides, such as gold, gold nanoclusters, zinc, zinc oxide, titanium, silver, silica, iron oxide, quantum dots, superparamagnetic iron oxide, thallium, and platinum.[8,10,20] Additionally, carbon-based materials, including carbon nanotubes, fullerenes, nanodiamonds, and GO, have garnered significant attention in various biomedical applications.[47] Self-assembled inorganic nanomaterials, produced through diverse methods, have found applications in cancer theranostics, simultaneously enabling tumor imaging and exerting therapeutic effects.[48–56] Additionally, they have been employed to enhance the radiosensitivity of cancer cells, mitigating radiotherapy resistance.[57] These nanomaterials have also demonstrated utility in improving imaging techniques, such as photoacoustic (PA) imaging,[20] with notable progress reported in drug delivery applications.[58]

Common approaches to self-assemble nanomaterials for biomedical applications include hierarchical self-assembly,[6,59–61] layer-by-layer self-assembly,[46,62,63] metal ion-induced self-assembly,[64,65] and magnetic-induced self-assembly.[66,67] In the context of hierarchical self-assembly, inorganic nanomaterials have been constructed for imaging,[59] chemotherapy and drug delivery,[60] photothermal therapy,[61] and even the development of an organ-on-a-chip.[6] Layer-by-layer self-assembly has been employed for assembling inorganic nanomaterials for drug delivery[46,62] and cancer phototherapy.[46] In the biomedical field, supramolecular self-assembly based on polymers has undergone extensive research, particularly in drug delivery and tissue engineering. This involves the assembly of vesicles, micelles, and hydrogels through block copolymer assembly.[68] While there exists a review specifically focused on self-organization and the self-assembling process in tissue engineering *in vivo* studies, it is noteworthy that the comprehensive exploration of materials' properties, self-assembly mechanisms, and *in vitro* effects is lacking.[69] Hence, there is a need for a comprehensive description of the state-of-the-art in the field of self-assembled inorganic nanomaterials for other biomedical applications, which will be presented in the following sections.

2. Self-assembly

The inspiration drawn from Nature's self-assembly structures has spurred scientific exploration and innovation in the development of novel materials based on these principles. Molecular self-assembly, a ubiquitous process in the formation of essential structures for complex life forms, including lipid membranes, higher-order structured proteins, nucleic acids, and multicomponent protein aggregates, has been a subject of study for decades.[70,71] Despite decades of recognition, a consensus on the definition of self-assembly remains elusive, primarily due to terminology overlap and the nuanced distinction between self-assembly and self-organization across different scientific disciplines.[69,72] The application of self-assembly concepts to the fabrication of inorganic nanostructures has become feasible with the emergence of nanofabrication and nanomaterials. However, this transition poses challenges, as the well-established techniques in biological and organic systems may not seamlessly translate to the production of inorganic nanostructures.[73,74]

Self-assembly is defined as the spontaneous organization of molecules or pre-synthesized nanoparticles into highly organized structures through non-covalent bonds.[36,75,76] There are five universally accepted key points characterizing self-assembly. Firstly, molecular recognition is essential, requiring interactions between molecules or structures to form organized patterns. Secondly, self-assembly relies on a delicate balance of attractive and repulsive forces, typically weak, among the components. Thirdly, entities involved must possess mobility to come into contact and facilitate mass migration. Fourthly, self-assembly commonly occurs in solution or on a smooth surface or interface. Lastly, the fifth point emphasizes the reversibility of self-assembled structures. It is widely believed that self-assembled structures must be reversible due to the involve-

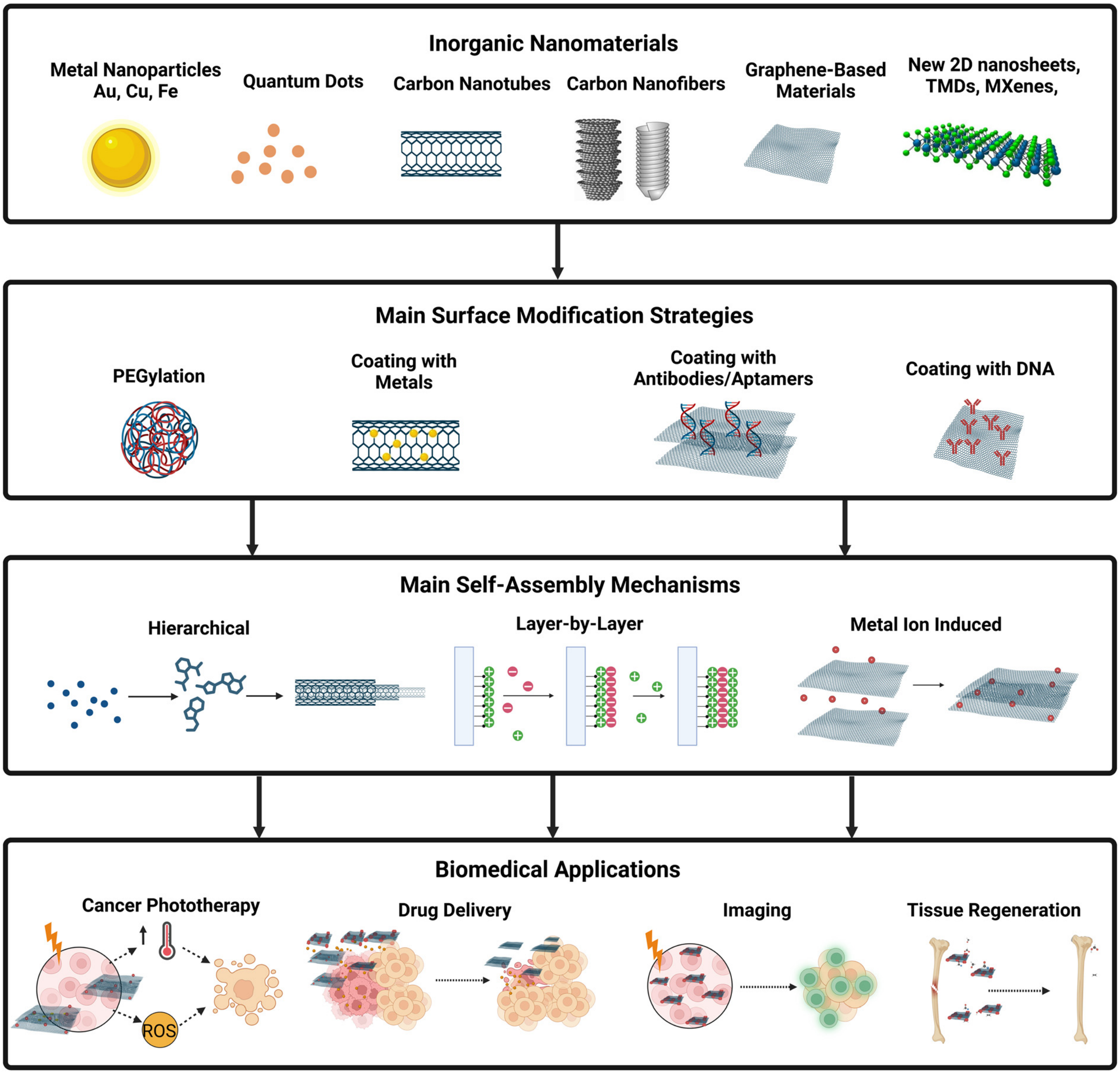

Fig. 1 Inorganic nanomaterials common surface modifications, self-assembly types, and biomedical applications. As an example, carbon dots can be modified with polymers, such as PEG, to increase water stability and biocompatibility, which is important for imaging applications. Inorganic nanotubes can be functionalized with gold nanoparticles to enhance light absorption which is important for phototherapy applications. Nanosheets and other nanostructures can be coated with antibodies or aptamers to increase the specificity of the nanoparticle to a specific cell, which is important for drug delivery, tissue regeneration, and cancer therapy. The main self-assembly mechanisms of inorganic nanoparticles produced for biomedical applications are hierarchical, layer-by-layer, and metal-induced self-assembly (see Table 1). Created with Biorender.com. Abbreviations: PEG, poly(ethylene glycol); PVP, polyvinylpyrrolidone; Au, gold; Cu, copper; MNP, magnetic nanoparticles; ROS – reactive oxygen species; RMDs, refractory metal dichalcogenides; TMOs – transition metal oxides; DOX – doxorubicin.

ment of non-covalent weak interactions and some covalent bonds.[73,77] The extensive study of biological and organic self-assembled systems has led to the assumption that reversibility is a shared feature among all self-assembled structures. However, as self-assembly extends into the inorganic domain and scientific knowledge progresses, some works suggest that self-assembly can be irreversible.[78–80] This highlights the evolving understanding of self-assembly dynamics, especially in the context of inorganic materials.

Self-assembly mechanisms can be classified into a range of categories, broadly classified into static or dynamic,[73,81] chemical, physical, or colloidal,[81,82] and guided self-assembly (also known as directed or templated self-assembly).[81] Further categorization is possible based on size (atomic, molecular, or colloidal) and the nature of interaction (interfacial or biological).[75,83] Guided self-assembly stands out with numerous subcategories, encompassing techniques such as electric or magnetic fields, lithography/masking, surface wetting, patterned substrates, and seeding.[73,81,82,84,85] In contrast, conventional self-assembly techniques include supramolecular self-assembly (encompassing amphiphile self-assembly with lipid, peptide amphiphile, block copolymer, and hierarchical structures), layer-by-layer assembly, among others.[86,87] The richness of self-assembly categories highlights its vast and versatile nature, especially with its recent extension into inorganic-based systems, as illustrated in Fig. 2.

There exists a divergence of opinions among authors regarding the definition of self-assembly, with some considering it to encompass all bottom-up methods mediated by the interaction of precursors in liquid or vapor form.[88] However, this perspective is not universally accepted within the scientific community. Irrespective of the specific self-assembly type, common interactions underlie the process across all categories. Notable interactions include hydrogen bonding or hydrogen-bonded frameworks, π–π stacking, van der Waals forces, electrostatic interactions (ion–ion, ion–dipole, dipole–dipole), and others like solvation, depletion, bridging, coordination bonds, electric double layer, hydration, steric effects, among additional factors.[71,75] These shared interactions contribute to the richness and versatility of self-assembly processes across diverse categories.

2.1 Self-assembly types

2.1.1 Static *vs.* dynamic self-assembly. The majority of established self-assembly systems fall under the category of static self-assembly, characterized by equilibrium and the absence of energy dissipation, as illustrated in Fig. 3. Examples of static self-assembly include self-assembled peptide-amphiphile nanofibers and the formation of a three-dimensional aggregate of micrometer plates through capillary forces. In contrast, dynamic self-assembly systems, which are less explored, require a constant dissipation of energy. The interactions between structures within dynamic systems demand continuous energy input to maintain their positions, and the system disassembles when the energy flow ceases. Dynamic self-assembly is commonly observed in biological and living systems, but it can also manifest in inorganic systems. Examples include an aggregate of rotating magnetized disks interacting *via* vortex–vortex interactions and the collective movement of a school of fish.[73,81] Studies have demonstrated that a system can transition between static and dynamic self-assembly by introducing a magnetic field.[89,90]

Both static and dynamic self-assembly systems can be further categorized into co-assembly, hierarchical self-assembly, and directed self-assembly. Co-assembly involves the par-

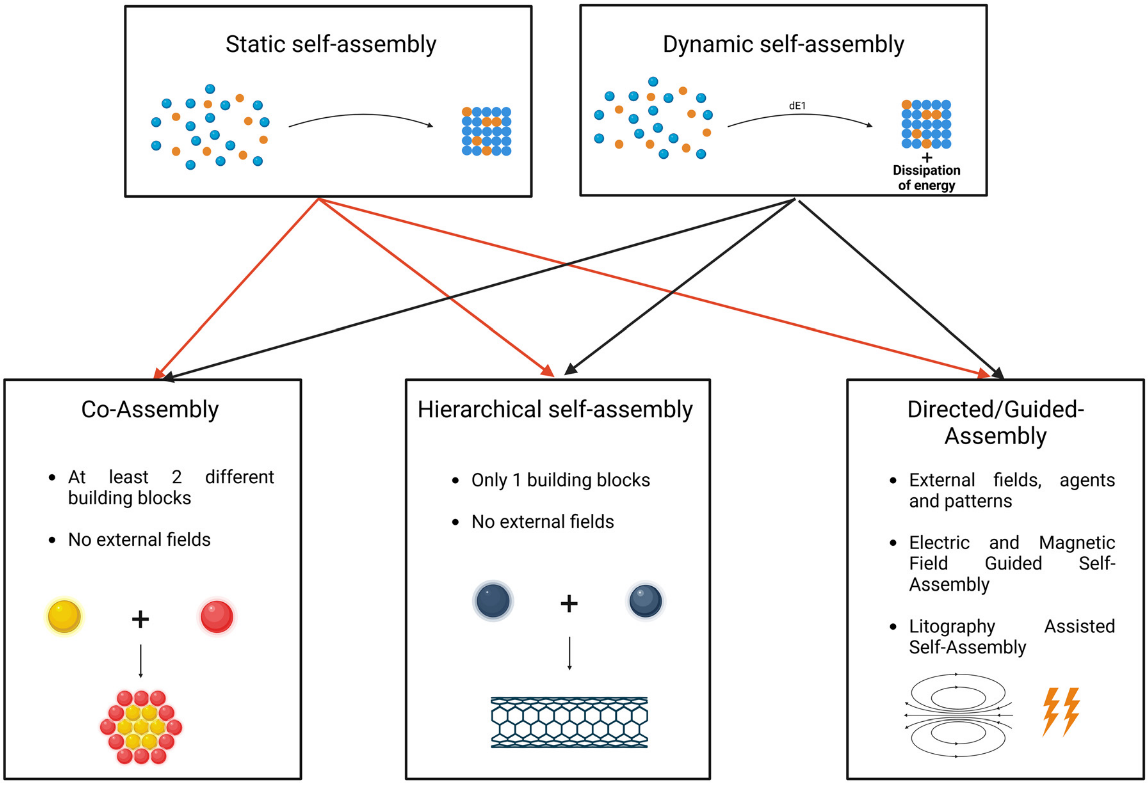

Fig. 2 Different categories of self-assembly. Static and dynamic self-assembly (top). Different subcategories of self-assembly, including co-assembly, hierarchical self-assembly, and Directed/Guided Assembly. Co-assembly is defined by the spontaneous interactions of 2 different building blocks, resulting in a new nanoparticle. Hierarchical self-assembly consists of the repeated interaction between various equal building blocks. Directed/Guided Assembly occurs when a nanocomplex is formed as a result from the interaction between an external field, or template and a homogeneous or heterogeneous system. Created with Biorender.com.

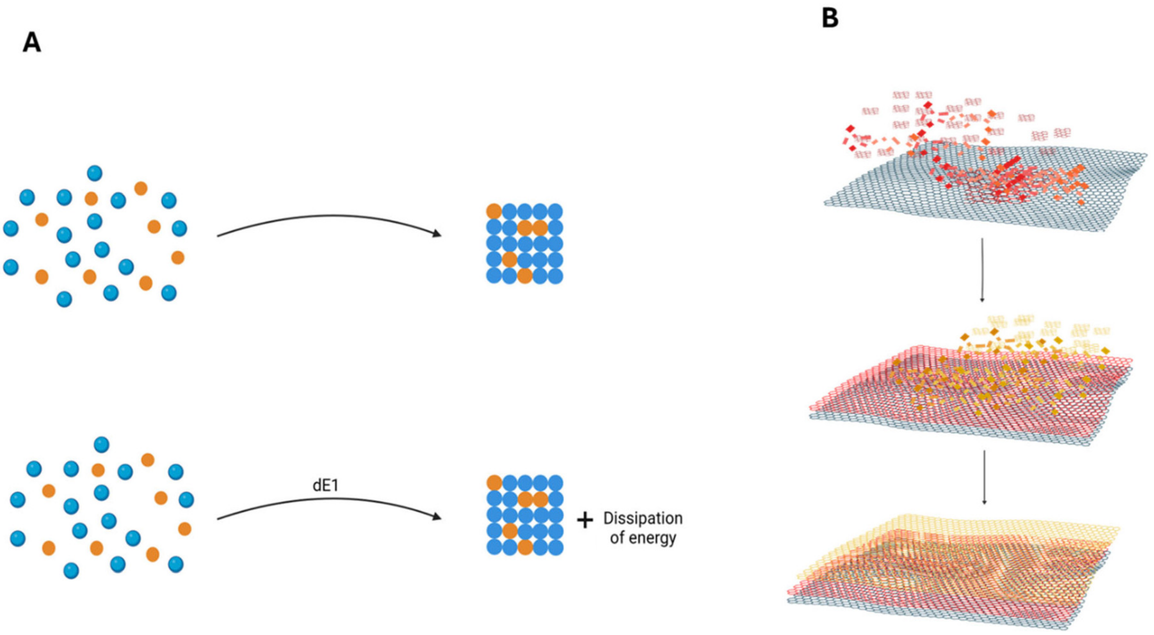

Fig. 3 (A) Illustration representing the differences between static and dynamic self-assembly. Static self-assembly (top) is characterized by equilibrium and the absence of energy dissipation, while dynamic self-assembly systems (bottom) require a constant dissipation of energy. (B) Schematic diagram of layer-by-layer self-assembly. Layers are formed by exposing a substrate to solutions with positively or negatively charged species alternately, leading to the spontaneous deposition of a multilayer system. Created with BioRender.com.

ticipation of a heterogeneous system in the self-assembly process, meaning different building blocks coexist in the same system. Hierarchical self-assembly entails the repeated use of the same building block for interactions at various length scales, from short-range to medium-range and long-range. Directed self-assembly occurs in predefined areas influenced by external forces or custom patterns. This approach often combines bottom-up and top-down methods.[81]

2.1.2 Guided self-assembly. Guided self-assembly, alternatively known as templated, directed, or assisted self-assembly, is a process that enhances the yield of highly structured and organized materials by introducing templates and external fields that interact with particles.[71] This approach can be subdivided into various techniques, including electrical field-guided self-assembly, magnetic field-guided self-assembly, lithography or masking, capillary force-induced self-assembly, flow-directed self-assembly, electrostatic self-assembly, solution-based self-assembly, among many others. Each of these methods involves the deliberate manipulation of external factors to guide and control the self-assembly process, allowing for the precise arrangement and organization of particles to achieve desired structures.

2.1.2.1 Electric field guided self-assembly. Electric fields can induce self-assembly by exposing a system containing molecules and nanoparticles to direct current or alternating current fields, as illustrated in Fig. 4.[71,85,88] The key property facilitating field-induced assembly is particle polarization, which is influenced by the dielectric properties of the particles, the surrounding medium, and the distribution of electrons within the particles. The charges within the double electrostatic double-layer also contribute to polarization when exposed to an external field.[71,85,91,92] When particles in a solution are subjected to electric fields, they tend to polarize due to mismatches in dielectric properties with the solvent.[71,85,93] Applying an electric potential results in the attraction of charged particles towards the electrode of the opposite charge, causing the migration of nanoparticles – a phenomenon known as electrophoresis.[71,85,88,94] When the interaction is sufficiently strong to overcome Brownian movement, and the electric field and electrophoresis force are increased significantly, particles sensitive to the electric field can form dipolar chains, assembling into various structures. While both direct current and alternating current can be employed to promote guided self-assembly, the use of alternating current offers advantages over direct current. Alternating current minimizes electroosmotic and electrochemical effects associated with direct current applications.[93,94]

2.1.2.2 Magnetic field guided self-assembly. Similar to electric field-induced assembly, magnetic fields play a crucial role in directing the self-assembly of magnetic nanoparticles (MNPs) by either inducing or leveraging natural dipole–dipole interactions.[71,85,88,95] The interaction nature can be attractive or repulsive, depending on whether the dipoles are aligned in parallel or antiparallel directions, as depicted in Fig. 4. The self-assembly induced by external magnetic fields can be reversible, contingent on the energy and strength of the bonds between atoms, utilizing magnetophoresis and the magnetophoretic force to guide the assembly. Consequently, the particles must either be magnetically sensitive, or the medium in which the nanoparticles are suspended should be

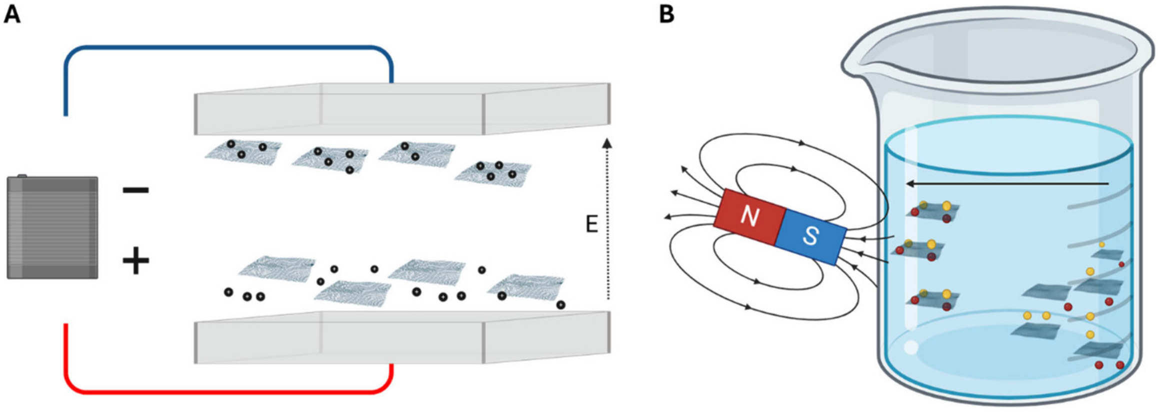

Fig. 4 Illustration of self-assembly of nanoparticles through exposing the materials to an electric field (A) or a magnetic field (B). Applying an electric potential results in the attraction of charged particles towards the electrode of the opposite charge, when the interaction is sufficiently strong, particles can form dipolar chains that are assembled into various structures. Similar to electric field-induced assembly, magnetic fields play a crucial role in directing the self-assembly of magnetic nanoparticles by either inducing or leveraging natural dipole–dipole interactions. Created with BioRender.com.

magnetic.[85,88,93,94] Several factors, including the volume of the particles, magnetic field gradient, and susceptibility contrast between the particles and the medium, directly influence the characteristics of the self-assembled nanoparticles and their propensity to self-assemble.[85,94] The geometrical configuration is dependent on the strength of the magnetic field, the nature of the bonds, and the shape of the molecules to be self-assembled. Magnetic nanoparticles find considerable use in biomedical applications, particularly as drug delivery vehicles and for magnetic resonance imaging (MRI).[71,93,94]

2.1.2.3 Self-assembly guided by lithography. Particle lithography exploits the self-assembly capability of colloidal particles to create larger and more complex structures. Techniques such as controlled evaporation, convective assembly, spin-coating, and electrophoretic deposition have successfully produced large-area, close-packed crystalline assemblies of colloidal spheres. These assembled nanospheres can serve as lithography masks, either positively using the particles or negatively using the interstitial spaces, to guide and form controllable molecular patterns on a substrate.[71,85,96]

Various lithography approaches promote molecular self-assembly, including photolithography, interference lithography, electron beam lithography, mold-based lithography (including nanoimprint lithography and soft lithography), and nanostencil lithography.[88,97,98] Photolithography, also known as lithography or UV lithography, uses radiation to transmit a defined shape from a mask or model to a photosensitive resist on a substrate. Chemical treatments are then applied to inscribe the transmitted pattern or allow the deposition of new material in the chosen shape. Interference lithography utilizes short bursts of light waves to create high-density patterns in a large area of a photosensitive substrate. The technique involves the interference of two laser beams and finds applications in display panels, surface-enhanced Raman scattering (SERS) active substrates, solar cells, magnetic storage devices, and more.[85,88,91,92,94,96–98]

Electron beam lithography focuses and accelerates electrons onto an electron-sensitive material coated on the substrate, altering the chemical and physical properties of the irradiated molecules. The pattern is created by immersing the substrate in a developer solution, resulting in the desired nanoparticles.[85,88,91,92,97,98] Nanostencil lithography employs stencils to construct nanometer-scale patterns and nanoparticles, either additive or subtractive. The nanostencil can act as a mask for material deposition or protection by placing it between the substrate and the material source.[85,88,97,98]

Nanoimprint lithography involves pressing a hard mold with required patterns into a polymeric layer. After thermal treatments, the polymer, displaying the mold's patterns, can be separated, and used as a functional nanoparticle or as a mask to transfer patterns to other materials. This method allows the replication of small features up to 5 nm and has been employed for various applications.[97,98] Nanosphere lithography is a simple and efficient method to produce nanostructures and 2D nanoarrays. However, its utility is limited by the requirement for monodisperse solutions and easily reproducible nanoparticles. The process begins with the self-assembly of nanospheres in a solution to form a deposition mask, which is then transferred to other substrates to create diverse patterns.[88,97,98]

Selective modification of the substrate surface plays a crucial role in guiding the self-assembly process by altering the capillary force experienced by particles. This discriminatory self-assembly is achievable by changing the surface hydrophobicity, where colloidal particles in a suspension assemble onto hydrophilic surfaces while avoiding adhesion to hydrophobic regions.[81,99] Utilizing a substrate with locally defined hydrophobic or hydrophilic structures enables the manipulation of surface wetting and the creation of assembly patterns. This involves inducing areas where colloidal particles are compelled to form nanostructures, while in other areas, self-assembly is inhibited.[100] Wetting is quantified by the contact angles of a solution drop on the substrate surface, with complete wetting achieved at a contact angle of 0° and complete nonwetting at 180°.[20]

Flow-directed self-assembly leverages fluidic flow properties to direct the assembly of nanoparticles with features that interact with the flow.[76] Macroscopic viscous flows can order a suspension of nanomaterials, transforming them into nanocrystals.[76,93] Large amplitude oscillatory shear is employed to order particles ranging from 100 nm to 1 μm. The properties of the applied field, such as shear rate, shear strain, particle volume, particle charge, polarity, and potential for interactions with other molecules, are tunable and directly impact the capacity of colloidal self-assembly and ordering.[93] High flow strengths are necessary for effective nanoparticle ordering, and upon removal of the force, molecules tend to disaggregate into a chaotic distribution. One challenge is that the flow applied in laboratory procedures is typically much smaller than the magnitude required for industrial applications, limiting the feasibility of this guided procedure in industrial environments.[93,94]

2.1.3 Conventional or solution-based self-assembly. As previously mentioned, the distinction between hierarchical self-assembly and co-assembly is mainly dependent on the number of building blocks that are involved in the construction of a more complex structure. As illustrated in Fig. 2. When only one type of building block is used during the synthesis of the new particle, the synthesis process can be categorized as hierarchical self-assembly. However, if two or more molecules or particles interact spontaneously to form a new nanocomplex, the self-assembly process is defined as co-assembly. The following self-assembly types and fabrication techniques can be included in both definitions depending on the number of building blocks in the system.

Solution-based self-assembly fabrication techniques, while sharing the fundamental principle of creating conditions for self-assembly through intermolecular reactions without the interference of external fields, offer diverse pathways to build nanostructures with vastly different properties. These properties can be adjusted by changing precursor molecule concentrations or by incorporating molecules with different properties. This process enables control over the geometrical features of nanoparticles and is typically a simple and cost-effective experiment. The fabrication process can vary significantly depending on the properties of precursor substances such as surfactants and solvents.[85,88] Common solution-based self-assembly procedures include evaporation-based self-assembly, layer-by-layer self-assembly, and colloidal growth.[85]

Supramolecular self-assembly has garnered attention from researchers due to its foundation in natural processes, playing a crucial role in constructing and functionalizing numerous nanoparticles, molecules, and natural materials with intriguing properties essential for the environment's natural functions.[101] Supramolecular self-assembly involves the formation of organized and complex structures from other molecules and particles, referred to as building blocks. This assembly is a result of exposing the molecules to various intermolecular forces, including the hydrophobic or solvophobic effect, electrostatic forces, hydrogen bonding, π–π stacking, coordination interactions, and dipole–dipole interactions.[102]

Layer-by-layer (LbL) self-assembly revolves around depositing colloids, molecules, and smaller particles onto a previously constructed surface.[88,103] After deposition, the layers are kept intact and bonded by various intermolecular forces, such as electrostatic forces and hydrogen bonding, as illustrated in Fig. 3.[88,103,104] The layers are formed by exposing the substrate to solutions with positively or negatively charged species alternately, leading to the spontaneous deposition of a multilayer system with various layers due to the adsorption of oppositely charged particles on the substrate.[88,103,104]

The washing procedures constitute the final step in this self-assembly method, involving the exposure of the layers to ultrapure water between the addition of different charged materials, constituting a deposition step.[88,103] The described method represents the conventional immersion-based approach of layer-by-layer assembly.[103] However, common techniques like spin assembly, which mimics the adsorption of alternately charged particles on a substrate while providing rotation of the substrate layer, and spray assembly, which employs sprays and aerosols to build various layers, are also part of conventional layer-by-layer assembly methods.[103,104] Additionally, fluidic assembly and electromagnetic assembly fall within this category, with fluidic assembly using fluidic channels or pipetting techniques, while electromagnetic assembly relies on electromagnetic forces to drive the self-assembly process.[103] Layer-by-Layer assembly's production of thin films has numerous applications in areas such as biomedicine, drug delivery, and the creation of separation or selective barriers.[103,105]

Evaporation-induced self-assembly (EISA) is a solution-based self-assembly method, similar to layer-by-layer self-assembly, hydrothermal self-assembly, and colloidal growth.[71,88,106] This method generates nanoparticles by trapping the self-assembly process within compartments such as micelles and other organic shells.[88] Micelles, formed by amphiphilic surfactant molecules with hydrophilic heads and hydrophobic tails, aggregate when in contact with an aqueous solution, binding the heads and enclosing the tails inside a spherical structure. Hydrophobic nanoparticles or their precursors can be encapsulated in these micellar structures to induce their assembly.[88,106]

EISA utilizes an air-film interface to induce the evaporation of the most volatile components in the solution or formed film. This reduction in volume between molecules forces their alignment, leading to an increased concentration of other solutes, such as the surfactant. This concentration increase triggers the self-assembly of the remaining components into a hybrid inorganic–organic compound. After removing the surfactant molecules, the resulting structure is a robust mesoporous film.[88] EISA can be employed to produce various nanoparticles with highly desirable characteristics. These characteristics can be tuned by adjusting initial parameters such as solution composition, pH, and processing factors like partial vapor pressures, convection, temperature, and more.[107]

The self-assembly of nanoparticles at liquid–liquid, liquid–air, and liquid–solid interfaces can be achieved through techniques such as Langmuir–Blodgett, sedimentation, and evaporation-induced self-assembly, along with the adsorption of nanoparticles and various other methods not extensively mentioned in this review.[85] The Langmuir–Blodgett method is employed to create nanoparticles at the liquid–gas interface, which are subsequently transferred to a solid substrate. This method involves precursor particles of soft materials. Langmuir films are characterized as monolayer compounds of amphiphilic molecules assembled by linking their partially dissolved hydrophilic heads. The hydrophobic tails extend to the gaseous phase to minimize free energy. Fully formed Langmuir films are compressed to create highly condensed films, ensuring the physical consistency of the film before transferring it from this interface to a solid substrate. The transfer is achieved by immersing the solid substrate onto the liquid surface, and this process can be repeated to form a multilayer structure, as illustrated in Fig. 5.[88,108] This versatile procedure allows the production of precise films and mesoporous materials with nano-precision control over film thickness, composition, and the sequence of various layers. The versatility of this method permits the use of various molecules, ranging from inorganic particles to organic molecules with biological functions.[108]

The self-assembled monolayers (SAMs) method is primarily used to prepare single-layer functional structures of various soft materials, allowing precise control over the composition of each segment of the built layer.[108] This technology is highly valuable for surface engineering, enabling the modification of surface properties of the targeted structure, such as wetting, adhesion, lubrication, cell attachment, and more.[83,108] Molecules utilized in this method should have a head with a strong affinity to the substrate, a tail, and a functional group. SAMs molecules are prepared through the adsorption of a chemical anchoring group to a substrate and van der Waals interactions between the molecules. The assembly of particles in this method is driven by the chemisorption of the head of the molecules with the substrate, followed by the organization and association of the tails to achieve an equilibrated organization that minimizes surface free energy.[88]

Colloidal growth is a relatively novel concept, and the factors leading to particle growth are not extensively studied, explaining the lack of theoretical models to explain the mechanism. Literature suggests that colloidal growth is based on the colloidal stability of molecules in a solution. In contrast to nucleation models, the size and characteristics are determined by colloidal stability rather than thermodynamic stability. Colloidal stability-driven growth posits that nanoparticles grow to a size where they cannot overcome the energy of aggregation. The energy involved, referred to as the deactivation energy, is defined as the amount of energy in the particles at which aggregation stops.[88,109] Liquid crystals (LCs) are fluids exhibiting precise oriented order in their constituent molecules, possessing characteristics like optical birefringence and curvature elasticity. They exist in an intermediate state between crystalline solids and isotropic liquids, and their constituent molecules are anisotropic molecules or aggregates in surfactant solutions. Depending on their characteristics, LCs can be classified into three groups: thermotropic liquid crystals, lyotropic liquid crystals, and metallotropic liquid crystals.[88] LCs are promising candidates for guided self-assembly of nanoparticles, as they combine order and mobility at the molecular level. Additionally, these materials are responsive to external fields and can change their properties when in contact with other surfaces.[110] LCs have the capability to guide and alter the physical properties, inducing the formation of different molecular bonds of colloidal particles dissolved in a solution with LCs. Responsive LCs interact with the atoms of colloids, competing with electrostatic and elastic interactions between colloids. This interaction allows molecules to rotate relative to the LCs, assembling the dissolved colloids into a thermodynamically favorable phase, resulting in a transformation of the LCs phase and a change in the molecule's configuration.[100]

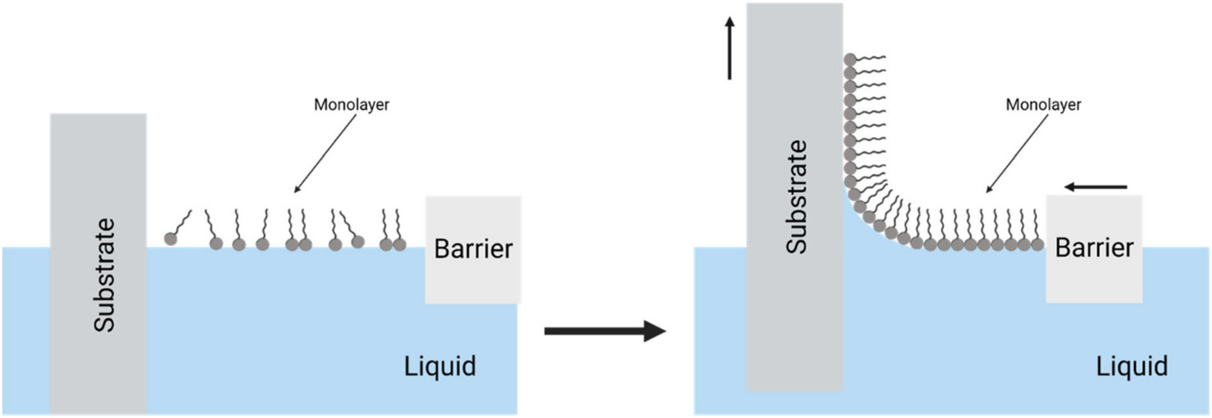

Fig. 5 An illustration of the Langmuir–Blodgett method, depicting the compression of a monolayer and the consequent transfer from the liquid towards the surface of a solid substrate. Created with BiRender.com.

DNA techniques for self-assembly have been utilized to precisely control the orientation and arrangement of nanoparticles, especially nanostructures with metal ions like Ag and Au, as these metals readily bind with the functional groups of DNA.[100] The two major methods of guided self-assembly with DNA are the DNA templating strategy and DNA scaffold-directed self-assembly. In guided self-assembly with DNA, particles may be functionalized with a strand of DNA if the particle lacks a section capable of bonding with other functionalized molecules. DNA recognition of the particles directs the molecules to assemble in a designed manner with a configurational or constitutionally planned chiral structure.[91,95] In DNA templating, DNA molecules act as rigid structures that induce the deposition of nanoparticles and colloidal molecules with sensitive receptors to the functional groups of the DNA structures.[91,95] DNA-dependent self-assembly has been employed to develop bulk-scale hydrogels, induce the crystallization of nanoparticles, and control the synthesis of organic nanomaterials for drug delivery.[88]

2.2 Chemical *vs.* physical *vs.* colloidal self-assembly

Different perspectives on the classification of self-assembly are evident in the literature. According to Gatzen *et al.*, chemical self-assembly involves the formation of a new crystal lattice or chain through non-covalent bonding, exemplified by Self-Assembled Monolayers (SAMs). Physical self-assembly refers to the assembly of inorganic molecules or atoms during physical processes like Molecular Beam Epitaxy (MBE) or Chemical Vapor Deposition (CVD), producing low-defect and high-purity thin films. Colloidal self-assembly, in this view, involves particles in a liquid suspension.[81] However, Ziaie *et al.* present an alternative perspective, combining physical and chemical self-assembly and excluding colloidal self-assembly as a distinct category. They describe physical self-assembly as the spontaneous aggregation/organization of colloidal nanoparticles through non-covalent interactions, citing Evaporation-Induced Self-Assembly (EISA) as an example. Chemical self-assembly, in this context, includes SAMs, DNA, and others, aligning with Gatzen's perspective.[82]

It is worth noting that some authors suggest considering bottom-up methods like Molecular Beam Epitaxy (MBE) and Chemical Vapor Deposition (CVD) as forms of self-assembly, challenging the traditional definitions. However, the reluctance to include these techniques in the self-assembly category may stem from the historical association of self-assembly with biological systems and the ongoing lack of consensus and study regarding definitions of inorganic self-assembly.[88] The diversity of perspectives underscores the evolving nature of the field and the ongoing discussions surrounding the classification of self-assembly techniques.

2.3 Interactions in self-assembly

Hydrogen bonds and hydrogen-bonded frameworks result from the attractive force between a hydrogen atom covalently bonded to an electronegative atom, such as oxygen or nitrogen, and another electronegative atom or molecule.[111] Hydrogen-bonded frameworks involve the assembly of 2D or 3D crystalline networks through hydrogen bonding.[112] For instance, the hydrogen atom covalently bonded to oxygen in a water molecule creates a positive and a negative zone, leading to attraction between hydrogen and oxygen in neighboring water molecules. While hydrogen bonds were initially considered within the scope of electrostatic interactions, various mechanisms beyond purely electrostatic interactions are involved.[113] Manipulating hydrogen bonds allows the creation of various molecular structures.[114] Researchers, such as Ilhami *et al.*,[115] have utilized self-assembly based on hydrogen bonds to produce nanogels suitable for biomedical applications. π–π stacking interactions are particularly prominent in aromatic systems and can be classified into three subcategories: edge-to-edge T-shape, parallel displaced, and cofacial parallel.[116] Supramolecular self-assembly based on π–π stacking has found extensive use in drug-loading applications, especially for hydrophobic antitumor drugs with aromatic π–π conjugated structures. Carbon-based materials and micelles, both possessing delocalized π-bonds, serve as favorable carriers for drug loading.[117,118] Despite being overlooked at times, π–π stacking interactions also play a role in stabilizing hydrogen-bonded frameworks.[119] These interactions can be harnessed in inorganic self-assembly systems, as most non-covalent interactions are associated with supramolecular chemistry.[120] van der Waals interactions, based on attractive forces, arise from induced dipoles due to the temporary displacement of electronic charges or permanent dipoles, such as polar molecules. Despite being considered one of the weakest forces, van der Waals interactions play a crucial role in controlling condensation and aggregation processes, influencing adhesion and absorption of molecules on inert materials like graphene.[121–125] These interactions are highly sensitive to geometry, location, structure, and external environmental characteristics.[124] Consequently, van der Waals interactions can alter the properties of nanoparticles, including structure, molecular dynamics, and electronic charge distribution, by employing different external interferences and conditions.[119,124]

Electrostatic interactions play a crucial role in the self-assembly process, involving the attraction of oppositely charged ions or the repulsion of particles with the same charge. The interaction is described by Coulomb forces and is characterized as a long-range force (up to 50 nm) with much higher strength (typically 500–1000 kJ mol^{-1}) compared to other forces such as van der Waals interactions (1 kJ mol^{-1}). For colloidal systems, electrostatic forces depend on the magnitude of the particle's charge, direction of movement, and the shape of the global electron charge, among other factors. The complexity of these dependencies allows the use of electrostatic forces to self-assemble nanoparticles, providing control over environmental characteristics.[53,71,73,75] Nanoparticles developed in solution or water present an interfacial double layer responsible for interactions, consisting of the Stern layer and the Gouy-Chapman diffuse layer.[71,73] Electrostatic forces can be employed to assemble molecules with the same or different charges, as well as particles of various sizes, ranging from quantum nanorods to electrically and magnetically responsive micelles.[53,71,73]

Electrostatic interactions, particularly between particles with opposite charges, has been instrumental in constructing a wide range of nanoparticles, from small structures to complex 3D superstructures. Electrostatic interactions are utilized in various self-assembly techniques, including templated self-assembly, electrical assembly, layer-by-layer assembly, and others.[100] Patterned substrates serve as a strategy for nanoparticle self-assembly, involving surface irregularities where a drop of a suspension is deposited. The driving force behind shaping the solution into a defined pattern is the capillary force of the liquid. As the liquid evaporates, the patterns confine the liquid, concentrating nanoparticles into a smaller space. In this confined space, electrostatic forces from the suspension in an ionic solution or interparticle van der Waals forces come into play, leading to the assembly of new nanostructures.[81,95] Electrostatic interactions are highly influenced by factors such as pH, electrolyte concentration, and ion strength due to screening effects on nanoparticle surfaces.[85,94,126] These forces, categorized as noncovalent, contribute to the self-assembly of various nanoparticles and work in conjunction with hydrophobic interactions, determining the finite size and shape of the assembled nanoparticles.[75]

Solvation interactions, a short-range interaction also known as a structural force, can be attractive or repulsive for the self-assembly of colloidal and intermolecular structures dissolved in a solution.[83] This force complements other forces like van der Waals forces and electric double-layer interaction. Solvation force arises from the formation of layers of solvent particles around the surface of colloidal molecules, leading to the creation of solvation shells. Tuning solvation force is possible by changing physical factors dependent on this force, such as shape, size, and polarity of solvent molecules, or by altering properties of colloidal surface molecules like hydrophobicity or hydrophilicity, geometrical shape, and surface homogeneity.[20] Solvation interactions between nanoparticles occur at the solvent–solvent and solvent–colloidal surface interfaces, limited by solvent shells. These forces are essential for the assembly of various particles as they define colloidal stability and crystallization tendencies.[91,95]

Depletion force is an attractive force that occurs between large colloids suspended in a solution containing depletants. Depletants are typically small solutes such as polymers, small nanoparticles, micelles, and salts. The bonding between two colloids surrounded by smaller depletants is explained by the intersection of the area formed between each colloid and its depletants, with the distance between the two colloids defining the depletant diameter. This overlap excludes the depletants, leading to the appearance of an attractive force between the colloids. The release of some molecules increases the osmotic pressure and entropy, prompting the colloids to form aggregates.[100]

Bridging interaction occurs when nanoparticles are exposed to the bridging force. This force is characterized as an attractive force between colloidal particles dissolved in a colloidal system with polymer chains. In this solution, the polymer–polymer interaction is preferred over the polymer–solvent interaction, causing colloidal particles coated with polymers to experience an attractive force between them.[71] The strength of the bridging force is related to the number of smaller segments and other nanoparticles attached to the colloidal particles and molecules. This interaction can predict whether the conditions provided by researchers will induce the assembly of complex structures. If the affinity between the colloidal particles and the smaller elements is stronger than the attraction between the solvent molecules and the smaller segments, the adsorption of the fragments will occur. The bridging force induces attraction between particles, linking them.[127]

Coordination bonds involve metallic atoms and molecules, typically weaker (2–250 kJ mol^{-1}) compared to covalent linkages (100–400 kJ mol^{-1}), but they are reversible.[75,95] The bond strength and dynamicity are defined by the selection of the metal ion and ligand, which can be another metal, an organic, or an inorganic polymer. These bonds result in a structure with the metallic ion in the center surrounded by an array of ligands, and their formation involves the substitution of smaller ligands (*e.g.*, H_2O, Cl^-, NH_3) by larger ligands (*e.g.*, pyridine, carboxylate, phosphine), increasing entropy.[128] Coordination bonds enable the formation of various nanomaterials with biomedical applications, such as colloids, gels, and other solutions.[128,129]

Hydration forces are experienced by molecules and particles when dissolved or suspended in a solvent composed exclusively of water. These forces involve water–water and water–surface interactions, with hydration shells formed by solvent atoms surrounding the particle.[130,131] The nature of hydration forces depends on the surface characteristics of nanoparticles. For hydrophilic surfaces, the dominating net hydration force is repulsive for short separations, while for hydrophobic surfaces, the hydration force between molecules with such surfaces is attractive.[132] Hydration forces between nanoparticles in a solution are crucial for the assembly of particles with biomedical applications, influencing colloidal stability and crystallization tendencies. Studying and tuning hydration forces can improve nanoparticle systems.[130–133]

Steric forces refer to either attractive or repulsive long-range forces between nearby nanoparticles, typically coated with polymers or small particles. The magnitude of these forces is influenced by various interactions, including polymer–polymer, polymer–solvent, and polymer–colloid interactions, as well as factors such as ligand density, ligand molecular weight, and particle solubility in the solvent.[91,134] When nanoparticles are fully coated with polymers, interactions with other nanoparticles occur through the overlapping of polymeric layers, leading to solvent displacement and increased surface energy.[71,85,91,92,134] Repulsive steric forces find applications in building polymers for enhanced colloidal stability, artificial joints, transplants, drug delivery, and more.[71,85]

Capillary force, involved in colloidal self-assembly, comes into play when a particle contacts the triple interface of water (or another liquid), solid colloidal particles, and another medium, typically air. This interaction aims to minimize the free energy provided by the interfaces, reducing the interfacial area.[71,73,134,135] Capillary force can be either attractive or repulsive, exhibiting a long range and magnitude often superior to hydrophobic and van der Waals interactions. Its strength depends on surface tension, contact angle, particle size, medium density, and molecular properties of the colloid, including wetting behavior and surface roughness.[71,73,126,134] Tuning capillary interactions involves manipulating the shape of the meniscus at the interface between solid elements and the liquid, whether in a liquid–liquid or liquid–vapor interface.[71,126] While capillary force has various applications in self-assembly, such as constructing dense networks of solids, its low selectivity limits the precision achievable in secondary structures. The three major types of capillary forces are immersion, flotation, and bridging.[71]

Surface tension is the cohesive force exerted and experienced by particles of the same type, leading to the contraction of the liquid to achieve the smallest possible area, often forming a droplet to minimize total energy. This phenomenon occurs because molecules at the liquid's surface exhibit higher cohesive forces with inner liquid particles than at the liquid–gas or liquid–solid interfaces.[136] Always acting perpendicular to the liquid's surface, surface tension is dependent on the nature of the interface and is a result of the tendency of surface atoms to minimize the interface area, as the molecules and atoms on the liquid's surface are less stable.[136] In self-assembly, surface tension plays a crucial role, especially when the solution is not exposed to other forces. It determines the free geometrical shape of the solution and regulates the size of some self-assembled nanostructures.[137]

3. Self-assembly of inorganic nanoparticles for biomedical applications

Various inorganic nanoparticles have been self-assembled with either other inorganic molecules or with organic ones, forming hybrid structures that perform specific functions and have unique properties. Table 1 systematizes the main properties, assembly mechanisms, and interactions regarding inorganic nanoparticles developed by self-assembly for biomedical applications.

Gold nanoparticles can assume various configurations, from quantum dots and nanorods, to nanosheets. Those nanoparticles can be used as the starting material or as the coating material to enhance the properties of nanostructures, especially photothermal conversion efficiency. In the literature, promising results have been obtained using this material. Gold nanoparticles have been assembled into nanospheres (hydrodynamic radius = 78.8 nm) using dithiol-polyethylene glycol (HS-PEG-SH) and further modified with the chemotherapeutic agent doxorubicin (DOX) and the epidermal growth factor (EGF), to improve tumor targeting efficiency.[138] Song *et al.*[59] created double-layered magnetic vesicles using amphiphilic Janus nanoparticles of Au–Fe_3O_4 with a diameter of 110–115 nm. The authors took advantage of the different binding abilities of Fe_3O_4 and Au to self-assemble nanocomplexes. Hierarchical self-assembly was used to construct these mentioned nanocomplexes and to improve their photothermal capabilities and magnetic properties. Mono- or double-layered vesicles were assembled, the latter having two inverse types, as illustrated in Fig. 6.

Tao *et al.*[139] developed gold nanorods coated with Y-shaped CpG DNA, forming a nanostructure with an average size of 91.5 nm and a zeta potential of 18.6 mV. The DNA hybridization led to the self-assembly of the nanomaterial. This assembly type was used to improve the stability and specificity of the gold nanorods while maintaining good photothermal conversion properties.

Black phosphorus (BP) is another inorganic nanomaterial that can be used as a starting material or as a coating for various biomedical applications. In its two-dimensional form, black phosphorus is frequently used in cancer theranostics applications. Like some other 2DnMat, BP lacks stability under ambient and physiological conditions. Zhao *et al.* demonstrated through simulation that BP can be successfully passivated *via* the self-assembly of an organic molecule, perylene-3,4,9,10-tetracarboxylic dianhydride (PTCDA).[159] BP films have been obtained by self-assembly based on the Langmuir–Blodgett technique.[160] Yu *et al.*[140] encapsulated black phosphorus quantum dots in a hydrophobic micelle to improve the targetability for cancer phototherapy using self-assembly. The formed structures were hydrophobic micelles composed of 3 layers: an outer layer of PEG-*b*-PAsp, a middle layer of PPS, and an inner layer of SAHA. Zhang *et al.*[65] assembled a spherical Janus structure of black phosphorus quantum dots coated with Cu^{2+} ions and THQ, using metal ion-induced self-assembly promoted by the Cu^{2+} ions. The formed nanoparticles combined sensitivity to radiation and stability in water and physiological conditions.

Li *et al.*[141] coated Ag_2S QDs and tellurium nanorods (TeNRs) using polypeptide-induced self-assembly on a core of a polypeptide-engineered $PC_{10}ARGD$, which created a molecule with a diameter of 160 nm and a thickness of 9.4 nm responsive to external magnetic fields, to be used as a tool for chemotherapy and to induce ROS production.

Iron-based nanomaterials are used with significant prevalence and are self-assembled with other nanomaterials to improve or to give the nanostructure good magnetic responsiveness for various biomedical applications. Mandal *et al.*[67] constructed a particle capable of leading to effective angiogenesis, mainly self-assembled by magnetic fields. The organic–inorganic hybrid system was a tubular magneto-nanoparticle of 2 layers, the outer layer being composed of Fe_3O_4 magnetic nanoparticles, while the inner layer was composed of hydrophilic polyacrylic and enriched with polycaprolactone, with a zeta potential of 20 mV and a diameter of 2–5 μm. The polyacrylic improved bio-adhesion and biocompatibility while

Table 1 Recent studies on self-assembled inorganic nanomaterials, their physicochemical properties, and interactions involved in the process of self-assembly

Material	Main properties	Main self-assembly mechanisms/Interactions and formed structure	Ref.
DOX-EGF-SA-AuNPs	Diameter = 78.8 nm Ratio of HS-pH-DOX to AuNPs 200 : 1 DOX loading capacity = 16% Nanoparticles target specific receptors on cancer cells pH and L-glutamine dependent drug release	Type: not specified Interactions: HS-PEG-SH mediated Structure formed: gold nanospheres loaded with EGF and DOX	138
Au-Fe_3O_4 NPs	Diameter = 110–115 nm Amphiphilic block of copolymer brushes The weight fraction of the polymers coated on Janus NPs is 35% Strong NIR absorption and magnetic properties Stable in water, PBS and cell culture medium	Type: hierarchical self-assembly Structure formed: two kinds of double-layered plasmonic-magnetic vesicles, with Au or Fe_3O_4 localized on the exterior and in the interior	59
AuRNs-CpG-DOX	Diameter = 91.5 nm Zeta potential = 18.6 mV Loading capacity = DOX 1500 : 1 AuNRs Drug release is responsive to NIR, Biocompatible and stable in physiological conditions	Type: chemical self-assembly Interactions: hydrogen bonds (DNA hybridization) Structure formed: gold nanorods coated with Y-shaped CpG DNA intercalated with DOX and with PEG	139
BP QDs@PPS	Diameter = 146.2 nm ± 0.026 Zeta potential = −31.4 ± 3.8 mV Stable molecule and biocompatible BPQDs loading rate = 2.95% Drug release is pH dependent, acidic conditions increase the release rate Stable in plasma	Type: not specified Structure formed: Hydrophobic micelles composed by an outer layer of PEG-b-PAsp, a middle layer of PPS and an inner layer of SAHA	140
CCM@AT	Diameter = 160 nm Shell thickness = 9.4 nm Ag_2S 1 : 1 TeNRs ratio Zeta Potential = −28.6 mV Stable in water PBS and cell culture medium	Type: not specified Structure formed: cancer cell membrane-coated with Ag2S QDs and TeNRs, which encapsulates PC_{10}ARGD and Na_2TeO_3, the attributed name of the developed complex was CCM@AT	141
CDDP : GO	Diameter = 90–120 nm CDDP 1.5 : 1 GO: ratio Specific, with low toxicity to healthy cells Stable in water	Type: hierarchical self-assembly Structure formed: 3D nanosphere coated with proflavine and DOX	60
CF@Mxene@ZnO	Layer spacing = 0.64 nm Mxene is used as an inner dielectric layer to cover the core-sheath composite Good metallic electrical properties, shows a positive response for conduction loss	Type: hierarchical self-assembly Structure formed: a 3D nanocomposite core-sheath with an inner layer made of carbon fiber (CF), a middle layer made of Mxene and ZnO as the outer layer	61
DEA-f-Gr-*f*-ODA	Diameter = 550 nm Thickness = 20 nm Potential zeta = −12.3 mV Amphiphilic particles CPT loading efficiency = 31.5% Biocompatible and dispersible in water and organic solvents Stable in water	Type: not specified Structure formed: 3D nanosheet coated with DEA and ODA	142
DNA/MoS_2-NS	Length = 100 nm Thickness = 2–4 nm Sensitive to cancer cells increased ATP metabolism Drug release dependent on the concentration of ATP Biocompatible Stable in water and culture medium	Type: layer-by-layer self-assembly Structure formed: testudo like superstructure with various layers of MoS_2	62
ELK1-GO	Diameter at 45 °C = 2000 nm Internal diameter = 50 µm Thickness > 10 µm GO 1 : 40 ELK1	Type: hierarchical self-assembly Structure formed: 3D nanotubes, defined by a core-shell model The core is formed by GO and the shell by ELK1	6
F-apt/SWNT	Length = 50–150 nm Good dispersibility in various media Stable in water, PBS and culture medium	Type: noncovalent self-assembly Structure formed: single walled carbon nanotube (SWNT) coated with fluorophore-labeled aptamer, namely Cy5-Sgc8c	143
Fe2O3@GO MitP-TF	Length = 50–100 nm Thickness = 1–2 nm Superparamagnetic and photothermal behavior, Biocompatible, Highly specific	Type: *in situ* magnetic self-assembly Structure formed: 2D nanosheet composed of superparamagnetic graphene oxide, tumor targeting transferrin, and mitochondrial peptide	66

Table 1 *(Contd.)*

Material	Main properties	Main self-assembly mechanisms/Interactions and formed structure	Ref.
NGO-HDex	Diameter = 238 ± 19.67 nm Zeta potential = −11.7 ± 1.69 mV GO 2 : 1 Hdex Drug loading capacity = 3.4 mg mg^{-1} Stable in PBS and culture medium	Type: not specified Interaction: π–π stacking Structure formed: 2D nanohybrid sheet composed of GO, and Hdex	43
GQDs-Mn_3O_4 w/RhB dye	Diameter = 2–4 nm Biocompatible and stable in water Absorbs radiation at a wavelength from 210–710 nm	Type: metal ion induced self-assembly Structure formed: graphene-quantum dots coated with Mn_3O_4	64
MION	Diameter = 103 nm Zeta potential = 34 mV Photothermal conversion efficiency = 71% Biocompatible and stable in physiological conditions, Stable in water	Type: PEGylation (weak interactions) Structure formed: condensed iron oxide nanocrystal with PEG, amino groups and a NIR dye	144
Graphene nanoplatelets	Diameter = 20 μm	Type: layer-by-layer self-assembly Structured formed: multi-layered sheet of graphene and KMPR, coated with various cancer biomarkers	63
HAP/CS/HA/Mxene/ AuNRs/DOX	Diameter = 2–3 μm Zeta potential = −3.8 ± 0.4 mV. Drug encapsulation efficiency = 83.9% pH and light dependent drug release Photothermal efficiency = 20.42% for HAP/CS/HA/Mxene/ AuRNs and 13.76% for HAP/CS/HA/Mxene, Biocompatible	Type: layer-by-layer self-assembly Structure formed: hybrid microcapsules, with an inner layer of hydroxyapatite, coated with PSS/CS/HACS, Mxene AuNRs and DOX	46
Hap@PDA/AuNR	Diameter = 2 μm Zeta potential = 15.1 ± 0.7 mV Drug loading efficiency = 95.6% Biocompatible, pH dependent drug loading and release	Type: not specified Interaction: electrostatic Structure formed: H-HAP/PDA hybrid shell	145
Janus BP QDs/metal-organic nanoparticles	Diameter = 25 nm The J-MOPs absorbs radiation at 500 nm Radiation sensitive, stable in physiological conditions, and dissolved in acidic conditions, J-MOPs generates ROS and release Cu^{2+} ions in the tumor Stable in water	Type: metal ion induced self-assembly Structure formed: spherical structure of BPQDs coated with Cu^{2+} ions and THQ	65
MMT	Diameter = 5–10 μm Zeta potential = 20 mV The magnetic nanoparticles tethered tetra-armed BCP are an organic-inorganic hybrid system The nanocomposite is pH and magnetic responsive and allows bio-adhesion	Type: magnetic self-assembly Interactions: intra and intermolecular H-bonding Structure formed: tubular magneto-nanoparticles, of two layers	67
MnO_2@PtCo nanoflowers	Diameter = 200 nm MnO_2@PtCo nanoflowers have excellent catalytic efficiency PtCo nanoparticles had a molar ratio Pt/Co of 3 : 1 MnO_2 4 : 1 PtCo Good dispersibility and stability in physiological conditions Stable in culture medium	Type: not specified Structure formed: biomimetic nanoflowers of nano enzymes	146
MoS2	Length = 40–240 nm. Potential zeta = −16 mV High affinity for cancer cell receptors, produces ROS if irradiated Good stability in a vast range of pH (3–10), Stable in water	Type: not specified Interactions: supramolecular, van der Waals Structure formed: supramolecular glycosheet, of 2D MoS_2 nanosheets coated with glycoprobes	147
MoS_2 aggregates and sheets	Hydrodynamic radius = 141 nm Lateral dimension = 100 nm Zeta potential = −18 ± 1 mV The aggregates are NIR responsive Biocompatible, Stable in water and culture medium	Type: not specified Structure formed: cotton-candy aggregates made of MoS_2 coated with albumin	148
MoS_2-GSH-CYS-PF127	Diameter = 102 nm Zeta Potential = 9.4 mV The drug release related to particle morphology change The drug loading capacity = 51.36%. Biocompatible, Stable in water	Type: self-assembly by dialysis Structure formed: spherical homogenous core of MoS_2-GSH-PF127 coated by CYS	149
Mxene/C3N4	Thickness = 2 nm Zeta potential = 7.6 mV Allowed PDT and PTT under hypoxic conditions Photothermal conversion efficiency = 40.8% Biological and stable in physiological conditions Stable in water, PBS, and cell culture medium	Type: electrostatic self-assembly Structure formed: two dimensional heterostructure in form of nanosheet made of Ti_3C_2/g-C_3N_4	150

Table 1 *(Contd.)*

Material	Main properties	Main self-assembly mechanisms/Interactions and formed structure	Ref.
N^+/Graphene	Diameter = 5–10 μm Length = 100–400 μm, Biocompatible	Type: hydrothermal self-assembly method Structured formed: 3D nanoparticle formed by multilayers of graphene	151
nGO@DOX-cPEG	Diameter = 113.3 nm Zeta Potential = 25 mV, DOX release was significantly higher under acidic conditions. Loading capacity ~70% Stable in PBS and cell culture medium	Type: not specified Structured formed: flakes of nGO@DOX-cPEG, coated with DOX	152
nHA-rGO/nHA-GO	nHA 1 : 5 GO ratio Pore size = 80 μm Lateral dimensions = 1.66 μm Thickness = 1.15 nm	Type: not specified Structure formed: hydrogel with 3D porous scaffolds composed of either reduced graphene oxide or graphene oxide and nHA	153
PNIPAM-peptide-Au	Diameter = 120–300 nm Zeta potential = −20 mV Responsive to temperature changes, Biocompatible	Type: not specified Structure formed: Nanospheres formed of PNIPAM decorated with peptide-Au	154
RuZ, cyclometalated Ru(II)	Hydrodynamic radius = 135 nm (in culture medium) Zeta potential = −8.1 mV Self-assembly decreases the oxygen consumption and inhibits glycolysis Stable in water and cell culture medium	Type: not specified Interaction: electrostatic and π–π interactions Structure formed: Nanoaggregate like a nanosphere made of RuZ	155
TC@Ch-MFO	Diameter = 500 nm Zeta potential = 2.5 mV Photothermal conversion efficiency = 22.4% Photostability, biocompatibility, conductivity, and pH dependent drug release profile	Type: not specified Interaction: cross linking with chitosan Structure formed: TC@Ch-MFO, is formed by $MnFe_2O_4$ nanospheres coated with Ti_3C_2	156
Ti_3C_2@GNRs/PDA/Ti_3C_2	Lateral size = 250 nm Thickness = 25.3 nm Zeta potential = −53.1 mV Photothermal conversion efficiency = 45.89% DOX loading efficiency = 95.88%, pH dependent drug release with NIR	Type: not specified Interaction: π–π stacking Structure formed: hybrid nanostructure of Ti_3C_2@GNRs/PDA/Ti_3C_2	157
V_2O_5@pDA@MnO_2	Size = 300 nm Removes harmful ROS Biocompatible and high stability, under physiological conditions High enzymatic capacities	Type: not specified Structure formed: nanocomplex Y-shaped, of V_2O_5 coated with pDA and MnO_2 nanoparticles	158

4T1: murine carcinoma cells; 5-FU: 5-fluorouracil; AIBI: 2,2-azobis[2–2-imidazolin-2-ylpropane] dihydrochlorine; AuNRs: gold nanorods; AuNS: gold nanostars; BMD: bone mineral density; BMD: bone mineral density; BPQD: black phosphorus quantum dots; CDDP: cisplatin; CF: carbon fibre; CpG: unmethylated cytosine-guanosine; CPT: anticancer drug camptothecin; CPT: hydrofobic camptotheein; CS: chitosan; Cy5.5: cyanine5.5; CYS: cystine; DEA: diethanolamine; DODAB/DOPE: dimethyldioctadecylammonium bromide/1,2-dioleoyl-*sn*-glycero-3-phosphoethanolamine; DOX: Doxorubin; EGCG: -Epigallocatechin-3-gallate; EGF: Epidermal growth factor; ELRs: elastin-like recombiners; F-apt: fluorophore-labelled aptamer; GO: graphene oxide; GQDs: graphene quantum dots; Gr: graphene; ODA: oleylamine; GSH: glutathione; H22: mouse hepatocellular carcinoma cell line; HA: hyaluronic acid; HDACis: histone deacetylase acetylase inhibitor; HDex: hematin-terminated dextran; HEK293T: human embryonic kidney cells; HLECs: human lymphatic endothelial cells; IC_{50}: half maximal inhibitory concentration; ICG: indocyanine green; KRASl: mutant anticancer K-Ras gene plasmid; LBL: layer-by-layer; MAPM: magnetically active polymeric micelle; MCF-7: human breast cancer cells; MitP: mitochondrion-targeting peptide; MMT; magnetic micro-tubular material; MNP: magnetic nanoparticles; MOPs: metal organic particles; N/A: not applicable; NAC: *N*-acetylcysteine; nHA: hydroxyapatite; NIR: near infrared radiation; ODNs: oligodeoxynucleotides; PBS: phosphate buffered saline; PC-3: human prostate cancer cells; pDA: polydopamine; PDT: photodynamic therapy; PE-PCL: pentaerythritol poly(ε-caprolactone); PEG: polyethylene glycol; PEI: polythylene imine; PNIPAM: poly(*N*-isopropyl acrylamide); PS: polystyrene; PTT: photothermal thrapy; PU: elastic polyurethane; PVA: polyvinyl alcohol; QD: quantum dots; rGO: partially reduced graphene oxide; RhB: Rhodamine B; ROS: reactive oxygen species; RuZ: cycloruthenated complex; SA: self-assembled; SAHA: Suberoylanilide hydroxamic acid; SWNT: single walled carbon nanotube; T80: Tween 80; TeNRs: tellurium nanorods; TF: transferrin (tumor targeting protein); THQ: tetrahydroxyanthraquinone; TLR: toll-like receptors; TPP: Triphenyl phosphonium bromide.

maintaining effective pH and magnetic responsiveness. Liu *et al.*[66] produced magnetic graphene oxide nanosheets-based complexes (L-Fe_2O_3@GO-MitP-TF) functionalized with the tumor-targeting protein transferrin (TF) and with the mitochondria-targeting peptide (MitP), which presented sizes ranging from 0.5 to 1 μm. Those particles were capable of *in situ* self-assembly on tumor cells, being able to confine them and preventing both invasion and metastasis *in vitro* and *in vivo*. Furthermore, they allowed tumor eradication under photothermal therapy (NIR irradiation). A schematic illustration is shown in Fig. 7.

Carbon-based nanomaterials, such as fullerenes, quantum dots, nanotubes, or nanosheets, are ideal for various biomedical applications and usually allow versatile functionalization. Georgitsopoulou *et al.*[142] developed a Janus-type graphene nanosheet coated with oleylamine (ODA) and diethanolamine (DEA). After the assembly of the nanocomplex, camptothecin (CPT) was loaded at its surface. The 3D struc-

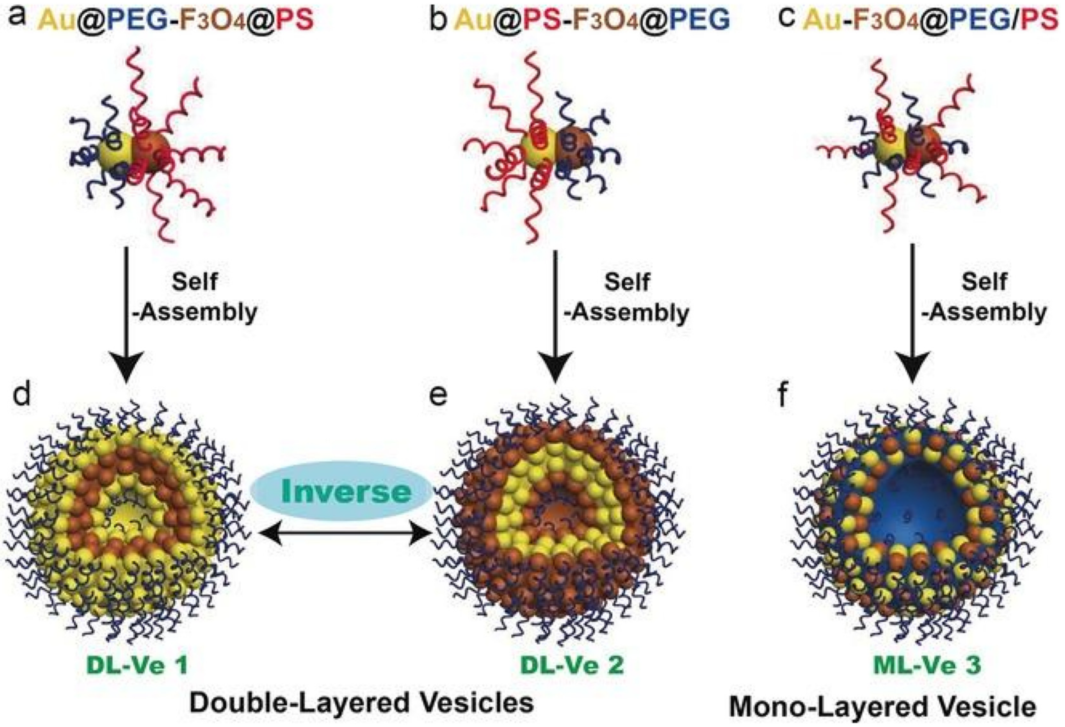

Fig. 6 Schematic illustration of Janus Au-Fe_3O_4 NPs. Nanoparticles were grafted with hydrophilic polyethylene glycol (PEG) on Au and hydrophobic polystyrene (PS) on Fe_3O_4 (a), with PS on Au and PEG on Fe_3O_4 (b), and with binary mixed PEG and PS (c), and the hierarchical self-assembly of the resulting three kinds of Janus amphiphilic nanoparticles into double-layered plasmonic–magnetic vesicle 1 (d) and 2 (e) and mono-layered vesicle 3 (f) in aqueous media. Reproduced with permission,[59] 2017, John Wiley and Sons. Abbreviations: PEG, hydrophilic polyethylene glycol; PS, hydrophobic polystyrene.

ture presented a hydrophilic surface, coated with the mentioned polymers, and a hydrophobic interior of graphene only, having a diameter of 547.5 nm and a zeta potential of −12.3 mV.

Han *et al.*[61] used hierarchical self-assembly to form a structure with an outer layer of ZnO and a core of carbon fiber (CF) previously self-assembled with $Ti_3C_2T_x$ flakes by electrostatic interactions, as depicted in Fig. 8. The 3D structure formed was composed of layers with a spacing of 0.64 nm, with a dielectric layer, and a positive response to conduction loss.

Various 3D carbon-based structures have been developed for numerous biomedical applications, especially for applications and treatments based on phototherapy and chemotherapy. Nandi *et al.*[60] reported hierarchical self-assembly, transforming 2D graphene nanosheets into a 3D nanosphere stacked with proflavine and doxorubicin with a diameter of 90 to 120 nm. The proflavine and doxorubicin first bind to the graphene oxide (GO) nanosheets, followed by cisplatin, forming bonds with the prior-mentioned molecules. Lastly, cisplatin bonds to other cisplatin molecules present on separate nanosheets, forming the 3D structure. Wu *et al.*[6] reported hierarchical self-assembly to tightly control the interactions between GO, as the main building block, and proteins like elastin-like recombiners (ELRs). The study shows an effective functionalization of GO with ELK1. The resulting structure follows a classic core–shell model with a diameter of 50 μm and thickness of 10 μm. Cao *et al.*[151] assembled multilayers of 2D graphene nanosheets into a 3D structure using a hierarchical self-assembly method. The researchers developed a graphene scaffold with enough porosity to promote cell growth and proliferation. Afterward, the author improved hydrophobicity and water stability by introducing hydrophilic groups like N^+ using physical ion implantation. These particles were stable in water, biocompatible, and had a diameter of 5 to 10 μm.

2D graphene structures and other nanomaterials, such as black phosphorus, transition metal carbides, MXenes, and TMDs, among others, have gained increased attention in the biomedical field.[34,35] Their properties at the nanoscale differ from their bulk counterparts due to the high volume-to-surface ratio observed on smaller scales.[35] Jin *et al.*[43] created a nanocarrier based on the partial reduction and functionalization of GO with hematin-dextran conjugated (HDex) and loaded with DOX. The authors state that the self-assembly of GO with HDex occurred through π–π stacking of GO and hematin, however, the type of self-assembly isn't specified. The compound showed a DOX loading capacity of 3.4 mg mg^{-1}, presenting a pH-dependent release, having a zeta potential of −11.7 mV, and a size of 238 nm. Yan *et al.*[143] self-assembled a structure based on single carbon nanotubes, using mainly noncovalent self-assembly. Fig. 9 shows that this carbon-based nanomaterial was coated with the Cy5-Sgc8c aptamer, which conferred the nanostructure good bio-

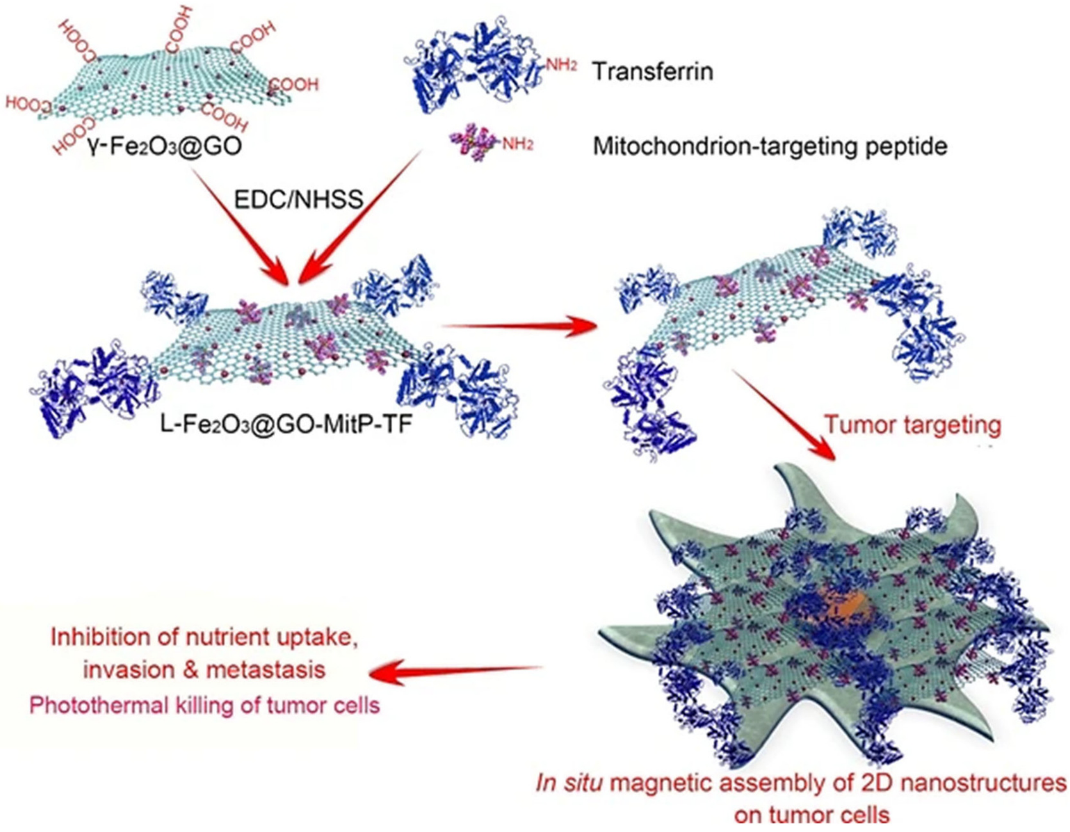

Fig. 7 Magnetic graphene oxide-based nanosheet complexes (L-Fe_2O_3@GO-MitP-TF) production and their *in situ* magnetic 2D self-assembly on tumor cells for cancer therapy. Reproduced with permission,[66] 2020, Springer Nature. Abbreviations: EDC, 1-ethyl-3-[3-dimethylaminopropyl] carbodiimide; NHSS, *N*-hydroxysulfosuccinimide.

compatibility, dispersibility in water, and specificity for cancer cells.

Lan *et al.*[64] functionalized graphene quantum dots (GQDs) with Mn_3O_4 by metal ion-induced self-assembly to improve the efficiency of surface-enhanced Raman scattering (SERS) to enable the identification of molecular species that are present in cancer cells. The Mn_3O_4 was used to connect the GQDs and diminish their fluorescence while maintaining the Raman signal properties. The structure had a diameter of 2–4 nm and absorbed radiation at a wavelength ranging from 210 to 710 nm. Zhang *et al.*[63] used layer-by-layer self-assembly to develop a structure with a diameter of 20 μm, comprised of multiple layers of graphene coated on the outside with various cancer biomarkers to increase specificity. Thapa *et al.*[152] developed PEGylated flakes of graphene oxide *via* a non-specified self-assembly modality. The nanoparticles had a diameter of 113.3 nm and a DOX loading capacity of 70%.

Reduced graphene oxide (rGO) has also been used for numerous biomedical applications. It is obtained from GO using chemical, thermal, photo, or electrochemical reduction procedures that decrease its oxygen-containing functional groups content. This partially restores optical absorbance and electrical and thermal conductivity, which is relevant for photothermal therapy (PTT) applications. However, rGO becomes more hydrophobic, decreasing aqueous stability when compared with GO.[161] Li *et al.*[153] built a scaffold composed of nano-hydroxyapatite (nHA) and rGO. The dispersion containing 20 wt% nHA-rGO formed a hydrogel with a pore size of 80 μm. The nanosheets had a lateral dimension of 1.66 μm and a thickness of 1.15 nm.

MnO_2, MoS_2, and $MoSe_2$ are other examples of inorganic materials that have been used to build nanostructures through self-assembly with various other molecules. Some authors have used MnO_2 as a base nanomaterial or as a coating material to improve the photothermal conversion efficiency, using hierarchical self-assembly.[146] Wang *et al.*[146] built a highly ordered MnO_2 nanoflower coated with uniformly dispersed PtCo nanoparticles. This nanostructure was formed by taking advantage of the large amount of free functional groups on the surface of PtCo which directed the growth of MnO_2 nanoflowers. The final structure (MnO_2@PtCo) had good water dispersibility, a diameter of 200 nm, and a MnO_2 to PtCo molar ratio of 4 : 1. MoS_2 was used by multiple researchers as the main nanomaterial to form nanosheets coated with glycosheets,[147] cotton candy aggregates coated with albumin,[148] a spherical core coated with CYS,[149] and a testudo-like structure of MoS_2,[62] when self-assembled through supramolecular self-assembly, desolvation self-assembly, colloidal self-assembly by

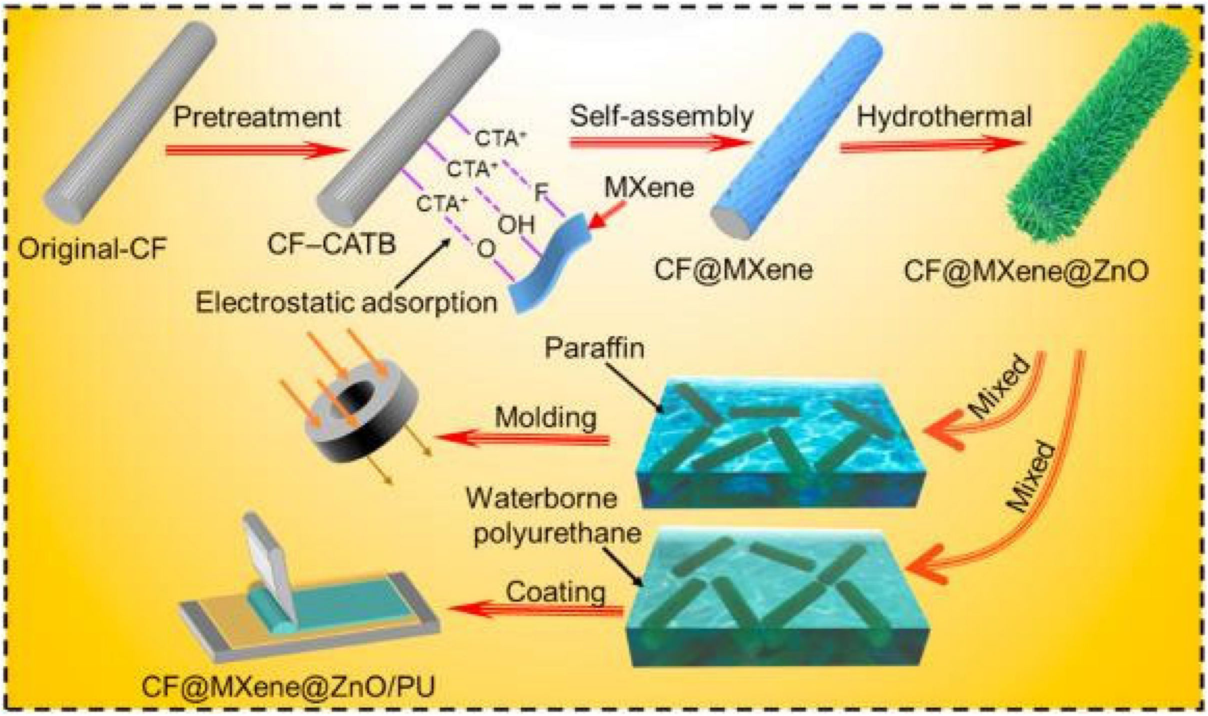

Fig. 8 Illustration of the synthetic process of CF@MXene@ZnO (CMZ) microrods and CMZ/PU composites. Firstly, the pretreated CF was modified with a positive charge by CTAB and then dispersed in a multilayered $Ti_3C_2T_x$ suspension. $Ti_3C_2T_x$ flakes assembled on the surface of CTAB-modified CF (CF-CTAB) successfully due to the abundant surface terminal groups (−OH, −F, −O). Finally, the pretreated CF was completely coated by $Ti_3C_2T_x$ MXene, forming the uniform MXene sheath. 3D ZnO flowers were then grown on the CM through the typical hierarchical self-assembly process to decorate CF@MXene. The obtained CMZ fillers were then added into waterborne PU uniformly to fabricate flexible composite coatings by coating the as-prepared solution repeatedly. Reproduced with permission,[61] 2021, Elsevier Ltd. Abbreviations: CF, carbon fiber; CTAB, cetyltrimethylammonium bromide; PU, polyurethane.

dialysis, and layer-by-layer self-assembly, respectively. Ji *et al.*[147] developed a nanostructure based on MoS_2 nanosheets coated with glycosheets composed of various glycoligands, like galactose, *N*-acetyl galactosamine, and lactose. The molecule had a size ranging from 40 to 240 nm, a zeta potential of −16 mV, demonstrated high affinity for cancer cell receptors, and induced ROS production upon irradiation. The nanoconstruct was built through supramolecular self-assembly. Ramana *et al.*[148] assembled a cotton candy-like nanostructure composed of MoS_2 sheets, which were self-assembled through a desolvation method for theranostics purposes. The lateral dimension and the hydrodynamic radius of the cotton-candy aggregates were 100 nm, and 141 nm, respectively.

Vadivelmurugan *et al.*[149] developed a bio-responsive MoS_2-based nanocomposite. This nanomaterial was composed of Pluronic F127, Cystamine (CYS), Glutathione (GSH), and MoS_2. The final conformation of the nanocomposite was a (MoS_2-GSH-CYS) shell with F127 and DOX at the surface of the nanoparticle. First, the researchers produced the MoS_2-GSH nanoparticles using a dimethyl sulfoxide (DMSO) solution. Afterward, F127 and CYS were self-assembled to the MoS2-GSH nanocomplex. Particles presented a hydrodynamic size of 82.3 nm, a zeta potential of 1.7 mV, and revealed good biocompatibility, a drug loading capacity of 51.36%, and stability in water. These were efficient for drug delivery in a GSH-rich environment. Li *et al.*[62] produced a nanostructure (DNA-MoS_2 NS) using layer-by-layer self-assembly. The assembly of this complex nanostructure was guided by DNA molecules bonded to the nanosheets through sulfur atom defect vacancies. After the establishment of the mentioned bonds, the DNA particles present on different nanosheets bind to other DNA molecules. The lateral size of the complex was 100 nm, having a thickness of 2–4 nm. Nanoparticles presented high sensitivity to ATP concentration increase and good biocompatibility.

Zhang *et al.*[150] used electrostatic self-assembly to develop heterogeneous 2D nanosheets made of Ti_3C_2/g-C_3N_4, coated with triphenyl phosphonium bromide (TPP), as illustrated in Fig. 10. 2D nanosheets had a thickness of 2 nm, a zeta potential of 7.6 mV, and a photothermal conversion of 40.8%. They were also biocompatible and stable in physiological conditions.

Electrostatic self-assembly has been used by various researchers to produce diverse inorganic and hybrid nanostructures. Li *et al.*[155] assembled a nanosphere of RuZ with a hydrodynamic size of 135 nm, a zeta potential of −8.1 mV, and good stability in cell culture medium. The main interactions in this self-assembly process included electrostatic and π–π interactions. Wu *et al.*[156] self-assembled a TC@Ch-MFO nano-

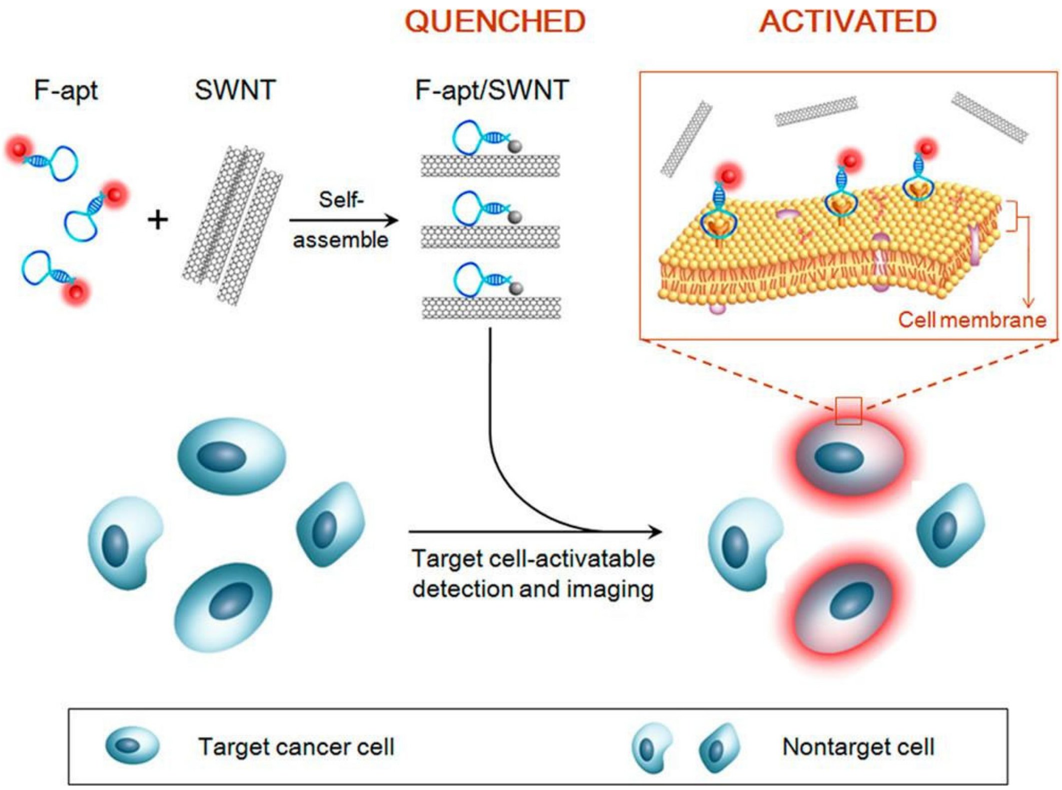

Fig. 9 Activatable fluorescence probing strategy for targeting cancer cells based on self-assembled fluorophore-labelled aptamer/single-walled carbon nanotube (F-apt/SWNT) ensembles. Cancer-targeted F-apts are used as recognition molecules, and the SWNT are used as nanoscaffolds for the aptamers and nanoquenchers of dyes. Reproduced with permission,[143] 2014, American Chemical Society. Abbreviations: F-apt, fluorophore-labelled aptamer; SWNT, single-walled nanotube.

structure, using a crosslinker, namely chitosan to integrate phototherapy and imaging techniques. The nanomaterial was constituted by $MnFe_2O_4$ nanospheres coated with Ti_3C_2, having a diameter of 500 nm, zeta potential of 2.5 mV and photothermal conversion of 22.4%. This nanoparticle was also electrically conductive, biocompatible and presented pH dependent drug release. Cao *et al.*[145] used electrostatic self-assembly, performing a hydrothermal transformation method, to develop hybrid hollow microcapsules of HA/PDA/AuNRs. A hollow sphere made of $CaCO_3$ was fabricated using a fast precipitation method. Afterward, hydroxyapatite was added to the microspheres as a coating and, through a solvothermal process, and $CaCO_3$ was removed while maintaining the external sphere of hydroxyapatite. Gold nanorods and dopamine were used to coat the surface of the nanomaterials by suspending the spheres in a solution of Tris-HCL buffer and dopamine hydrochloride. Lastly, the produced microspheres were coated by immersion in a gold nanorod solution followed by centrifugation. The particles presented a diameter of 2 μm and zeta potential of −15.1 mV, stability in physiological conditions, photothermal stability, a DOX drug loading efficiency of 95.6%, and pH responsiveness. The self-assembly process described above is illustrated in Fig. 11.

Li *et al.*[153] constructed a composite scaffold of rGO sheets and nano-hydroxyapatite (nHA). The scaffold presented a pore size of 80 μm and a thickness of 1.15 nm. This material was responsive to NIR irradiation and induced an increase in bone mineral density after eradicating the tumor. Huang *et al.*[158] developed a nanostructure (V_2O_5@pDA@MnO_2) formed by nanowires of V_2O_5 coated with a layer of polydopamine that was used to mimic glutathione peroxidase and as an efficient link between the nanowire and the MnO_2 nanoparticles. The MnO_2 nanoparticles were used to mimic superoxide dismutase (SOD) and catalase (CAT). Initially, V_2O_5 and dopamine were added to Tris-HCl buffer with ethanol, and after stirring and centrifugation, the formed V_2O_5@pDA complex was heated to 80 °C, and aqueous $MnSO_4{\cdot}6H_2O$ was added to the heated solution. This nanomaterial had a size of 300 nm and showed high biocompatibility and stability in physiological conditions.

Wu *et al.*[46] self-assembled a pH/NIR multi-responsive drug delivery system based on hydroxyapatite (HAP), chitosan (CS)/hyaluronic acid multilayers, gold nanorods (AuNRs), and an MXene (Ti_3C_2). The nanoconstruction method applied was layer-by-layer self-assembly. Particles had a diameter of 2–3 μm, a zeta potential of −3.8 mV, a DOX encapsulation efficiency of 83.9%, and a photothermal efficiency of 20.42%. Zhu *et al.*[157] manufactured a multilayer Ti_3C_2 MXene-based nanoplatform, Ti_3C_2@GNRs/PDA/Ti_3C_2. The authors state that self-assembly was made mainly through π–π stacking. The par-

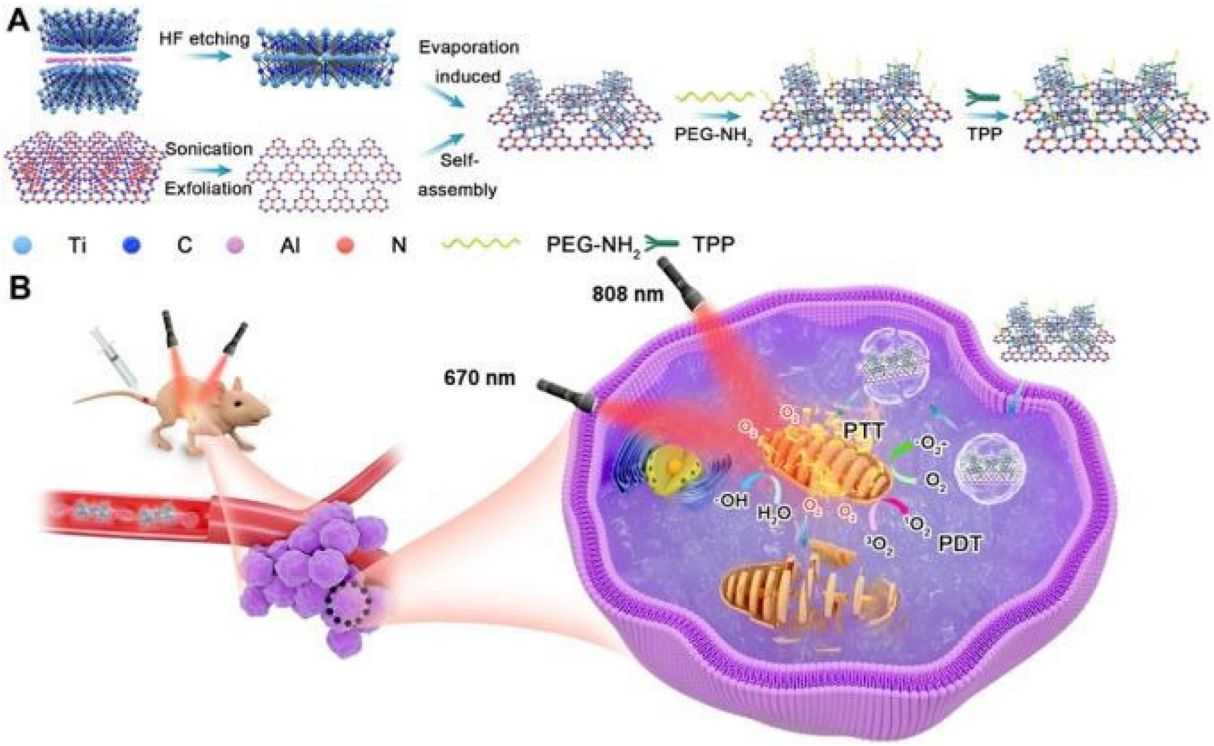

Fig. 10 Electrostatic assembly of a two-dimensional Ti_3C_2/g-C_3N_4 heterostructure for photothermal and photodynamic therapy. The self-assembled nanoparticle resulted from the conjugation of Ti_3C_2 and g-C_3N_4 and subsequent surface modification with PEG-NH_2 and TPP. Under 670 nm laser irradiation, the nanocomplex can produce reactive oxygen species through electron transfer. As a result, various pathways of PDT are activated under normoxic and hypoxic conditions. The illustrations also exemplify the capability of the nanocomplex to induce effective PTT after being irradiated at an 808 nm wavelength. (A) Schematic of Ti_3C_2/g-C_3N_4-TPP NSs production. (B) Schematic illustration of Ti_3C_2/g-C_3N_4-TPP mitochondria-targeted PDT and PTT effect. Reproduced with permission,[150] 2020, Elsevier Ltd. Abbreviations: PEG-NH_2, polyethylene glycol-amine; PDT, photodynamic therapy; PTT, photothermal therapy; TPP, triphenylphosphonium bromide.

ticles produced had a lateral size of 250 nm, a height of 25.3 nm, a zeta potential of −53.1 mV, a photothermal conversion of 45.89%, stability in water and cell culture medium, and good biocompatibility.

4. Biomedical applications of self-assembled inorganic nanomaterials

4.1 *In vitro* studies

Many inorganic nanomaterials have been self-assembled and studied for biomedical applications. Table 1 (self-assembly methods) and Table 2 (surface modification and biomedical component) congregate the most relevant *in vitro* studies involving self-assembled inorganic nanoparticles for biomedical applications up to date. Song *et al.*[59] developed Janus amphiphilic Au–Fe_3P_4 nanoparticles (Au@PEG-Fe_3O_4@PS) to improve the deficiencies of traditional imaging techniques. Both surfaces of the particle were modified with different polymers, making the Au surface hydrophilic and Fe_3P_4 hydrophobic. This material did not present any toxicity towards U87MG cells and increased image contrast and definition. Other applications of gold nanoparticles include PDT and chemotherapy.[138,139,145,154,162] Various studies use 808 nm laser light radiation (1–2 W cm^{-2}) for 5–20 minutes to decrease cancer cell viability to 6.5–20%. Tao *et al.*[139] developed a multifunction platform composed of gold nanorods coated with Y-shaped unmethylated cytosine-guanosine CpG, PEG, and encapsulated DOX. AuNRs-CpG-DOX (250 pM) was irradiated with a NIR laser (808 nm, 1.5 W cm^{-2}, 10 min) leading to a temperature increase above 42 °C, reducing murine hepatocellular carcinoma H22 cells viability to 10%. Zhang *et al.*[154] developed a drug delivery system with imaging capabilities based on PNIPAM nanospheres and Au clusters. DOX release was triggered by alteration of PNIPAM chains 3D configuration caused by temperature increase. Tests in the human cervical cancer HeLa cells revealed no toxicity for concentrations between 0.04–2.5 μmol L^{-1}, with lysosomal accumulation being observed. Cao *et al.*[145] developed hybrid microcapsules by electrostatic self-assembly, composed of hollow HA/PDA/AuNRs to be used as a tool for drug delivery. The microcapsules presented sensitivity to NIR and also pH responsiveness. HAP/PDA/AuRNs/DOX dispersions (50 μg mL^{-1}) under NIR laser irradiation (808 nm, 4 W cm^{-2}) increased temperature by 37.5 degrees with 40% DOX being released, while it reduced the human breast cancer cells MCF-7 cells viability to 40%. Feng *et al.*[138] constructed a nanomaterial composed of

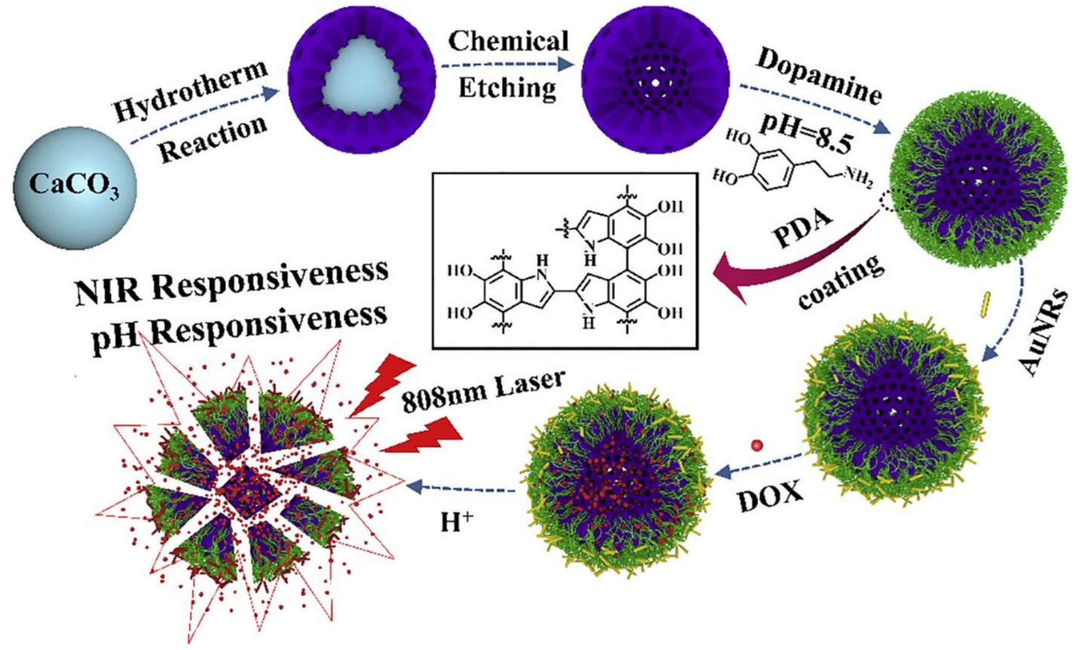

Fig. 11 Electrostatic self-assembly of H-HAP/PDA/AuNRs hybrid vehicles for drug delivery. HAP was synthesized by a hydrothermal transformation method, which was applied to $CaCO_3$ microspheres. Afterward, dopamine was self-polymerized on the surface of the mesoporous HAP in an alkaline environment. Then, AuNRs were coated on the surface of the H-HAP/PDA nanoparticles using electrostatic interactions. Finally, DOX was loaded into the H-HAP/PDA/AuNRs hybrid microcapsules. Reproduced with permission,[145] 2020, Elsevier B.V. AuNRs, gold nanorods; $CaCO_3$, calcium carbonate; HAP, hydroxyapatite particles; NIR, near-infrared radiation; PDA, polydopamine; ROS, reactive oxygen species.

gold nanoparticles assembled by cross-linking with dithiol-polyethylene glycol (HS-PEG-SH) coated with epidermal growth factor (EGF). DOX-EGF-SA-AuNPs were designed to selectively target brain tumor cells and destroy them by delivering DOX. Drug release was found to be pH dependent and sensitive to high vascularity, targeting specific receptors found in U87 brain tumor cells. L-Glutamine (GSH) present inside tumor cells triggered a complete breakdown, changing the morphology of the nanocarrier to a single gold nanorod. Fig. 12 illustrates that the nanomaterial showed good biocompatibility and presented a DOX loading capacity of 16%. The human glioblastoma U87 cell viability was reduced to 50% after treatment with DOX-EGF-SA-AuNPs.

Liu *et al.*[66] constructed a hybrid nanoparticle (Fe_2O_3@GO-MitP-TF) for cancer PTT. A549-RFP cells were incubated with the nanocomposite (50 mg mL^{-1}) and irradiated with a NIR laser (808 nm, 20 W cm^{-2}) for 4 min. Temperature increased from 27 °C to 60 °C, inducing a reduction of intracellular ATP levels in tumor cells, and viability decreased to values under 20%. Mandal *et al.*[67] developed a magnetic nanoparticle-based micro-tubular material (MMT) that could induce cellular adherence to assist in angiogenesis. The hybrid nanoparticles were responsive to changes in the environmental pH and magnetic fields. Eight hours after treatment, the number of HeCaT cells adhered was 2.8×10^5, 4.1×10^5, or 7.0×10^5, respectively, for the control group, gelatin medium only, or gelatin + MMT, showing a clear increase in cell adhesion with MMT.

Ramana *et al.*[148] formed MoS_2 aggregates, a spherical cotton candy-shaped material composed of MoS_2 coated with albumin to diagnose and eradicate cancer cells using PTT and PDT. HeLa cell viability was only 10% after incubation with MoS_2 (200 μg mL^{-1}), followed by NIR laser irradiation (808 nm, 500 mW) for 5 minutes. Li *et al.*[62] developed a technique for building a nanostructure self-assembled layer-by-layer by DNA non-complementary oligonucleotides with thiol-terminated groups that bind to sulfur atom defect vacancies on MoS_2. This superstructure was used as a drug delivery vehicle to improve targeted chemotherapy for cancer cells by increasing targetability, drug release, and encapsulation efficiency. The human breast cancer cells MDA-MB-468 were tested with DOX (5 μM) and different components, including the superstructure (LBL-DOX/D2/MoS_2-NS). Results revealed higher cell death caused by the superstructure (80% of apoptosis) and a tumor spheroids volume reduction of 45% after 5 days. Ji *et al.*[147] produced DNA/MoS_2-NS, a nanostructure constituted by MoS_2 nanosheets and glycoligands – Galactose (Gal), *N*-acetylgalactosamine (GalNAc), and lactose. These nanostructures were responsible for recognizing and afterward inducing increased ROS formation in tumor cells. *In vitro* tests showed that a nanocomposite concentration of 10 μg mL^{-1} decreased human hepatoma Hep-G2 cell viability by 83%. Vadivelmurugan *et al.*[149] used a spherical homogenous core built by the self-assembly of cystamine-glutathione-MoS_2 (CYS-GSH-MoS_2) with pluronic F127 (PF127) and encapsulated DOX. HeLa cell lines were incubated with the nanomaterial for

Table 2 Self-assembled inorganic nanoparticles biological effects tested in *in vitro* studies

			Biological studies *in vitro*		
Material	Further functionalization	Application	Parameters	Results	Ref.
AuNPs	EGF, DOX	Drug delivery and targeting	U87, GBM43 and U251 cells Incubation: 72 h	DOX-EGF-SA-AuNPs IC_{50}: U87 cells = 98.2 nM GBM43 cells = 36.76 nM U251 cells = 45.57 nM	138
Au-Fe_3O_4 NPs	PEG and PS	Imaging	U87MG cells Incubation: 24 h [Au@PS-Fe_3O_4@PEG] = 0.4, 0.8, 1.6, 3.2 nM	For all concentrations Cell viability: 100%	59
AuRNs-CpG-DOX	PEG-TH, TLR agonist, TLR9 specific CpG and ODNs	Chemotherapy, hyperthermia, and immunotherapy	H22 cells I: 808 nm 1.5 W cm^{-2}, 10 min Incubation: 4 h	T_{max} = 42 °C AuRNs-CpG-Dox: [50 pM] = 70% [100 pM] = 45% [250 pM] = 10%	139
BP QDs@PPS	HDACis	PTT and chemotherapy for eradicating primary cancer before metastasis	B16F10 cells I: 808 nm, 1 min, 1 W cm^{-2} Incubation: 4 h	IC_{50}: PPS = 1.41 μg mL^{-1}, free BPQDs = 1.24 μg mL^{-1} BPQDs@PPS = 0.25 μg mL^{-1} Cell viability: BPQDs@PPS (2.5 μg mL^{-1}) = 10% BPQDS@PSS induces apoptosis at 0.2 μg mL^{-1} HSP70 protein expression increases with BPQDS@PSS concentration	140
CCM@AT	Cancer cell membrane	Chemo-photo therapy	4T1 tumor cells I: 808 nm, 0.5, 1.0, 1.5 W cm^{-2}, 10 min Incubation: 4 h	Maximum fluorescence at [H_2O_2] = 75 μM Photothermal efficiency = 21.4% T_{max} = 45 °C Cell viability = 10.95% to CCM@AT (at Ag_2S QDs 0.21 mg mL^{-1}, TeNRs 0.032 mg mL^{-1}) + laser	141
CDDP : GO	Cisplatin (cddp), nanosheets, proflavine and DOX	Targeted chemotherapy	HeLa cervical cancer cells, L929 fibroblasts Incubation: 24 h	GO–CDDP-NPs: IC_{50} = 7.5 μM	60
DEA-f-Gr-*f*-ODA	CPT	Drug delivery	A549 cells Incubation: 24, 48 h	IC_{50}: 24 h = 12.5 μM 48 h = 1.5 μM Cell viability (9.12 μg mL^{-1}) = 20% CPT release (176 h) = 38% Cell Uptake (4.56 μg mL^{-1}): 24 h = 23.5%, 48 h = 43.9%	142
DNA/MoS_2-NS	DOX	Delivery of cancer chemotherapy	MDA-MB-468 cells Incubation: 48 h [DOX] = 5 μM	Apoptosis after 48 h: Control = 17% Dox = 17% LbL-Dox/D2/MoS_2-NS = 80%	62
ELK1-GO	N/A	Functional fluidic devices and organ-on-a-chip-platform	hUVEC cells Incubation: 7 days Cell culture occurred at the same time of self-assembly	ELK1–GO membrane: formation of an integral endothelial layer on both sides After 7 days the number of cells doubled	6
F-apt/SWNT	N/A	Cancer detection and imaging	CCRF.CEM cells to Ramos cells ratios: 3 : 1, 1 : 3	3 : 1 ratio: positive signs = 73.37% 1 : 3 ratio: positive signs = 25.59% Maximum sensitivity: 12 CCRF-CEM cells in samples with 100 000 non-target cells	143
Fe2O3@GO MitP-TF	TF, MitP	Photothermal therapy of cancer	Sarcoma bearing mice, [L-/S-Fe_2O_3@GO-MitP-TF] = 50 mg kg^{-1} (per day), I: 808 nm, 20 W cm^{-2}, 10 min, for 6 days	T_{max} = 60 °C Apoptosis = 78% Decreased tumor weight by 90%	66
GO-HDex	DOX	Drug delivery	MCF-7/ADR cells [DOX] = 2 μg mL^{-1} Incubation: 24 h	Cell death = 70%	43

Table 2 *(Contd.)*

			Biological studies *in vitro*		
Material	Further functionalization	Application	Parameters	Results	Ref.
GQDs-Mn_3O_4w/RhB dye	RhB	Improvement of surface-enhanced Raman scattering for cancer cell identification and to detect small molecules	HL7702, HepG-2, HeLa cells [GQD]-[Mn_3O_4] = 0–800 μg mL^{-1} Excitation at 514 nm	Cell viabilities > 90% SERS peak: HeLa and HepG-2 = 2935 cm^{-1} HL7702 cells = 3087 cm^{-1}	64
Graphene nanoplatelets	N/A	Lung cancer sensor array	ANXA2, VEGH, ENO1 incubation over night Tested in DC mode	Detection limits: ANXA2 and VEGF = 1.0 pg mL^{-1}, ENO1 = 0.1 pg mL^{-1}	63
HAP/CS/HA/MXene/AuNRs/DOX	DOX and AuNRs	Drug delivery	MCF-7 cells Incubation: 24 h	Cell viability (100 μg mL^{-1}): HAP/CS/HA/MXene/AuNRs = 85% HAP/CS/HA/MXene/AuNRs/DOX = 43.55%	46
Hap@PDA/AuNR	AuNRs and DOX	Multi-responsive drug delivery vessels for cancer therapy	MCF-7 cells Incubation: 24 h, pH = 4.5 I: 808 nm, 4 W cm^{-2}, 12 h	DOX release: HAP/PDA/AuRNs = 14.8% HAP/PDA/AuRNs + NIR = 40% Cell viability: HAP/PDA/AuRNs/DOX (50 μg mL^{-1}) = 73.5%	145
Janus BP QDs/metal-organic nanoparticles	N/A	Photodynamic therapy	HepG2 cells Incubation: 3 h I: 670 nm, 0.1 W cm^{-2}, 5 min	Cell viability: Laser + BPQDs (80 μg mL^{-1}) = 56.1% Laser + J-MOPs (80 μg mL^{-1}) = 22%	65
MMT	N/A	Induce angiogenesis	1×10^5 HeCaT cells Incubation: 24 h	Cell viability: tissue culture medium = 72% Gelatin medium = 79% Gelatin + magnetic micro-tubular medium = 88% Adhered cells: control = 2.8×10^5 Gelatin medium = 4.1×10^5 Gelatin + magnetic micro-tubular medium = 7.0×10^5	67
MnO_2@PtCo nanoflowers	N/A	Anticancer chemodynamic therapy	4T1 tumor cells Incubation: 48 h Cytotoxicity was tested in normoxia and hypoxia	Cell viability (200 μg mL^{-1}): Normoxia = 5% Hypoxia = 10% Induced hypoxia inducible factor (HIF)-1a expression	146
MoS2 (2D)	N/A	Anticancer photodynamic therapy	HeLa Broadband light source: 30 min Incubation: 2 h	Cell viability: 2D MoS_2 + light 5 μg mL^{-1} = 72% 10 μg mL^{-1} = 64%	147
MoS2 aggregates and sheets	N/A	Cancer diagnosis, photothermal, and photodynamic therapy	HeLa cells I: near infrared, 10 min, 200 μg mL^{-1}	Cell viability = 10%	148
MoS_2-GSH-CYS-PF127	DOX	Bio-responsive drug delivery for cancer treatment	HeLa cell lines Incubation: 24 h	Cell viability (40 μg mL^{-1}) = 35% Red fluorescence in the cells after 6 h for: free DOX, DOX loaded MoS_2-GSH-CYS-PF127 (5 μg mL^{-1})	149
MXene/C3N4	TPP and PEG-NH_2	Photothermal, and photodynamic therapy of cancer	A549 and MCF-7 cells Incubation: 4 h I: 808 laser (0.8 W cm^{-2}, 5 min) or 670 nm (0.48 W cm^{-2}, 5 min)	T_{max} = 59 °C Cell viability: PBS = 100% Ti_3C_2/g-C_3N_4-TPP = 100%, Ti_3C_2/g-C_3N_4 + 670 nm = 55%, Ti_3C_2/g-C_3N_4 + 808 nm = 50%, Ti_3C_2/g-C_3N_4 + 670&808 nm = 27%, Ti_3C_2/g-C_3N_4-TPP + 670 & 808 nm = 13%	150
N^+/Graphene	N/A	Tissue regeneration	Mouse-fibroblast cells (L929) and human endothelial cells (E926) Graphene + three different concentrations N^+, (1×10^{16}, 1×10^{18},1×10^{20}) ions cm^{-2}, MTT colorimetric assay after 7 days	Contact angle: 3D-graphene = 56.58°, N^+/3D-graphene = 27.52°, MTT Optical density (day 7): 3D-graphene = 0.7, N^+/3D-graphene at 1×10^{20} ions per cm^2 = 1.2	151
nGO@DOX-cPEG	PEG	NIR induced chemothermal therapy	Prostate cancer cells (PC3, DU145 and LNCaP) Incubation 24 h I: NIR, 2.0 W cm^{-2}, 5 min	T_{max} = 50 °C Cell viability: GO@DOX-cPEG = 25% GO@DOX-cPEG + NIR = 10%	152

Table 2 *(Contd.)*

			Biological studies *in vitro*		
Material	Further functionalization	Application	Parameters	Results	Ref.
nHA-rGO	N/A	Eradication of bone cancer cells using PTT and induction of new bone tissue formation	MG-63 cells I: 808 nm, 1 W cm^{-2}, 10 min, for 5 days	T_{max} = 77 °C Cell viability = 15%	153
PNIPAM-peptide-Au	DOX	Drug delivery and fluorescence imaging	HeLa cells	Cell viability (2.5 mM) = 110% Bright red emission is mainly co-localized in the lysosomes	154
RuZ, cyclometalated Ru(II)	N/A	Drug delivery	MDA-MB-231/Adr cancer cells Incubation: 2 h, 10 μM	2.5 μM RuZ reduced ATP production to almost zero Cell viability = 55%	155
TC@Ch-MFO	CS	Chemodynamic therapy, and magnetic resonance imaging	HeLa cells I: 808 nm, 1.5 W cm^{-2}, 10 min Incubation: 4 h	Cell viability = 20%	156
Ti_3C_2@GNRs/PDA/Ti_3C_2	DOX, PDA and CH_3	Drug delivery to be applied in remote cancer therapy	MCF-7 cells I: 808 nm, 2 W cm^{-2}, 1 h Incubation: 4 h	pH = 4.5 (after 12 days): Cumulative release (0 W cm^{-2}) = 22.5% Cumulative release (2 W cm^{-2}) = 35.0% Cumulative release (4 W cm^{-2}) = 45.0% NIR (after 12 days): Cumulative release (pH = 4.5) = 35% Cumulative release (pH = 6.5) = 10% Cumulative release (pH = 4.5) = 2% Cell viability: Ti_3C_2@GNRs/PDA/Ti_3C_2 (50 μg mL^{-1}) = 90% Ti_3C_2@GNRs/PDA/Ti_3C_2 + DOX (50 μg mL^{-1}) = 54.2%	157
V_2O_5@pDA@MnO_2	Dopamine	Mimic intracellular antioxidant defence system	HEK293T cells Incubation: 24 h	Cell viability (40 μg mL^{-1}) = 80% Removal of superoxides (15 μg mL^{-1}) = 70%	158

4T1: murine carcinoma cells; 5-FU: 5-fluorouracil; AIBI: 2,2-azobis[2-(2-imidazolin-2-yl)propane] dihydrochlorine; AuNRs: gold nanorods; AuNS: gold nanostars; BMD: bone mineral density; BMD: bone mineral density; BPQD: black phosphorus quantum dots; CDDP: cisplatin; CF: carbon fiber; CpG: unmethylated cytosine-guanosine; CPT: anticancer drug camptothecin; CPT: hydrofobic camptotheein; CS: chitosan; Cy5.5: cyanine5.5; CYS: cystine; DEA: diethanolamine; DODAB/DOPE: dimethyldioctadecylammonium bromide/1,2-dioleoyl-*sn*-glycero-3-phosphoethanolamine; DOX: Doxorubin; EGCG: Epigallocatechin-3-gallate; EGF: Epidermal growth factor; ELRs: elastin-like recombiners; F-apt: fluorophore-labeled aptamer; GO: Graphene oxide; GQDs: graphene quantum dots; Gr: graphene; ODA: oleylamine; GSH: glutathione; H22: mouse hepatocellular carcinoma cell line; HA: hyaluronic acid; HDACis: histone deacetylase acetylase inhibitor; HDex: hematin-terminated dextran; HEK293T: human embryonic kidney cells; HLECs: human lymphatic endothelial cells; I: laser irradiation; IC_{50}: half maximal inhibitory concentration; ICG: indocyanine green; Krasl: mutant anticancer KRASl: mutant anticancer K-Ras gene plasmid; LBL: layer-by-layer; MAPM: magnetically active polymeric micelle; MCF-7: human breast cancer cells; MitP: mitochondrion-targeting peptide; MMT; magnetic micro-tubular; MNP: magnetic nanoparticles; MOPs: metal organic particles; N/A: not applicable; NAC: *N*-acetylcysteine; nHA: hydroxyapatite; NIR: near infrared radiation; ODNs: oligodeoxynucleotides; PBS: phosphate buffered saline; PC-3: human prostate cancer cells; pDA: polydopamine; PDT: photodynamic therapy; PE-PCL: pentaerythritol poly(ε-caprolactone); PEG: polyethylene glycol; PEI: polyethylene imine; PNIPAM: poly(*N*-isopropyl acrylamide); PS: polystyrene; PTT: photothermal thrapy; PU: elastic polyurethane; PVA: polyvinyl alcohol; QD: quantum dots; rGO: partially reduced graphene oxide; RhB: Rhodamine B; ROS: reactive oxygen species; RuZ: cycloruthenated complex; SA: self-assembled; SAHA: suberoylanilide hydroxamic acid; SWNT: single walled carbon nanotube; T80: Tween 80; TeNRs: tellurium nanorods; TF: transferrin (tumor targeting protein); THQ: tetrahydroxyanthraquinone; TLR: toll-like receptors; TPP: triphenyl phosphonium bromide.

24 h at various concentrations. For the highest concentration (40 μg mL^{-1}), cell viability decreased to 35%. Wang *et al.*[146] developed a nanostructure capable of producing chemodynamic therapy to kill cancer cells. After the murine 4T1 triple-negative breast cancer cells were incubated for 48 h with MnO_2@PtCo (200 μg mL^{-1}), 95% or 90% cell viability decreases were observed in normoxia or hypoxia, respectively. Interestingly, the nanomaterial promoted hypoxia-inducible factor (HIF)-1a expression. Huang *et al.*[158] developed a nanowire-shaped nanocomplex (V_2O_5@pDA@MnO_2) composed of V_2O_5 coated with a layer of polydopamine, which was used as an efficient link between the nanowire and the MnO_2 nanoparticles. The immortalized human embryonic kidney HEK293T cells were incubated with 40 μg mL^{-1} of the nanomaterial, and no toxicity was found, since cell viability was above 80%. For a concentration of 15 μg mL^{-1}, superoxide removal was approximately 70%.

Li *et al.*[141] self-assembled a composite nanoparticle based on AG2S and TeNRs, named CCM@AT. *In vitro* studies were made to test the efficiency of phototherapy and chemotherapy on 4T1 cells. Those were incubated with different concentrations of CCM@AT for 24 h and afterward irradiated with a NIR laser (808 nm, 1.0 W cm^{-2}) for 10 minutes. Temperature increased to 45 °C, and cell viability was lowered to 10.95%. Li

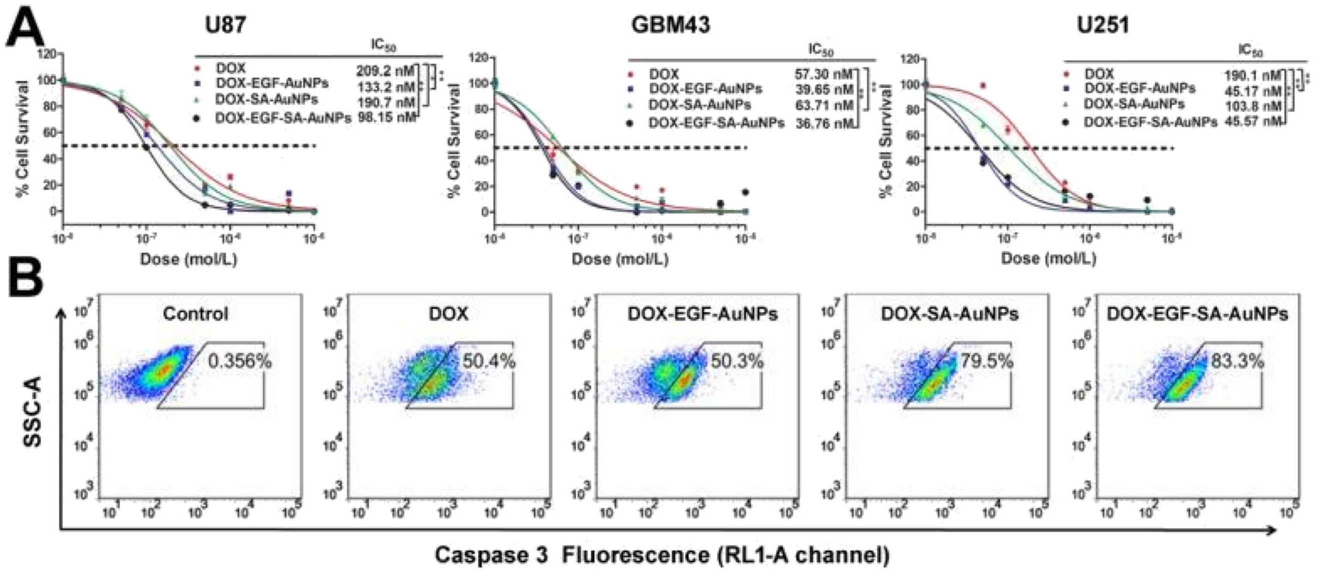

Fig. 12 Self-assembled inorganic nanomaterials *in vitro* cytotoxicity studies in brain tumor cells. (A) Cytotoxicity assays using U87, GBM43, and U251 cells treated with DOX, DOX-SA-AuNPs, DOX-EGF-AuNPs, and DOX-EGF-SA-AuNPs for 72 h. Error bars indicate standard error (n = 6). *P < 0.05, **P < 0.01, and ***P < 0.001 compared with the free-DOX group. (B) Flow cytometry analysis of cleaved caspase-3, a critical executioner of apoptosis, in U87 cells treated with 1 μM DOX, DOX-SA-AuNPs, DOX-EGF-AuNPs or DOX-EGF-SA-AuNPs for 72 h, the RL1-A channel is shown. Reproduced with permission,[138] 2017, Theranostics. AuNPs, gold nanoparticles; DOX, doxorubicin; EGF, epidermal growth factor.

et al.[155] assembled a cyclometalated Ru(II) complex by forming RuZ in water. The authors targeted the creation of a drug delivery method for the destruction of multi-drug resilient cancer cells. The human triple-negative breast cancer cells MDA-MB-231/Adr were incubated with various concentrations of RuZ. For a 10 μM concentration, cell viability was reduced to 55%.

Wu *et al.*[156] produced multimodal TMO-based nanoplatforms of Ti_3C_2 nanosheets attached to $MnFe_2O_4$. Formed nanoparticles were denominated TC@Ch-MFO and self-assembled through electrostatic mechanisms. They were designed for drug delivery, chemotherapy, to regulate the tumor microenvironment by raising the synthesis of reactive oxygen species (ROS), and for imaging applications. *In vitro* cell viability was 20% for HeLa cells treated with 300 μg mL^{-1} TC@Ch-MFO and irradiated with NIR emitted by a laser (808 nm, 1.5 W cm^{-2}) for 10 minutes.

Han *et al.*[61] developed a carbon Fiber@MXene@ZnO nanocomplex (CMZ) for cancer PTT. The photothermal heating effect was tested after coating with different amounts of PU. After 200s NIR laser irradiation (600 mW cm^{-2}), CMZ/PU-1.5, which resulted from the mixture of a CMZ solution with waterborne polyurethane to control the loading amounts of CMZ in 1.5 wt% PU, revealed the best results, being able to heat the surrounding environment until 128.7 °C, demonstrating its high photothermal conversion ability. Carbon-based nanoparticles, such as single-walled nanotubes, have been developed by Yan *et al.*[143] to provide precise and specific imaging for cancer diagnosis. The nanotubes were coated with fluorophore-labelled aptamer (F-apt) and incubated with 0 to 25 000 CCRF-CEM cells. The lowest sensitivity found was the ability to detect 12 CCRF-CEM cells mixed in a sample with approximately 100 000 non-target cells. Normal and tumorigenic cells were tested under SERS conditions with the inclusion of GQD-Mn_3O_4. The nanomaterial increased the method efficacy distinguishing cell populations.[64]

Thapa *et al.*[152] functionalized graphene oxide (GO) with DOX self-assembled by hydrothermal treatment. Subsequently, the assembled nanomaterial (nGO-@DOX) was conjugated with chitosan-polyethylene glycol (cPEG) in the liquid phase, forming nGO@DOX-cPEG, which was then tested for its capabilities as an agent for NIR-induced chemotherapy, drug delivery, and PTT. The PC3 human prostate cancer cells were incubated for 24 h with the nanomaterial and with a DOX concentration of 1 μM, followed by NIR irradiation (808 nm, 2.0 W cm^{-2}) for 5 minutes, yielding a cell viability of 25%. Wu *et al.*[6] developed an ELK1-GO composite to create a functional fluidic device and organ-on-a-chip-platform. Then, hUVECs, human embryonic vein endothelial cells, were incubated for 7 days while self-assembly occurred. Interestingly, the number of cells doubled on the ELK1-GO membrane, proving its effectiveness. Fig. 13 depicts the *in vitro* results stated above. Georgitsopoulou *et al.*[142] functionalized graphene with oleylamine (ODA) and diethanolamine (DEA) to produce Janus type nanosheets by hydrophobic self-assembly. The process formed 3D structures with hydrophilic surfaces and hydrophobic interiors. The human A549 lung cancer cells were incubated for 48 h with the nanomaterial (9.12 μg mL^{-1}). Nanoparticle uptake was 23.5% or 43.9% after 24 or 48 h, respectively, while cell viability decreased to 20%.

Cao *et al.*[151] coated graphene nanosheets with N+ to improve their biostability and biocompatibility before produ-

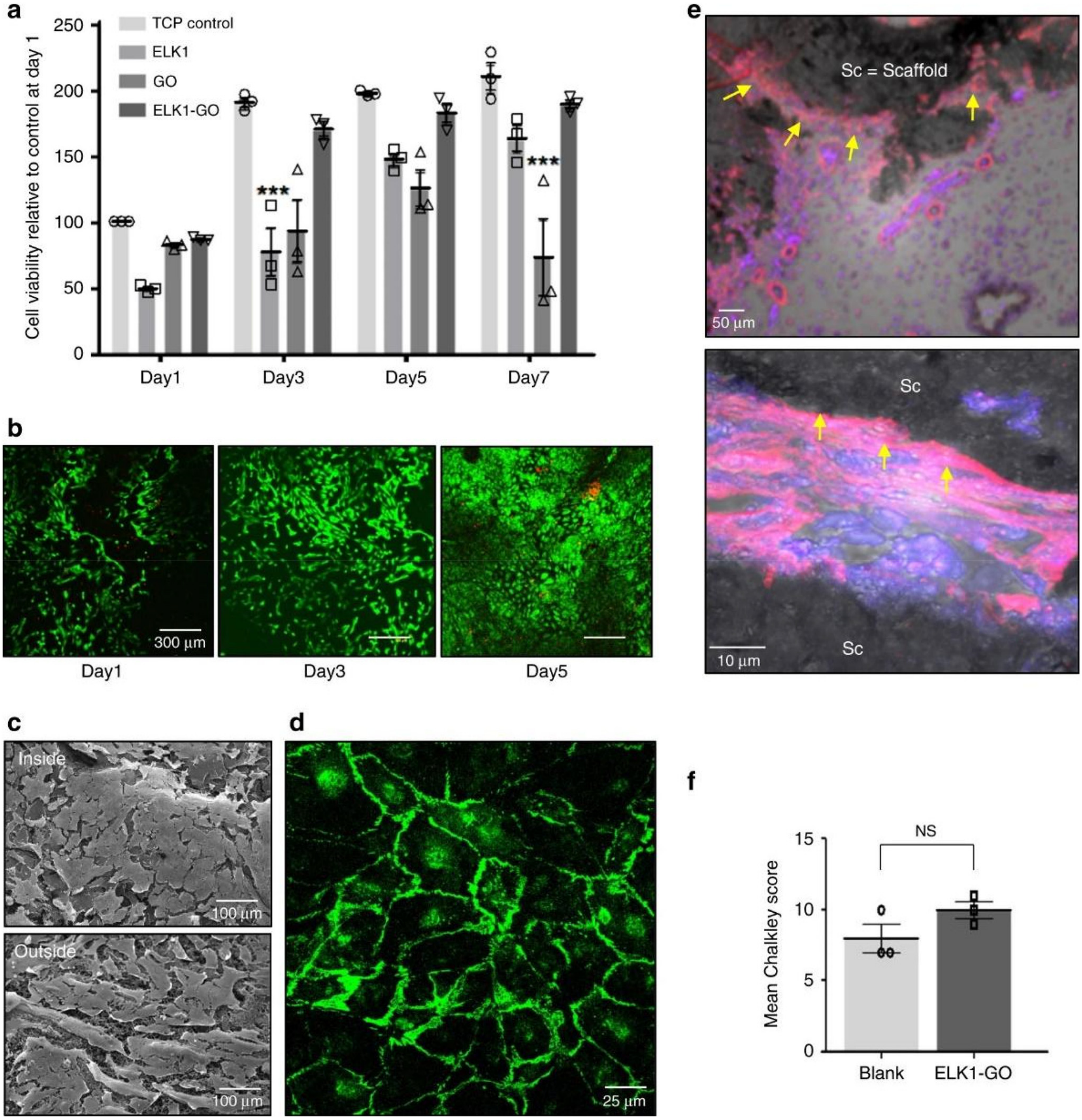

Fig. 13 Self-assembled inorganic nanomaterials for the production of capillary-like fluidic microstructures. (a) Cell viability and proliferation of hUVECS on both sides of the ELK1–GO membrane (MTT assay). ELK1 is a human transcription activator. The results revealed that cell viability and proliferation on ELK1–GO materials are at least similar to those of cells growing on tissue culture polystyrene (TCP) for 7 days. (b) Live (green)/dead (red) assay confirmed the proliferation of hUVECs. (c) Scanning electron micrographs demonstrate the formation of an integral endothelial layer on both sides of the ELK1–GO membrane. (d) VE–cadherin (CD144) was labelled to observe the organization of the adhesion molecules and revealed that cells exhibited strong intercellular junction staining, also suggesting the formation of an integral endothelial layer on the ELK1–GO membrane. (e) Histological sections of the ELK1–GO tube implants within a chick chorioallantoic membrane (CAM) model for 7 days highlighting alpha-smooth muscle actin (α-SMA, pink) staining and cell nuclei (blue) counterstain. The results revealed endothelial cells forming capillary-like structures surrounding the ELK1–GO tubes (yellow arrows). (f) Chalkley count analysis showing a slightly higher level of angiogenesis on tube-containing samples compared to control samples (blank model). Error bars represent standard deviation (n = 3). *$p < 0.05$. Two-way ANOVA. NS; no significance. Reproduced with permission,[6] 2020, Springer Nature. Abbreviations: GO, graphene oxide; hUVECs, human umbilical vascular endothelial cells.

cing tissue engineering scaffolds, succeeding in increasing cell density after N+ coating. Zhang *et al.*[63] created a lung cancer sensor array of graphene as a device to detect biomarkers present in tumor lung cells. It was able to detect the biomarkers VEGF, ENO1, and ANXA2. Detection limits were 1.0 μg mL^{-1} for ANXA2 and VEGF, and 0.1 μg mL^{-1} for ENO1. Kolokithas-Ntoukas *et al.*[144] produced alginate-coated condensed clustered colloids of magnetite nanocrystals with poly(lysine)-*b*-PEG-*block*-copolymer (MPEG-11). After the mentioned conjugation, NIR-797 isothiocyanate dye was assembled to the nanostructure, forming MPEG-NIR for imaging and PTT. The nanomaterial had a photothermal conversion efficiency of 71% when irradiated with an 808 nm laser. For healthy fibroblasts (NIH/3T3 cell line), no cytotoxicity has been detected as the obtained cell viability was superior to 90%. Fig. 14 shows that A549 cancer cell viability decreased to 50% and 27% for 50 ppm and 250 ppm of MPEG-11, respectively.

Jin *et al.*[43] created a nanocarrier based on the partial reduction and functionalization of graphene oxide (GO) conjugated with hematin-dextran (hDEX) and loaded with DOX. The cytotoxicity of GO-hDEX loaded with different DOX concentrations was tested *in vitro*. Results revealed that a nanomaterial concentration of 2 μg mL^{-1} reduced MCF-7/ADR cell viability to 30%, while DOX alone resulted in 60% viability. Li *et al.*[153] built scaffolds made of nano-hydroxyapatite (nHA) and reduced graphene oxide (rGO) for PPT and tissue regeneration. The MG-63 human osteosarcoma cells were incubated for 24 h with nHA-GO or nHA-rGO scaffolds and irradiated with a NIR laser (808 nm, 1 W cm^{-2}, 10 minutes) for 5 days. Temperature increased to 77 °C for nHA-rGO scaffolds, which led to MG-63 cell viability decreases of 85%.

Other 2D nanomaterials have been studied regarding their potential for biomedical applications, including black phosphorus and MXenes. Black phosphorus is a very promising inorganic nanomaterial that has been explored for cancer PTT and PDT, as it presents high photothermal conversion efficiency. Yu *et al.*[140] developed a nanoparticle composed of vorinostat and black phosphorus quantum dots (BPQDs@PPS). A concentration of 2.5 μg mL^{-1} of this composite incubated with the murine melanoma B16F10 cells and irradiated with a NIR laser (808 nm, 1 W cm^{-2}, 1 min) led to a cell viability of 10%. Zhang *et al.*[65] developed a spherical structure of Janus black phosphorus quantum dots (BPQDs) encapsulated in a shell of tetrahydroxyanthraquinone (THQ)-Cu coated with Cu^{2+} (MOPs). *In vitro* testing proved the high cytotoxicity of the nanocomplex towards the hepatoma-derived HepG2 cells, decreasing their viability to 22% when 80 μg mL^{-1} were used.

Wu *et al.*[46] developed a pH/NIR multi-responsive drug delivery system based on hydroxyapatite (HAP), chitosan (CS)/hyaluronic acid multilayers, gold nanorods (AuNRs), and a MXene (Ti_3C_2). Afterwards, the obtained microcapsules were emersed into a DOX solution to load the nanocomplex. The drug release profile was radiation-dependent. After 12 h at a constant pH of 4.5, the samples irradiated with 2 W cm^{-2} had a cumulative release of approximately 75%. In contrast, for the group not submitted to irradiation, the cumulative release was only approximately 45%. Similarly, the drug release was also pH-dependent. After 12 h, the drug release at pH 4.5 was 62.24% and reached 23.22% at pH 7.4. After 60 min at a laser power of 4 W cm^{-2}, the temperature increase was of 38 °C. After 24 h incubation, for a concentration of 50 μg mL^{-1}, human breast MCF-7 cancer cells viability was 60%, whilst for a concentration of 100 μg mL^{-1}, cell viability was decreased to 44%. Zhu *et al.*[157] produced a multilayer Ti_3C_2 Mxene-based nanoplatform, Ti_3C_2@GNRs/PDA/Ti_3C_2, to create a vehicle for remotely controlled and targeted drug delivery. DOX was

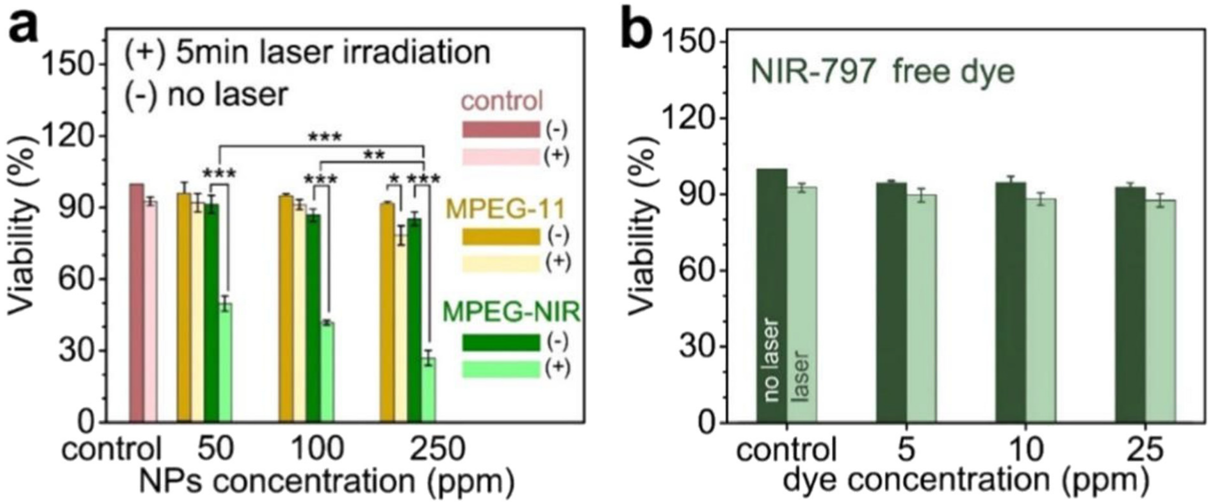

Fig. 14 Self-assembled inorganic nanomaterials for cancer photothermal therapy. Viability tests of A549 human lung carcinoma cells using the MTT assay with (+) and without (−) photothermal treatment for (a) MPEG-11 dye-labeled MPEG-NIR, and (b) free NIR-797 dye ($n = 3$, $^{*}p < 0.05$, $^{**}p < 0.01$, $^{***}p < 0.001$). Reproduced with permission.[144] 2021, American Chemical Society. Abbreviations: NIR, near-infrared; OD, optical density; SEM – scanning electron microscopy.

loaded due to its anticancer effect, and release studies were performed. PDA was also used to increase drug loading. Ti_3C_2@GNRs/PDA/Ti_3C_2 samples increased the surrounding temperature to approximately 65 °C when irradiated with a NIR laser (808 nm, 4 W cm^{-2}). Similarly to other published works, the drug release profile was pH-dependent. For a pH of 4.5, the cumulative release of DOX was approximately 45%, while at pH 7.4, the cumulative release after 12 h was approximately 20%. When MCF-7 cells were incubated with Ti_3C_2@GNRs/PDA/Ti_3C_2 loaded with DOX at a concentration of 50 μg mL^{-1} and irradiated with a NIR laser (808 nm, 4 W cm^{-2}) for 15 min, a cell survival rate of 54% was observed. Zhang *et al.*[150] developed a NIR-responsive 2D Ti_3C_2/g-C_3N_4 nanostructure coated with triphenyl phosphonium bromide (TPP): Ti_3C_2/g-C_3N_4-TPP. The aim was to construct a nanoparticle capable of performing PDT and PTT, directed at the destruction of cancer cells and surpassing hypoxia in tumor sites. Again, MCF-7 cells were incubated for 4 h and irradiated with NIR (808 laser, 0.8 W cm^{-2}) for 5 minutes. Under those conditions, temperature increased to 59 °C, and cancer cell viability decreased to 13%.

4.2 *In vivo* studies

Several *in vivo* studies have already been reported in literature involving the use of self-assembled inorganic nanomaterials. The most relevant are compiled in Table 3, which presents their potential applications, studied parameters, and most relevant results. Feng *et al.*[138] developed a nanostructure for targeted drug delivery to destroy brain tumor cells constituted by gold nanorods coated with epidermal growth factor (EGF), which resulted from the self-assembly of peptide cross-linking between the gold nanorods and dithiol-polyethylene glycol (HS-PEG-SH). The murine U87 brain tumor model was treated by intravenous injection of the nanocomposite at a DOX concentration of 1.5 mg kg^{-1}. After 27 days, this was the only group to have a survival rate of 80%, while the groups treated with free DOX, DOX-EGF-AuNPs, or DOX-SA-AuNPs all died. Song *et al.*[59] developed Janus amphiphilic nanoparticles (Au@PEG-Fe_3O_4@PS) to improve the deficiencies of traditional imaging techniques for cancer detection, which were intravenously administered to immunocompromised mice. The mice have been previously injected with human glioblastoma U87MG cells, irradiated with a 750 nm laser, and analyzed with a photoacoustic imaging laser system to evaluate their performance. These revealed a photoacoustic amplitude of 90 a.u. and a contrast efficiency of 295 m M^{-1} s^{-1}, proving to be effective for imaging applications. Tao *et al.*[139] produced a NIR-responsive gold-based nanomaterial (AuNRs-CpG-DOX) for cancer photothermal therapy. BALB/c mice injected with the H22 hepatocellular carcinoma mouse cell line were intratumorally treated with AuNRs-CpG-DOX at a DOX concentration of 1 mg kg^{-1} and a gold concentration of 1.65 nM. Then, mice were irradiated with a NIR laser (808 nm, 1.5 W cm^{-2}) for 10 min. The temperature increased to approximately 55 °C, and the final relative tumor volume was roughly 0.8.

Yu *et al.*[140] developed BPQDs@PPS for cancer PTT. Nanoparticles (1 mg kg^{-1}) were intravenously injected in mice inoculated with B16F10 melanoma cells, which were then submitted to laser irradiation (808 nm, 1 W cm^{-2}) for 90 s. BPQDs@PPS revealed no cytotoxicity or significant bioaccumulation in the kidneys, and body weight also remained similar between all mice groups. Fig. 15 shows that tumor volume was 500 mm^3 for mice treated with BPQDs@PPS followed by irradiation, while for untreated mice, it was 2500 mm^3. After 30 days, the survival rate of mice treated with BPQDs@PPS was approximately 35%, while for the other groups, it was 0%.

Li *et al.*[141] developed a composite nanoparticle based on PC_{10}AGRD-modified AG_2S and TeNRs encapsulated in 4T1 cell membranes (CCM@AT). After the CCM@AT was specifically targeted to the tumor, the TeNRs were dissolved by the high concentration of H_2O_2 at the tumor site to light up the fluorescence of Ag_2S QDs for NIR-II fluorescence imaging. In addition, the generated toxic Te_6O^6 molecules decreased ATP production by selective cancer chemotherapy, which is beneficial for photothermal therapy. The elevated temperature due to photothermal therapy promoted, in turn, the chemical reaction of chemotherapy. Compared to single photothermal therapy and chemotherapy, synergistic chemo-photothermal therapy could effectively suppress the growth of the murine 4T1 triple-negative breast cancer cells. In this study, mice were intravenously injected with the nanomaterial and irradiated with NIR (808 nm, 1 W cm^{-2}) for 10 minutes, from which no toxicity has been identified. The temperature at the tumor site reached 47 °C, and the tumor inhibition ratio of mice treated with CCM@AT and NIR was the highest, reaching 98.4%.

Yan *et al.*[143] tested the imaging and the diagnostics capability of F-apt/SWNT (200 μL D-PBS with 0.4 nmol Cy5-Sgc8 and 30 μg SWNTs) produced by non-covalent self-assembly in CCRF-CEM tumors present in nude mice. To test the imaging capabilities, the nanomaterial was injected into mice, and afterward, time-lapse fluorescence imaging was performed. As depicted in Fig. 16, mice without tumors and mice inoculated with Ramos tumor cells did not have any fluorescence for the first 90 minutes, while mice injected with CCRF-CEM had fluorescence after 30 minutes, proving the specificity of the nanocomplex.

Liu *et al.*[66] developed graphene oxide nanosheets (L-Fe_2O_3@GO-MitP-TF) functionalized with the tumor-targeting protein transferrin (TF) and the mitochondrion-targeting peptide (MitP). S180 sarcoma-burden mice were intratumorally treated with L-Fe_2O_3@GO-MitP-TF (50 mg per kg per day) and NIR laser (808 nm, 20 W cm^{-2}) for 10 min. This resulted in a temperature increase from 28 °C to 60 °C. Treatment with the nanocomposite plus NIR irradiation suppressed tumor growth. Additionally, it also led to a percentage of apoptotic cells of 78%, while the untreated mice had a percentage of 2.5%.

Kolokithas-Ntoukas *et al.*[144] produced alginate-coated condensed clustered colloids of magnetite nanocrystals with poly(lysine)-*b*-PEG-*block*-copolymer (MPEG-11). After the mentioned

Table 3 Self-assembled inorganic nanoparticles biological effects tested in *in vivo* studies

Material	Further functionalization	Application	Biological studies *in vivo* Parameters	 Results	Ref.
Au NPs	EGF, DOX, SA	Targeted drug delivery for brain cancer	U87 brain tumor-bearing Nude mice, Injected with: Cy5.5-EGF-SA-AuNPs Cy5.5-EGF-AuNPs, [Cy5.5] = 500 nmol kg^{-1} Administration route: Intravenous 5 groups: control, DOX, DOX-EGF-AuNPs, DOX-SA-AuNPs, DOX-EGF-SA-AuNPs [DOX] = 1.5 mg kg^{-1}	Fluorescence intensity: Cy5.5-EGF-SA-AuNPs ~2500 Cy5.5-EGF-AuNPs ~500 Survival rate (day 25): DOX-EGF-SA-AuNPs = 80% DOX-SA-AuNPs = 40% DOX-EGF-AuNPs = 20% DOX, and control = 0% Bioaccumulation after 24 h: liver, kidney, heart, lung, spleen, and Brain (no quantitative data was provided), AuNPs also found in urine	138
Au-Fe_3O_4 NPs	PEG, PS	Photoacoustic and MR imaging	U87MG-tumor bearing mice Administration route: Intravenous [Au-Fe_3O_4 NPs] = 500 μg mL^{-1}	Maximum photoacoustic amplitude = 90 a.u. Contrast efficiency = 295 ± 7.2 m M^{-1} s^{-1} Bioaccumulation after 24 h: liver, kidney, heart, lung, spleen, intestine, muscle and Blood (no quantitative data was provided)	59
AuRNs-CpG-DOX	PEG-TH, TLR agonist, TLR9 specific CpG, ODNs	Chemotherapy, hyperthermia, and immunotherapy	H22 tumor-bearing BALB/c mice 6 groups: PBS, Dox, CpG, AuRNs, AuRNs-CpG-Dox: 5×10^{10} particles Administration route: Intratumoral I: 808 nm, 1.5 W cm^{-2}, 10 min	T_{max} for AuNRs + NIR and AuRNs-CpG-DOX + NIR = 55 °C Relative tumor volume (after 12 days): AuRNs-CpG-Dox + NIR mice < 1 Other groups > 2, bioaccumulation after 24 h: liver, kidney, heart, lung, and spleen (no quantitative data was provided)	139
BP QDs@PPS	HDACis	PTT and chemotherapy for eradicating primary cancer before metastasis	B16F10 tumor-bearing C57BL/6 mice 4 groups: control, free BPQDs, PPS BPQDs@PPS, 1 mg kg^{-1}, administrated at 0, 2, 4, 6 and 8 days, BPQDs@PPS Administration route: Intravenous I: 808 nm, 1 W cm^{-2}, 90 s	No kidney cytotoxicity Final tumor volume (after 10 days): control = 2500 mm^3 BPQDs@PSS = 500 mm^3 Survival rate (after 25 days): BPQDs@PSS = 50% Other groups = 0% Bioaccumulation after 8 days: liver, kidney, heart, lung, and spleen (no quantitative data was provided)	140
CCM@AT	Cancer cell membrane	Chemo-photo therapy	4T1 tumor bearing mice Injection of CCM@AT (at 21 mg kg^{-1} Ag2S QDs, and 3.2 mg kg^{-1} Te) Administration route: Intravenous I: 808 nm, 1 W cm^{-2}, 10 min	Bright fluoresce in tumor 10 h post-injection Maximum temperature achieved = 47 °C CCM@AT caused 98.4% tumor inhibition after 24 days	141
F-apt/SWNT	N/A	Cancer detection and imaging	CCRF-CEM tumor-bearing Male athymic BALB/c mice Injection of 200 μL D-PBS containing Cy5-Sgc8c/SWNT (0.4 nmol Cy5-Sgc8, 30 μg SWNT) Administration route: Intravenous	Could substantially minimize the background signal originating from nontarget tissues and display contrast-enhanced imaging within the 30 min investigation	143
Fe_2O_3@GO-MitP-TF	TF, MitP	Photothermal therapy of cancer	Sarcoma bearing mice [L-/S-Fe_2O_3@GO-MitP-TF] = 50 mg kg^{-1} (per day) Administration route: Intratumoral I: 808 nm, 20 W cm^{-2}, 10 min, for 6 days	T_{max} = 60 °C Apoptosis = 78% Decreased tumor weight by 90%	66

Table 3 *(Contd.)*

Material	Further functionalization	Application	Biological studies *in vivo*		Ref.
			Parameters	Results	
MPEG-NIR	Isothiocyanate-modified NIR dye	Combine photothermal therapy and imaging	NOD Rag gamma mice injected with MPEG-NIR (150 μL, 2.5 mg mL^{-1}) Administration route: Retro-orbital	Photothermal ablation of cancer cells Deep-tissue photoacoustic and optical imaging capabilities in the ultra transparent optical window of the tissue (*ca.* 800 nm) Magnetic resonance imaging provided by the spin-active lattice of the nanocrystals Bioaccumulation after 72 h: liver, kidney, and spleen (no quantitative data was provided), clearance of nanomaterials predominantly through the hepatobiliary route	144
Janus BP QDs/metal-organic nanoparticles (J-MOPs)	N/A	Photodynamic therapy of cancer	HepG2 tumor-bearing BALB/c nude mice injected with J-MOPs (0.8 mg mL^{-1}) Administration route: Intratumoral I: 670 nm, 0.1 W cm^{-2}, 5 min	Relative tumor volume: PBS = 5.0 PBS + laser irradiation = 5.0 BPQDs + laser radiation = 4.5 J-MOPs = 3.5 J-MOPs + laser irradiation = 1.5	65
MnO_2@PtCo nanoflowers	N/A	Chemo dynamic therapy	4T1 tumor-bearing 8-week-old female Balb/c mice injected with MnO_2@PtCo nanoflowers (5 mg kg^{-1}) Administration route: Intratumoral	No cytotoxic effect Relative tumor growth: Control = 17 $MnoO_2$ = 15, PtCo = 7.5, MnO_2@PtCo = 0 Bioaccumulation after 72 h: liver, kidney, heart, lung, and spleen (no quantitative data was provided)	146
Mxene/C3N4	TPP and PEG-NH_2	Photothermal, and photodynamic therapy of cancer	MCF-7 tumor-bearing Female Balb/c nude mice I: 670 nm (0.48 W cm^{-2}, 5 min) and 808 nm (0.8 W cm^{-2}, 5 min) [Ti_3C_2/g-C_3N_4] = [Ti_3C_2/g-C_3N_4-TTP] = 20 mg kg^{-1} Administration route: Intravenous	T_{max} = 59.6 °C Relative tumor volume: PBS = 10 PBS + I = 10 Ti_3C_2/g-C_3N_4-TPP = 10 Ti_3C_2/g-C_3N_4 + I = 4.5 Ti_3C_2/g-C_3N_4 + I = 4.5 Ti_3C_2/g-C_3N_4 = 2 Ti_3C_2/g-C_3N_4-TPP + I = 0 Bioaccumulation after 24 h: liver, kidney, heart, lung, and spleen (no quantitative data was provided)	150
nGO@DOX-cPEG	PEG	Drug delivery and photochemotherapy	PC3 tumor-bearing Balb/c nude mice injected with nGO@DOX-cPEG (1 mg kg^{-1}) Administration route: Intravenous I: 808 nm, 2.0 W cm^{-2}, 5 min	T_{max} = 43.1 °C Tumor volume: Control = 1300 mm^3 DOX = 700 mm^3 nGO@DOX-cPEG = 300 mm^3 nGO@DOX-cPEG + NIR irradiation = 100 mm^3 Bioaccumulation after 24 h: liver, kidney, heart, lung, and spleen (no quantitative data was provided)	152
nHA-rGO	N/A	Cancer photothermal therapy and tissue regeneration	ICR mice and Adult male Sprague Dawley rats inoculated with MG-63 cells 4 groups: control, control + NIR, 20 wt% nHA-rGO, 20 wt% nHArGO + NIR The scaffold implantation was made at the bottom of the tumor I: 808 nm, 1.0 W cm^{-2}, 10 min Cranial defects analysed 8 weeks post-implantation	T_{max} > 60 °C nHA-rGO inhibited tumor growth (unlike the other groups) Bone mineral density: untreated defect = 96.04 mg cm^{-3}nHA-rGO = 284.58 mg cm^{-3}	153

Table 3 *(Contd.)*

Material	Further functionalization	Application	Biological studies *in vivo*: Parameters	Biological studies *in vivo*: Results	Ref.
RuZ, cyclometalated Ru(II)	N/A	Drug delivery	MDA-MB-231/Adr tumor-bearing Athymic nude female mice Administration route: Peritumoral	Relative volume after 14 days: PBS = 7.5 Dox (3.0 mg kg^{-1}) = 7 RuZ (1.5 mg kg^{-1}) = 4.4 RuZ (3.0 mg kg^{-1}) = 1.8 Bioaccumulation after 24 h: liver, kidney, heart, lung, and spleen (no quantitative data was provided)	155
TC@Ch-MFO	CS	Chemodynamic therapy, phototherapy, and magnetic resonance imaging	MIA*paca-2* tumor-bearing 5-week-old nude mice 5 groups: control, Ti_3C_2, TC@Ch-MFO and TC@Ch-MFO + NIR Administration route: Intratumoral I: 808 nm, 1 W cm^{-2}, 5 min	T_{max} = 55 °C Tumor volume: Control = 900 mm^3 TC@Ch-MFO + NIR = 200 mm^3	156
V_2O_5@pDA@MnO_2	Dopamine	Mimic intracellular antioxidant defense system, to decrease the harmful ROS production	Kunming mice inoculated with phorbol 12-myristate 13-acetate [(PMA)] = 100 μg mL^{-1} Incubation = 6 h [V_2O_5] = 80 μg mL^{-1}, MnO_2 = 80 μg mL^{-1} [V_2O_5@pDA@MnO_2] = (0, 10 and 80 μg mL^{-1}) Injection on the inflammation site	Mice treated with PMA showed strong luminescence The group treated with V_2O_5@pDA@MnO_2, and PMA showed a decrease in luminescence	158

4T1: murine carcinoma cells; 5-FU: 5-fluorouracil; AIBI: 2,2-azobis[2-(2-imidazolin-2-yl)propane] dihydrochlorine; AuNRs: gold nanorods; AuNS: gold nanostars; BMD: bone mineral density; BMD: bone mineral density; BPQD: black phosphorus quantum dots; CDDP: cisplatin; CF: carbon fiber; CpG: unmethylated cytosine-guanosine; CPT: anticancer drug camptothecin; CPT: hydrofobic camptotheein; CS: chitosan; Cy5.5: cyanine5.5; CYS: cystine; DEA: diethanolamine; DODAB/DOPE: dimethyldioctadecylammonium bromide/1,2-dioleoyl-*sn*-glycero-3-phosphoethanolamine; DOX: doxorubin; EGCG: -Epigallocatechin-3-gallate; EGF: Epidermal growth factor; ELRs: elastin-like recombiners; F-apt: fluorophore-labeled aptamer; GO: graphene oxide; GQDs: graphene quantum dots; Gr: graphene; ODA: oleylamine; GSH: glutathione; H22: mouse hepatocellular carcinoma cell line; HA: hyaluronic acid; HDACis: histone deacetylase acetylase inhibitor; HDex: hematin-terminated dextran; HEK293T: human embryonic kidney cells; HLECs: human lymphatic endothelial cells; I: laser irradiation; IC_{50}: half maximal inhibitory concentration; ICG: indocyanine green; KRASl: mutant anticancer K-Ras gene plasmid; LBL: layer-by-layer; MAPM: magnetically active polymeric micelle; MCF-7: human breast cancer cells; MitP: mitochondrion-targeting peptide; MMT: magnetic micro-tubular; MNP: magnetic nanoparticles; MOPs: metal organic particles; N/A: not applicable; NAC: *N*-acetylcysteine; nHA: hydroxyapatite; NIR: near infrared radiation; ODNs: oligodeoxynucleotides; PBS: phosphate buffered saline; PC-3: human prostate cancer cells; pDA: polydopamine; PDT: photodynamic therapy; PE-PCL: pentaerythritol poly(ε-caprolactone); PEG: polyethylene glycol; PEI: polyethylene imine; PNIPAM: poly(*N*-isopropyl acrylamide); PS: polystyrene; PTT: photothermal thrapy; PU: elastic polyurethane; PVA: polyvinyl alcohol; QD: quantum dots; rGO: partially reduced graphene oxide; RhB: Rhodamine B; ROS: reactive oxygen species; RuZ: cycloruthenated complex; SA: self-assembled; SAHA: suberoylanilide hydroxamic acid; SWNT: single walled carbon nanotube; T80: Tween 80; TeNRs: tellurium nanorods; TF: transferrin (tumor targeting protein); THQ: tetrahydroxyanthraquinone; TLR: toll-like receptors; TPP: triphenyl phosphonium bromide.

conjugation, the NIR-797 isothiocyanate dye was assembled in the nanostructure, forming MPEG-NIR for aimed imaging and PTT applications. Different preclinical imaging tools were combined, namely MR, optical, and ultrasound-photoacoustic (US-PA). Mice were retro-orbitally injected with the nanomaterial at a concentration of 2.5 mg mL^{-1}. The optical imaging provided strong fluorescence signals in the intestine and liver at 4 h and 8 h, respectively. In the liver then it gradually decreased until the last measurement at 72 h. The MR imaging confirmed the washout of the nanoparticles from the liver and the presence of the nanocomplexes in the spleen. Finally, US-PA imaging at 800 nm showed significant uptake into the spleen with a maximum PA intensity registered 8 h after the injection, while regarding the fluorescence registered in the liver, it should be noted that the maximum value was registered 24 h after the injection. After achieving the mentioned peak, fluorescence was slightly reduced until 72 h (the last period recorded). This test demonstrated the optical capabilities of the nanostructures in deep tissues when combined with imaging tools.

Zhang *et al.*[65] developed a spherical structure (J-MOPs) composed of Janus black quantum dots (BPQDs) encapsulated in a shell of tetrahydroxyanthraquinone (THQ)-Cu coated with Cu^{2+}. After the mice injected with the HepG2 tumor cells formed a tumor with the desired volume, the researchers intratumorally injected the J-MOPs (0.8 mg mL^{-1}), followed by laser irradiation (670 nm, 0.1 W cm^{-2}) for 5 min. After 14 days, the tumor volume was 5-fold lower than that of the control group, showing J-MOPs effectiveness for PDT.

Wang *et al.* produced[146] biomimetic MnO_2PtCo nanoflowers that were intratumorally administered (5 mg kg^{-1}) to

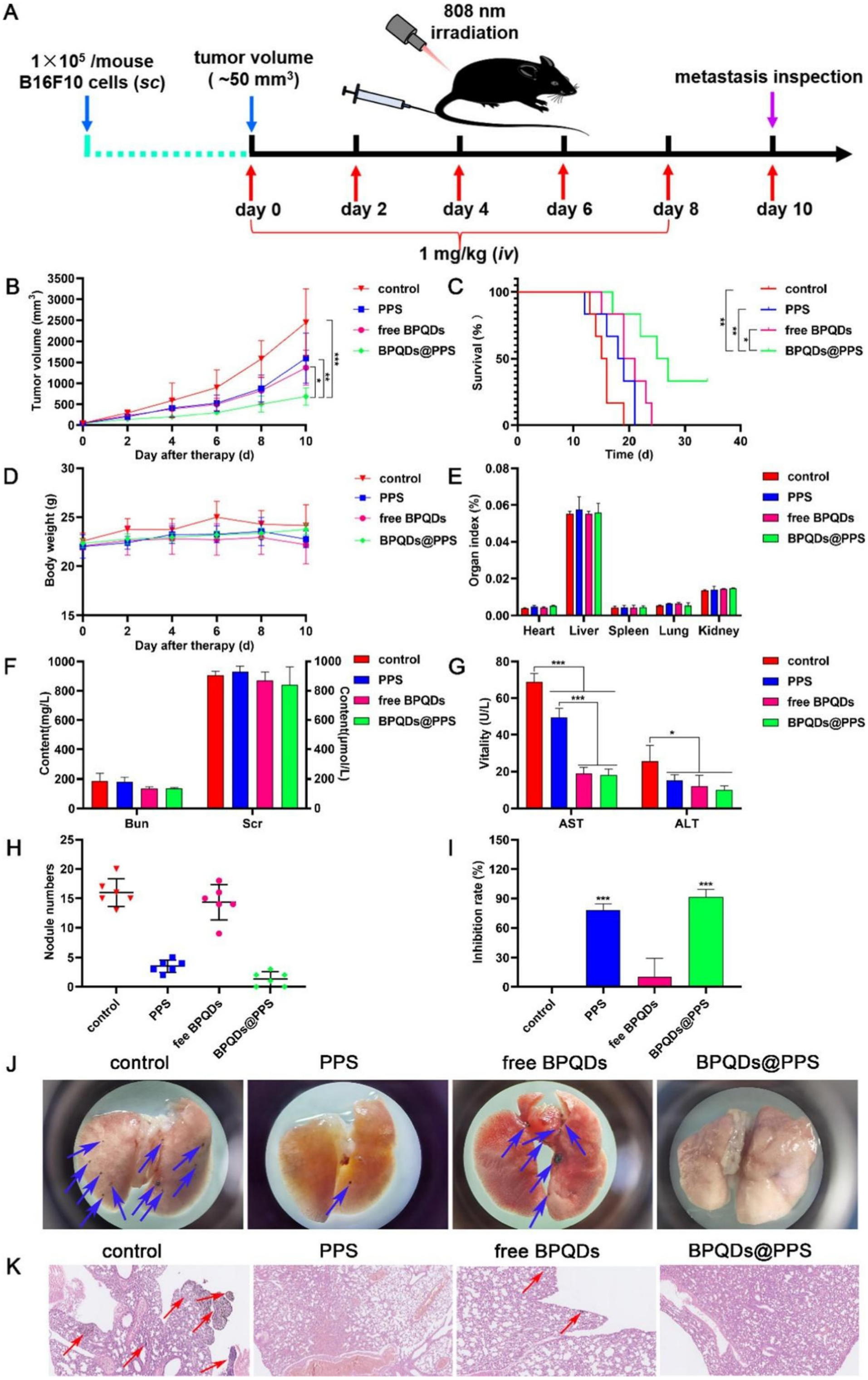

Fig. 15 Self-assembled inorganic nanomaterials for combined NIR photothermal therapy of cancer *in vivo*. BPQDs@PPS antitumor efficacy and safety have been tested on mice bearing B16-F10 melanoma cells. Animal administration protocol (A). Tumor volume (B); survival curves (C); body weight change (D); organ index (I); blood biochemical indicators of the liver (F) and kidney toxicity (G). Number of pulmonary metastasis nodules (H) and inhibition rate (I). The photographs of lung tissues with metastatic nodules of the first dead mice in each group (J); microscopic images obtained by H&E staining of the lung sections from the first dead mice in each group (×40) (K). The data were presented as mean ± SD ($n = 6$), $*p < 0.05$, $**p < 0.01$, $***p < 0.001$. Reproduced with permission.[140] 2022, Elsevier B.V.

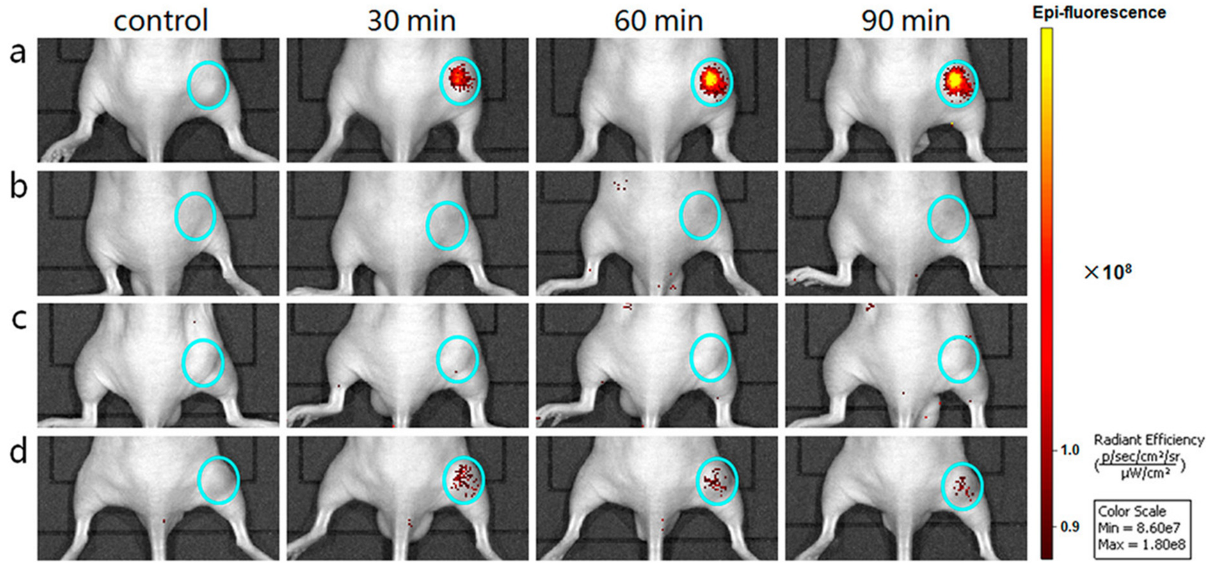

Fig. 16 Self-assembled inorganic probes for time-lapse fluorescence imaging of live mice grafted with different tumors. (a) CCRF-CEM tumor-bearing mice were injected with Cy5-Sgc8c/SWNT. (b) Normal mice without tumors were injected with Cy5-Sgc8c/SWNT. (c) Ramos tumor-bearing mouse injected with Cy5-Sgc8c/SWNT. (d) CCRF-CEM tumor-bearing mice injected with Cy5-Control/SWNT (Cyan circles indicate the injection sites; the control image was taken before injection). Reproduced with permission[143] 2014, American Chemical Society. Abbreviations: F-apt, fluorophore-labeled Aptamer; SWNT, single-walled carbon nanotubes.

BALB/c mice injected with 4T1 tumor cells. Interestingly, the tumor growth after treatment was 0, while the control group had a relative tumor growth of 17 times the initial size. No toxicity was observed towards healthy cells. MnO_2@PtCo nanoflowers not only could relieve hypoxic conditions but also induced cell apoptosis significantly through a ROS-mediated mechanism, thereby resulting in a remarkable and specific inhibition of tumor growth.

Zhang *et al.*[150] developed a heterogeneous 2D nanosheet composed of Ti_3C_2/g-C_3N_4, coated with triphenyl phosphonium bromide (TPP), and $PEG\text{-}NH_2$, forming Ti_3C_2/g-C_3N_4-TPP. The goal was to obtain a nanoparticle capable of simultaneously performing PDT and PTT, destroying cancer cells, and surpassing hypoxia at tumor sites. Mice bearing MCF-7 cancer cells were intravenously injected with the nanocomposite (100 μg mL^{-1}), followed by 670 nm (0.48 W cm^{-2}, 5 min) or 808 nm (0.8 W cm^{-2}, 5 min) laser irradiation. Groups of mice treated with only one laser and Ti_3C_2/g-C_3N_4 showed a very low inhibition rate, with no differences being found between the lasers. However, further investigation revealed that the coated nanocomplex induced complete tumor growth inhibition when irradiated with both lasers. Mice treated with both lasers and with the uncoated version of the nanomaterial still showed a relative tumor volume of 2.5. Despite the registered increase, it is still possible to conclude that a strong inhibition effect was present since the control group showed a relative tumor volume of approximately 9 times the initial size.

Thapa *et al.*[152] functionalized graphene oxide (GO) with doxorubicin, followed by modification with chitosan-PEG, to form nGO@DOX-cPEG. The nanomaterial was tested for its capabilities as an agent for NIR-induced chemotherapy. It has been administered intravenously to a PC3 xenograft mouse model, followed by NIR laser irradiation (808 nm, 2.0 W cm^{-2}) for 5 minutes. This treatment resulted in a local temperature increase to 43.1 °C. Mice treated with nGO@DOX-cPEG + NIR showed a decrease in tumor volume to almost half of the initial size after 20 days. Furthermore, to study the biodistribution, researchers used Cy5.5, a fluorescent probe, and nGO@Cy5.5-cPEG, as shown in Fig. 17. Cy5.5 present in the nanocomplex had longer circulation than free Cy5.5. Mice treated with free Cy5.5 showed no significant difference between the accumulation rates in tumor sites or in other organs, while Cy5.5 transported by the nanoparticles showed a clear tumor site-selective accumulation at 24 h after injection.

Li *et al.*[153] assembled a scaffold of nano-hydroxyapatite (nHA) and reduced graphene oxide (rGO), forming nHA-rGO to be used for bone tumor PTT and to induce bone tissue regeneration. Mice were injected with MG-63 cancer cells, followed by treatment with nHA-rGO and NIR laser (808 nm, 1.0 W cm^{-2}) for 10 minutes. Temperature increased to 60 °C after 4 minutes, and tumor growth was significantly inhibited. After 8 weeks, the cranial defected area of the group treated with the hydrogel had a bone mineral density of 284.58 mg cm^{-3}, while the control group had only 96.04 mg cm^{-3}.

Li *et al.*[155] self-assembled a Ru(II) complex, seeking the creation of a drug delivery method to destroy multi-drug resistant cancer cells. Athymic mice injected with cancer cells (MDA-MB-231/Adr) were divided into four groups and treated with either PBS, 3.0 mg kg^{-1} of doxorubicin (DOX), 1.5 mg kg^{-1} of RuZ, and 3.0 mg kg^{-1} of RuZ. The nanoparticles were

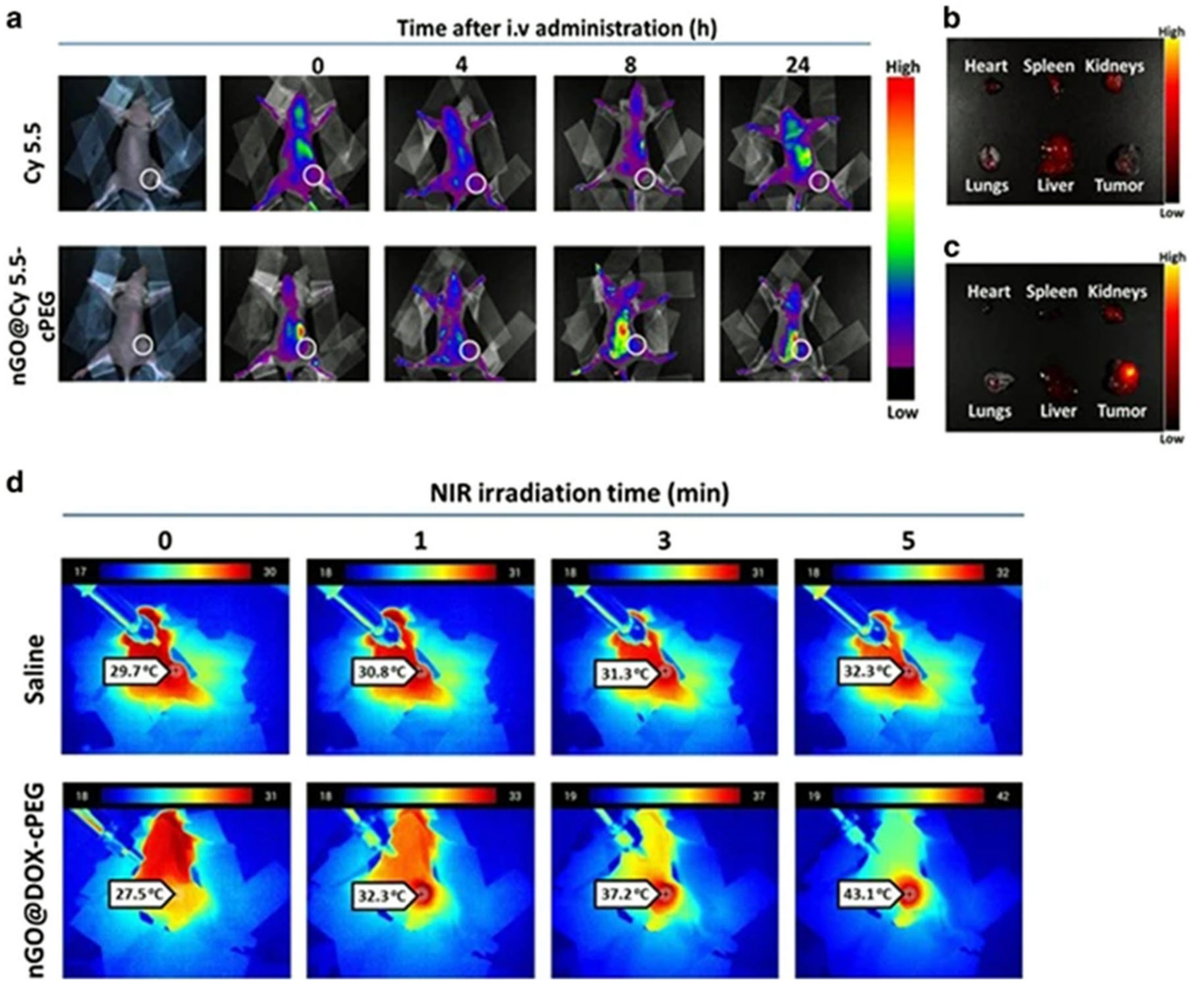

Fig. 17 Self-assembled inorganic nanomaterials *in vivo* biodistribution and photothermal effect. (a) *In vivo* biodistribution of nGO@DOX-cPEG in PC3 tumor xenograft mice (circle represents tumor area). Contours (concentration distribution) extracted from individual organs with (b) free Cy5.5, and (c) nGO@Cy5.5-cPEG are shown. (d) *In vivo* photothermal imaging upon NIR laser irradiation on tumors of mice pretreated with saline or nGO@DOX-cPEG. Reproduced with permission[152] 2017, Springer Nature. Abbreviations: cPEG, chitosan-polyethylene glycol; Cy5.5, cyanin 5.5; DOX, doxorubicin; nGO, nanodimensional graphene oxide; NIR, near-infrared.

administered in the peritumoral region. Results evidence maintenance of body weight in all groups, however, mice treated with RuZ had 62% tumor growth inhibition and a relative tumor growth of 1.8, while the control group had a relative tumor growth of 7.5. Notably, no cytotoxicity was detected for healthy cells for any of the mice groups.

Wu *et al.*[156] used multimodal TMO-based nanoplatforms (TC@Ch-MFO) of Ti_3C_2 nanosheets attached to $MnFe_2O_4$ self-assembled through electrostatic mechanisms for drug delivery, chemotherapy, and PTT. This approach aimed to combine chemodynamic therapy (CDT), PTT, and also magnetic resonance imaging (MRI). Immunocompromised mice injected with MIApaca-2 cells, derived from a human pancreatic cancer, were intratumorally administered with TC@Ch-MFO (1 mg mL^{-1}) and irradiated with a NIR laser (808 nm, 1.5 W cm^{-2}) for 5 minutes, which increased the local temperature to 55 °C. After 18 days, the researchers observed that the control group presented a tumor volume of approximately 900 mm^3, while the only group that had a tumor volume smaller than 500 mm^3 was that of mice treated with NIR plus the nanomaterial. Lastly, the nanomaterial has not been reported to cause any toxicity, and the weight of all mice studied remained constant throughout the experiment.

Huang *et al.*[158] self-assembled V_2O_5@pDA@MnO_2 nanostructures, seeking to mimic the intracellular defense system to decrease the concentration of harmful ROS and superoxide. The *in vivo* model reproduced an inflammatory model using Kunming mice and 12-myristate 13-acetate (PMA), which was used to induce acute local inflammation, increasing the concentration of endogenous ROS. The mice were treated with V_2O_5 (80 μg mL^{-1}), MnO_2 (80 μg mL^{-1}), and V_2O_5@pDA@MnO_2 nanocomposites (0, 10 and 80 μg mL^{-1}) at the inflammation site. It has been concluded that only the group treated with V_2O_5@pDA@MnO_2 showed an antioxidant effect calculated by the reduction of luminescence.

5. Biocompatibility and clinical concerns in the self-assembly of inorganic nanoparticles

Self-assembled inorganic nanoparticles are a unique tool to improve the traditional approaches or to create new therapies and biomedical applications to treat cancer and various other diseases, especially where the techniques available at the present moment failed to treat the patient or to provide acceptable outcomes. Although inorganic nanoparticles present great potential for numerous biomedical applications, these types of nanoparticles have also gathered some criticism, as they may present various toxic effects, including changes in the immunological response, which hinders future clinical trials.[163,164] The lack of clinical trials for the various nanomaterials mentioned and the small number of inorganic nanoparticles approved by the FDA for therapeutic use raised questions related to the long-term effects of these nanoparticles on the human body.[20,165]

Various aspects need to be considered before testing self-assembled inorganic nanoparticles in clinical trials. Some of the mentioned characteristics involve the prediction and evaluation of toxicity and biodegradability in the various systems of the human organism, for instance the biodistribution in the organs and impact in human metabolic pathway. At the same time, various types of toxicity must be studied, including acute toxicity, subchronic, chronic toxicity, genotoxicity, and reproductive toxicity.[20,161,166] Other challenges include the absorption of the majority of the injected nanoparticles by the reticuloendothelial system, which leads to the non-specific distribution of the nanoparticles in healthy tissues.[167] While at least one of the previously mentioned points is above an acceptable threshold, self-assembled inorganic nanoparticles must continue being improved.[20,161]

The use of satisfactory pre-clinical models, like animal models, is extremely important to correctly determine and understand the various effects of inorganic nanomaterials in the organism. Therefore, choosing the correct model will determine the validity of the *in vivo* results and reduce future risks that come with every clinical test of a new particle. The interactions between inorganic particles and the various systems depend on numerous factors like the geometrical structure, dimensions, functionalization and other hard to predict factors, since the same nanomaterial can induce different responses on different cells and prove to be inert or beneficial towards a certain tissue while being toxic to others. Interactions between systems are extremely complex and cannot be replicated precisely in *in vitro* and *in vivo* settings, because the number of variables present in a natural environment is too large, and the biological systems of laboratory animals are significantly different from those of the human body.[20,29]

To design a nanoparticle for biomedical uses, various challenges must be met and surpassed, such as the biocompatibility and safety of the systems designed, which must be considered, as illustrated in Fig. 18. As mentioned above, there is an enormous variety of inorganic building materials that can be used, adding to the possible geometrical configurations that are almost infinite. Consequently, each nanomaterial and each configuration require an extensive evaluation and characterization of their *in vitro* and *in vivo* effects.[29] The health regulators state clearly that these nanomaterials must be tested exactly in the same context as their future biomedical applications.[168]

The biocompatibility of the nanomaterials should be first evaluated by performing *in vitro* studies where the nanoparticles are incubated in a controlled space and in direct contact with the target cells. Gold nanoparticles are one of the most promising self-assembled inorganic nanomaterials, as can be concluded from *in vitro* and *in vivo* results described previously. Studies have also shown that surface functionalization is helpful in improving water stability, directly influencing cell response and cytotoxicity of those materials. Gold nanoparticles have high chemical inertness, which allows easy functionalization, and have, generally, an easy synthesis pathway.[169] Finally, different authors have shown that gold nanoparticles at various concentrations did not show any cytotoxicity for healthy cells with or without NIR laser irradiation.[138]

Carbon-based nanomaterials have attracted the attention of various researchers for numerous biomedical applications; however, their toxicity and biosafety profiles still need to be carefully studied regarding uses in PPT, PDT, bioimaging, and drug delivery.[170–172] Surface coatings composed of 3D, 2D, 1D, and 0D carbon structures have been reported in the literature.[64,151,153] The large majority of studies used coatings to improve biocompatibility and cell adherence. Cao *et al.*[151] produced an N^+ ions/3D graphene structure by hydrothermal self-assembly, which was revealed to be non-toxic to mouse fibroblast cells (L929) and to human endothelial cells (E926). Li *et al.*[153] tested 20 wt% nHA-GO and 20 wt% nHA-rGO produced by self-assembly for tissue regeneration, incubated with recombinant bone marrow mesenchymal stem cells (rBMSCs). After 5 days, materials were revealed not only to be biocompatible with normal cells but also to strongly induce cell proliferation. Lan *et al.*[64] exposed the primary human liver 7702 cells to various concentrations of graphene-quantum dots coated with Mn_3O_4 by metal ion-induced self-assembly (200, 400, 600, 800 μg mL^{-1}) for 24 h, with no cytotoxicity being found (cell viability above 95%).

Importantly, regarding metal-based nanomaterials (*e.g.*, iron oxide, MnO_2, MoS_2), size, charge, and surface geometry are factors that directly affect biocompatibility and cellular response. Ji *et al.*[147] constructed a multilayer of MoS_2

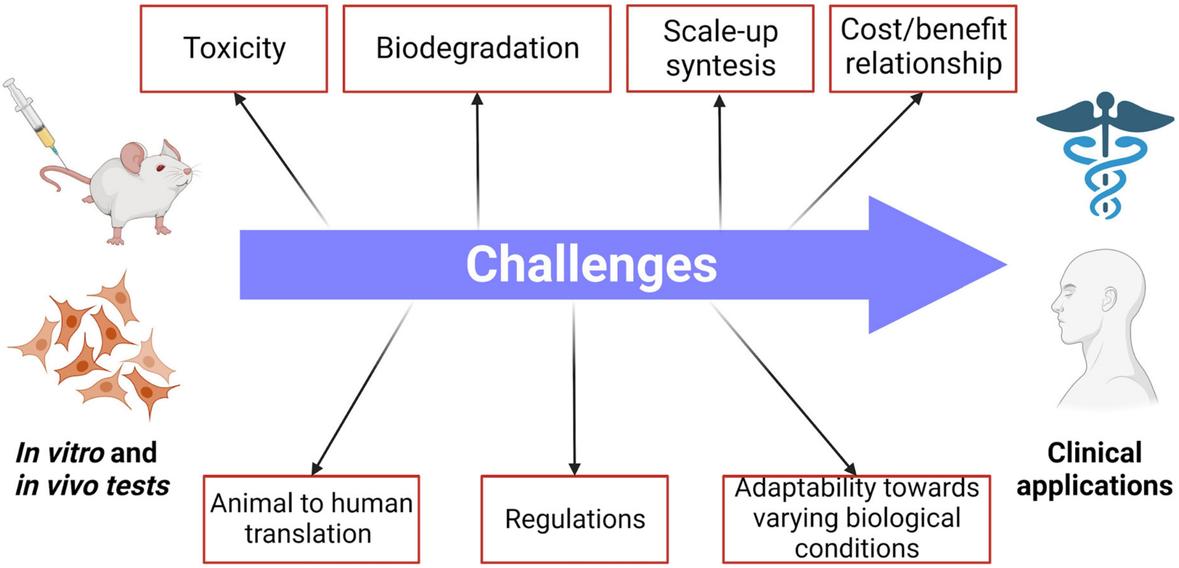

Fig. 18 Major challenges towards the clinical use of self-assembled inorganic nanoparticles. Examples are: their potential toxicity, to assure their biodegradation, that their synthesis scale-up is possible, a cost/benefit relationship to patients/hospitals, and suitable testing conditions and reproducibility regarding adaptability towards varying biological conditions, as well as animal to human translation; another important challenge is complying with applicable laws and regulations. Created with BioRender.com.

nanosheets, self-assembled by DNA chains, which increased the cohesion of the structure and made them sensible to the tumor environment. The nanoparticles were seeded with Hep-G2 and showed no toxicity towards these cells with concentrations up to 100 μg mL^{-1}. Wang *et al.*[146] constructed a MnO_2@PtCo nanoflower and performed cytotoxicity studies in healthy NIH3T3 cells, incubating them with the nanoflowers under hypoxia or normoxia. In both circumstances, the cell viability after 48 h was above 80%. Li *et al.*[155] assembled a nanoparticle based on ruthenium(II) complexes denominated RuZ. This nanocomplex presented IC_{50} values of 7.46 and 8.52 μM for LO2 and MCF10A cells, respectively.

PEG is a polymer very commonly used to improve the stability of inorganic nanoparticles in aqueous media and to increase their biocompatibility. Song *et al.*[59] performed PEGylation of Janus Au–Fe_3O_4 nanoparticles and tested the cytotoxicity of the resultant nanocomplex. U87MG cells were exposed to the nanoparticles at final concentrations of 0.4, 0.8, 1.6, or 3.2 nM for 2, 4, 8, 16, and 24 h, respectively. It was concluded that even at the highest concentration and longest incubation times, 100% cell viability was found. Zhang *et al.*[150] coated Ti_3C_2/g-C_3N_4 with PEG and exposed normal human dermal fibroblasts (NHDF) to the nanocomplexes. It was concluded that for concentrations up to 300 μg mL^{-1}, cell viability was above 90%. Tao *et al.*[139] functionalized gold nanorods (AuNRs) with PEG-SH to improve the stability and the biocompatibility of the nanocomplex, and also with CpG, to form AuNRs-CpG. The viability of the murine hepatocellular carcinoma H22 cells was measured in the presence of AuNRs-CpG at various concentrations (12.5–250 pM). No apparent cellular toxicity was observed, even at the highest concentration tested (250 pM). Kolokithas-Ntoukas *et al.*[144] produced magnetic iron oxide nanoparticles functionalized with PEG (MPEG). NIH/3T3 cells were then exposed to a range of MPEG concentrations (25–500 μg mL^{-1}). Given the results of cell viability of approximately 100%, even at the highest concentration tested (500 μg mL^{-1}), the authors concluded that no cytotoxicity derived from the nanoparticles took place.

For *in vivo* testing, self-assembled inorganic nanoparticles must be stable in physiological conditions to avoid aggregation and therefore, hydrophobic nanoparticles usually require surface functionalization. Even for water stable materials, modifications are usually performed to assure biocompatibility. The nanomaterials should accomplish their mission without causing any short or long-term toxicity and ideally be eliminated from the body. Various self-assembled inorganic nanoparticles have been coated with PEG to improve the biocompatibility of the inorganic core while maintaining their key properties intact for effective biomedical use, especially when applied in imaging and drug delivery systems.[173] This type of modification has succeeded in avoiding accumulation in various organs, including the spleen and liver.[59,138,140,150,158] Song *et al.*[59] performed PEGylation of Janus Au–Fe_3O_4 nanoparticles and tested their *in vivo* biodistribution using a U87MG tumor xenograft mice model. The tumors were allowed to grow to 80 mm^3 before the study started. Afterwards, the nanocomplex was injected intravenously, and the results collected 24 h later show that the assembled particles had 10% tumor accumulation, whilst 40% were found in the liver. No long-term toxicity studies were presented, and there was a lack of obvious degradation and clearance pathways. Wang *et al.*[146] studied the *in vivo* effect of MnO_2@PtCo nanoflowers in a murine 4T1 triple-negative breast cancer model using female

BALB/c mice. The mice were divided into three groups intravenously injected with saline (control), MnO_2@PtCo nanoflowers (5 mg kg^{-1}, 7 days post-injection), or MnO_2@PtCo nanoflowers (5 mg kg^{-1}, 28 days post-injection). After 28 days, none of the markers used to evaluate the toxicology of the nanoflowers in the liver, kidney, and blood, displayed significant changes compared to the control group, suggesting that no toxic effect was caused by the nanoparticles. Also, no significant weight or growth alterations were registered, and the H&E staining of major organs revealed that the morphology of the heart, liver, spleen, and lung of the mice injected with the nanoflowers remained unchanged. Despite the fact that no cytotoxic effects were detected after 28 days of the injection, no degradation or clearance mechanisms were mentioned, which may suggest these nanoparticles can be permanently accumulated in those major organs which could lead to significant toxicological issues in longer tests.

Gold nanoparticles have been functionalized with various molecules to improve their biocompatibility, including EGF,[138] PS,[59] and PEG.[59,139] Tao *et al.*[139] functionalized gold nanorods (AuNRs) with PEG-SH to improve the stability and the biocompatibility of the nanocomplex and also with CpG to form AuNRs-CpG. BALB/c mice were injected with one million H22 cells, and after the tumor xenograft reached 100 mm^3, those were injected intratumorally with the conjugates (1.65 nM). The animals were analyzed for 12 days, including body weight monitoring. No statistical differences were found between the control group and the group of mice treated with the nanocomposite, suggesting biocompatibility. However, after 24 h, bioaccumulation in the major organs like the liver and heart was detected, however, no further tests were made to confirm the possible long term effects. Feng *et al.*[138] functionalized gold nanoparticles with EGF to improve the targeting towards specific brain cancer cells. To create a brain tumor model, 5×10^5 U87 cells were injected into the right striatum of male nude mice. Afterwards, mice were injected with the nanomaterial at a concentration of 500 mg kg^{-1} and sacrificed 30 days postinjection to analyze biodistribution. Fluorescence imaging and histology studies show a clear accumulation of gold nanoparticles in the glomeruli and in the kidney tubes, with their presence also being detected in urine, suggesting that the nanomaterial is dissociated and can be excreted *via* renal clearance. Furthermore, mice's body weight remained similar between all groups, suggesting good biocompatibility.

Black phosphorus quantum dots (BPQDs) based particles have been used for imaging, PTT, drug delivery, and other applications, showing no systemic toxicity.[65,140] Yu *et al.*[140] tested BPQDs-based particles *in vivo* biocompatibility using C57BL/6 melanoma-bearing mice. After the tumors reached approximately 50^5 cells, the nanomaterial was injected at regular intervals at a concentration of 1 mg kg^{-1}. After 10 days, no significant change in body weight between groups could be identified. Tests on the vital organs showed no toxicity or lasting damage, and blood biochemical indicators revealed no signs of toxicity toward the kidneys. Despite the positive results, the biodistribution of the quantum dots and possible clearance routes weren't addressed; before these nanoformulations could be used in biomedical applications, longer protocols that study the long-term effect of these nanoparticles are required. Zhang *et al.*[65] also developed a nanoparticle based on black phosphorus quantum dots. To test the biosafety of these nanomaterials, BALB/c mice were subcutaneously injected with HepG2 cells after the tumor xenograft reached the desired volume, and then 0.8 mg mL^{-1} of the nanocomplex was injected. During the 14 days of the treatment, no body weight change was registered. To analyze the possible effects of the nanomaterials on vital organs, researchers used the H&E staining to evaluate possible changes in tissue morphology 14 days after the injection. The staining of the heart, liver, spleen, lung, and kidney didn't register any significant difference in morphology or signs of damage. Despite no indication of cytotoxicity, the biodistribution of these materials in major organs wasn't quantified, which calls for further studies on the clearance mechanisms of these nanomaterials. Thapa *et al.*[152] reported that graphene oxide also presented indicators that suggest biocompatibility since, after 20 days, no significant body weight changes have been found in BALB/C mice exposed to the nanomaterial. Furthermore, some selectivity was proven since significant bioaccumulation in the tumor tissue was identified. However, some fluorescence was also present in the liver, lung, spleen, heart, and kidney, which means that after 14 days there is some biodistribution of these materials in the mentioned organs. The H&E staining of these organs shows that for the tested period, no significant morphological changes were recorded. Nevertheless, further long-term tests on the biocompatibility of these nanomaterials and the clearance mechanisms that can be used to eliminate these nanoparticles should be made. MXenes functionalized with PEG by Zhang *et al.*[150] did not show any renal or hepatic cytotoxicity and no significant inflammation or chronic toxicity after two weeks of administration (20 mg kg^{-1}) to MCF-7 bearing mice. Additionally, no major changes in body weight were observed for any mice treated with the nanocomplex. Despite no obvious inflammation or damage being detected in the H&E stained images after two weeks, bioaccumulation was reported on various major organs, including the heart, liver, spleen, lung, and kidneys, which could lead to future cytotoxicity problems.

Iron oxide and manganese dioxide were also used as building blocks, and, in both cases, the nanomaterials were used for PTT, PDT, and imaging.[66,146,156,158] Wu *et al.*[156] also assembled a $MnFe_2O_4$@Ti_3C_2-Chitosan complex and tested its *in vivo* effect using 5-week-old nude mice injected with MIApaca-2 cells into the right armpit. The nanocomplex was administered by subcutaneous injection at a concentration of 1 mg ml^{-1}. The weight measurements showed no significant fluctuations between the control groups and the mice treated with the nanomaterial. The H&E staining images showed no damage or toxicity in vital organs such as the heart, spleen, liver, and kidney. Huang *et al.*[158] tested the effect of the V_2O_5@pDA@MnO_2 nanocomposite in a Kunming mice inflammation model, which had phorbol 12-myristate 13-acetate applied to the ear. After 6 h, mice were injected with the nanocomposites, which proved to be very good at scavenging ROS without provoking any visible toxicity.

A self-assembled cyclometalated complex, RuZ (IV: 3.0 mg kg^{-1}) has been tested *in vivo* in mice xenografted with MDA-MB-231/Adr cells. The complex revealed good biocompatibility, no systematic toxicity and the animal body weight remained similar between all tested groups. The nanoparticles were mainly expelled in the feces, and Ru plasma concentration decreased to almost 0 after 10 h. After 72 h, very small amounts of Ru were found in the major organs, including the heart, liver, spleen, lung, and kidney.[155] Liu *et al.*[66] tested Fe_2O_3@GO-MitP-TF nanoparticles in hemocytosis and serum biochemistry assays. The analysis showed that the nanoparticles did not induce hemolysis or increase the concentration of alkaline phosphatase (ALP), alanine aminotransferase (ALT), and aspartate aminotransferase (AST). Despite good indicators of biocompatibility, further studies should be provided, including the staining of major organs and the quantification of the biodistribution of the nanomaterial after a significant number of days of treatment. Li *et al.*[141] evaluated the biosafety of CCM@AT nanoparticles by tracking the possible weight changes of mice during the treatment, the morphological changes of vital organs, using H&E staining, and by analyzing a significant number of molecules and biomarkers from blood samples. After 24 days, no significant difference could be detected between the mice in the control group and the mice treated with the nanomaterials. Also, after 15 days of the administration, no physiological and morphological difference was detected in the tissues from the main organs of the treated mice, indicating that for that period no systemic toxicity was caused by the particles. Also, no acute toxicity was detected, since the levels of hemoglobin, platelet, white blood cell, and red blood cells remained the same for all the groups, including the control. Kolokithas-Ntoukas *et al.*[144] analysed the biodistribution of MPEG-NIR nanoparticles until 72 h after the injection. The biodistribution of the nanomaterials was registered in three main organs, the liver, spleen and kidney. The amount of nanomaterial in each organ remained constant throughout the 72 h. However, the authors suggest that the nanoparticles were cleared only after two weeks of administration. Further studies are required to confirm the biosafety of the nanomaterial and to prove the clearance route proposed by the authors. Li *et al.*[153] developed a scaffold composed of nHA-rGO to combine PTT and bone regeneration. First to evaluate if the mice could tolerate the PTT, their body weight was measured for 15 days after the treatment. Since no significant changes in weight were registered between the control group and the group treated with the scaffold and irradiated with NIR, the authors concluded the mice could tolerate the treatment. Nevertheless, further studies should be made to assess the biodistribution and stability of the materials of the scaffold in physiological conditions. Furthermore, an H&E staining was performed revealing that the scaffold increased bone regeneration, which could be a sign of good biocompatibility. However, further studies are necessary to ensure the scaffold and their nanomaterials can be either consumed or cleared without inducing adverse reactions.

Some inorganic nanomaterials have already been approved by the FDA for general use as therapeutic tools, those include Feraheme, ultramicro SPIONs (Ferumoxytol; AMI-7228; Code-7228; Rienso; Fera-heme) developed by AMAG and approved in 2009 for iron-deficiency anemia. Various other inorganic nanomaterials have already started clinical trials and showed promising results like the aqueous suspension of Hafnium oxide NPs (about 50 nm) (NBTX-3; NBTXR-3; PEP-503) invented by Nanobiotix and currently being tested in Phase II/III clinical trials as radiosensitizers for soft tissue sarcoma (ClinicalTrials.gov Identifier: NCT02379845) and tested in Phase I/II clinical trials for head and neck, liver, prostate, pancreatic and rectal cancers treatment (ClinicalTrials.gov Identifier: NCT04484909; NCT02805894; NCT03589339; NCT02901483; NCT02465593; NCT02721056).[20]

Although encouraging results were obtained regarding their low or inexistent short-term toxicity, some challenges of self-assembled inorganic or hybrid nanomaterials must be tackled before future clinical applications. Self-assembly is a well-known and widely studied topic, it has been used to develop nanomaterials with unique properties for biomedical applications by numerous researchers. It allows the combination of different particles with different properties in single structures with unique shapes and sizes. Despite assembly mechanisms being extensively described, some challenges must be overcome before this approach can be considered for producing nanomaterials for biomedical applications, including difficulties in describing and predicting interactions, particularly between small nanoparticles. Some structures developed by self-assembly are bonded with weak interactions, the effect of different physiological environments on the structure of these nanocomplexes must be extensively studied to guarantee functionality and biocompatibility. Also, some of the described methods and nanomaterials have high costs and are difficult to scale up to the levels required by the pharmaceutical industry. To solve this issue cheaper and efficient methods and materials should be prioritized, without compromising the biocompatibility and efficiency of the nanocomplexes.

The biosafety of these nanomaterials, meaning the capability of the human body to deal with these foreign materials without causing short and long-term adverse reactions is a key issue to overcome. The size, concentration, presence of functional groups, and stability in water, and in physiological studies are essential properties that require extensive *in vivo* studies before more successful clinical trials can be achieved. Moreover, the degradability in the human body of inorganic and inorganic–organic hybrid nanomaterials should also be extensively studied, as it directly impacts biodistribution and clearance routes and is a significant factor in biosafety. Most biodegradation studies have been made in very controlled settings, usually with *in vitro* models. Nevertheless, the complexity of *in vivo* assays can render the data obtained with *in vitro* models unreliable. So, further *in vivo* data, such as biodistribution, degradation, metabolism, and toxicity of nanomaterials, are required before a significant translation from laboratory to clinical trials can occur.

6. Conclusions

Inorganic nanoparticles used for self-assembly of structures for bioapplications range from metal nanoparticles, graphene-based materials, new 2D nanomaterials (MXenes, TMDs, BP), to other carbon nanomaterials (carbon nanotubes, carbon nanofibers). The most common self-assembly methods to produce nanomaterials for biomedical approaches are hierarchical, layer-by-layer, metal-induced, and magnetic self-assembly. The developed structures range from nanoflowers to vesicles, highly ordered stacks of 2D nanosheets coated with other materials that form well-defined 3D structures, or even *in situ* magnetic self-assemblies formed on cancer cells. Although various materials being used as the main building blocks, carbon-based nanomaterials ranging from BPQDs to nGO flakes are the most common self-assembled nanomaterials. These types of nanoparticles are the most prominently studied and tested in both *in vitro* and *in vivo* assays, since they present easy production methods, good biocompatibility, and ideal chemistry for surface modification. Also, their versatility is noted due to the large range of therapeutic applications they can be used for, such as PTT, PDT, imaging, drug delivery, and tissue regeneration. Other widely reported building blocks include iron and gold, for which surface modifications are required to increase stability in physiological conditions and anticancer effects, as well as to improve their biocompatibility. PEGylation was often used to improve biocompatibility and increase water stability. While doxorubicin is commonly loaded on the self-assembled nanomaterials to increase anticancer effectiveness, PTT is the most reported biomedical application, with 808 nm NIR lasers (0.5–4 W, 3–10 min) being used in most of the cases, leading often to almost complete elimination of cancer cells or tumors.

Moreover, most studies do report significant bioaccumulation in vital organs such as the spleen and liver, detected *via* histological analysis, as well as some inflammation. The broad range of possibilities for fine-tuning the properties of these particles may offer an interesting pathway to solve this issue, such as coating with FDA approved polymers like PEG. Long-term toxicological tests and successful clinical trials are still needed to allow the use of these nanomaterials in clinics as an alternative treatment with advantages over standard existing options.

In summary, despite facing numerous challenges, self-assembly has numerous advantages that could outweigh all the mentioned problems; its precision and versatility can produce new inorganic and hybrid nanomaterials capable of combining numerous biomedical applications that could revolutionize the medical approach to a significant number of diseases and injuries. It is anticipated that a new era may now start aiming at translating these nanotechnology advances to improve patients' quality of life and survival.

Data availability

No new data were created or analyzed during this study. Data sharing is not applicable to this article.

Conflicts of interest

The authors declare that they have no known competing financial interests or personal relationships that could have appeared to influence the work reported in this paper.

Acknowledgements

This work was financially supported by ALiCE, LA/P/0045/2020 (DOI: **10.54499/LA/P/0045/2020**), and LEPABE UIDB/00511/2020 (DOI: **10.54499/UIDB/00511/2020**) and UIDP/00511/2020 (DOI: **10.54499/UIDP/00511/2020**), funded by national funds through FCT/MCTES (PIDDAC), base UIDB/04293/2020 Funding of the Institute for Research and Innovation in Health - i3S. This work was financially supported by national funds through the FCT/MCTES (PIDDAC), under the FCT project 2022.04494.PTDC – PhotoRect (DOI: **https://doi.org/10.54499/2022.04494.PTDC**). Artur Pinto thanks the Portuguese Foundation for Science and Technology (FCT) for the financial support of his work contract through the Scientific Employment Stimulus - Individual Call (CEECIND/03908/2017, DOI: **https://doi.org/10.54499/CEECIND/03908/2017/CP1399/CT0008**). We would like to acknowledge Prof. Joseph P. Patterson, and Rakia Dhaoui for their help revising the content of chapter 2 on a previous version of the work.

References

1 L. Colombeau, *et al.*, *Inorganic nanoparticles for photodynamic therapy*, in *Light-responsive nanostructured systems for applications in nanomedicine*, 2016, pp. 113–134.
2 R. L. Siegel, *et al.*, Cancer statistics, 2022, *CA-Cancer J. Clin.*, 2022, **72**(1), 7–33.
3 L. Fearfield and J. Natkunarajah, Cutaneous Side Effects of Chemotherapy and Radiotherapy, in *Rook's Textbook of Dermatology, Ninth Edition*, 2016, pp. 1–15.
4 D. Albano, *et al.*, Imaging side effects and complications of chemotherapy and radiation therapy: a pictorial review from head to toe, *Insights Imaging*, 2021, **12**(1), 76.
5 G. Mohan, *et al.*, Recent advances in radiotherapy and its associated side effects in cancer—a review, *J. Basic Appl. Zool.*, 2019, **80**(1), 14.

6 Y. Wu, *et al.*, Disordered protein-graphene oxide co-assembly and supramolecular biofabrication of functional fluidic devices, *Nat. Commun.*, 2020, **11**(1), 1182.

7 M. F. Simoes, J. S. Sousa and A. C. Pais, Skin cancer and new treatment perspectives: A review, *Cancer Lett.*, 2015, **357**(1), 8–42.

8 E. Bianchi, *et al.*, Inorganic nanomaterials in tissue engineering, *Pharmaceutics*, 2022, **14**(6), 1127.

9 M. A. Khan, *et al.*, Revisiting inorganic nanoparticles as promising therapeutic agents: A paradigm shift in oncological theranostics, *Eur. J. Pharm. Sci.*, 2021, **164**, 105892.

10 W. Paul and C. P. Sharma, Inorganic nanoparticles for targeted drug delivery, in *Biointegration of medical implant materials*, 2020, pp. 333–373.

11 Y. Ghosn, *et al.*, Inorganic nanoparticles as drug delivery systems and their potential role in the treatment of chronic myelogenous leukaemia, *Technol. Cancer Res. Treat.*, 2019, **18**, 1533033819853241.

12 D. C. Luther, *et al.*, Delivery of drugs, proteins, and nucleic acids using inorganic nanoparticles, *Adv. Drug Delivery Rev.*, 2020, **156**, 188–213.

13 F. A. Silva, *et al.*, 2D Nanomaterials and Their Drug Conjugates for Phototherapy and Magnetic Hyperthermia Therapy of Cancer and Infections, *Small*, 2023, 2306137.

14 Y. Wang, H.-M. Meng and Z. Li, Near-infrared inorganic nanomaterial-based nanosystems for photothermal therapy, *Nanoscale*, 2021, **13**(19), 8751–8772.

15 C. Núñez, S. V. Estévez and M. del Pilar Chantada, Inorganic nanoparticles in diagnosis and treatment of breast cancer, *JBIC, J. Biol. Inorg. Chem.*, 2018, **23**, 331–345.

16 R. Costa-Almeida, *et al.*, Near-infrared radiation-based mild photohyperthermia therapy of non-melanoma skin cancer with PEGylated reduced nanographene oxide, *Polymers*, 2020, **12**(8), 1840.

17 H. Zhou, *et al.*, Biodegradable inorganic nanoparticles for cancer theranostics: insights into the degradation behavior, *Bioconjugate Chem.*, 2019, **31**(2), 315–331.

18 L. Guo, *et al.*, Autophagy modulated by inorganic nanomaterials, *Theranostics*, 2020, **10**(7), 3206.

19 E. Bagheri, *et al.*, Silica based hybrid materials for drug delivery and bioimaging, *J. Controlled Release*, 2018, **277**, 57–76.

20 Q. Liu, *et al.*, Inorganic nanoparticles applied as functional therapeutics, *Adv. Funct. Mater.*, 2021, **31**(12), 2008171.

21 R. Urie, *et al.*, Inorganic nanomaterials for soft tissue repair and regeneration, *Annu. Rev. Biomed. Eng.*, 2018, **20**, 353–374.

22 M. Pirzada and Z. Altintas, Nanomaterials for healthcare biosensing applications, *Sensors*, 2019, **19**(23), 5311.

23 S. Kumar, *et al.*, Optically active nanomaterials and its biosensing applications—a review, *Biosensors*, 2023, **13**(1), 85.

24 X. Li, *et al.*, The peptide functionalized inorganic nanoparticles for cancer-related bioanalytical and biomedical applications, *Molecules*, 2021, **26**(11), 3228.

25 Z. Wang, *et al.*, Application of zero-dimensional nanomaterials in biosensing, *Front. Chem.*, 2020, **8**, 320.

26 Z. Wu, S. Yang and W. Wu, Shape control of inorganic nanoparticles from solution, *Nanoscale*, 2016, **8**(3), 1237–1259.

27 V. Harish, *et al.*, Nanoparticle and nanostructure synthesis and controlled growth methods, *Nanomaterials*, 2022, **12**(18), 3226.

28 R. Tenne, Inorganic nanotubes and fullerene-like nanoparticles, *J. Mater. Res.*, 2006, **21**(11), 2726–2743.

29 S. I. Amaral, *et al.*, Carbon nanomaterials for phototherapy of cancer and microbial infections, *Carbon*, 2022, **190**, 194–244.

30 A. A. Abdellatif, *et al.*, Biomedical applications of quantum dots: overview, challenges, and clinical potential, *Int. J. Nanomed.*, 2022, 1951–1970.

31 A. M. Wagner, *et al.*, Quantum dots in biomedical applications, *Acta Biomater.*, 2019, **94**, 44–63.

32 B. Ni, *et al.*, General synthesis of inorganic single-walled nanotubes, *Nat. Commun.*, 2015, **6**(1), 8756.

33 A. A. Ensafi, Z. Saberi and N. Kazemifard, Functionalized nanomaterial-based medical sensors for point-of-care applications: An overview, in *Functionalized Nanomaterial-Based Electrochemical Sensors*, 2022, pp. 277–308.

34 M. Derakhshi, *et al.*, Two-Dimensional Nanomaterials beyond Graphene for Biomedical Applications, *J. Funct. Biomater.*, 2022, **13**(1), 1–2.

35 T. Hu, *et al.*, Two-dimensional nanomaterials: fascinating materials in biomedical field, *Sci. Bull.*, 2019, **64**(22), 1707–1727.

36 Y. B. Pottathara, *et al.*, *Chapter 1 - Synthesis and Processing of Emerging Two-Dimensional Nanomaterials*, in *Nanomaterials Synthesis*, ed. Y. Beeran Pottathara, *et al.*, 2019, Elsevier, pp. 1–25.

37 Z. Li, *et al.*, Mechanisms of liquid-phase exfoliation for the production of graphene, *ACS Nano*, 2020, **14**(9), 10976–10985.

38 Y. Xu, *et al.*, Liquid-phase exfoliation of graphene: an overview on exfoliation media, techniques, and challenges, *Nanomaterials*, 2018, **8**(11), 942.

39 S. Mohan, *Synthesis of inorganic nanomaterials: advances and key technologies*, Elsevier Science & Technology, 2018.

40 C. Verma, *et al.*, 3D nanomaterials: The future of industrial, biological, and environmental applications, *Inorg. Chem. Commun.*, 2023, 111163.

41 L. Cao, *et al.*, Photoluminescence properties of graphene versus other carbon nanomaterials, *Acc. Chem. Res.*, 2013, **46**(1), 171–180.

42 M. Coroş, *et al.*, A brief overview on synthesis and applications of graphene and graphene-based nanomaterials, *Front. Mater. Sci.*, 2019, **13**, 23–32.

43 R. Jin, *et al.*, Self-Assembled Graphene–Dextran Nanohybrid for Killing Drug-Resistant Cancer Cells, *ACS Appl. Mater. Interfaces*, 2013, **5**(15), 7181–7189.

44 D. Chen, *et al.*, Theranostic applications of carbon nanomaterials in cancer: Focus on imaging and cargo delivery, *J. Controlled Release*, 2015, **210**, 230–245.

45 R. Thiruppathi, *et al.*, Nanoparticle functionalization and its potentials for molecular imaging, *Adv. Sci.*, 2017, **4**(3), 1600279.

46 Z. Wu, *et al.*, Chitosan/hyaluronic acid based hollow microcapsules equipped with MXene/gold nanorods for synergistically enhanced near infrared responsive drug delivery, *Int. J. Biol. Macromol.*, 2021, **183**, 870–879.

47 G. Gonzalez-Avila, *et al.*, Nanotechnology and matrix metalloproteinases in cancer diagnosis and treatment, *Front. Mol. Biosci.*, 2022, **9**, 918789.

48 Q. Zou, *et al.*, Biological Photothermal Nanodots Based on Self-Assembly of Peptide–Porphyrin Conjugates for Antitumor Therapy, *J. Am. Chem. Soc.*, 2017, **139**(5), 1921–1927.

49 R. Zhang, *et al.*, Carrier-Free, Chemophotodynamic Dual Nanodrugs via Self-Assembly for Synergistic Antitumor Therapy, *ACS Appl. Mater. Interfaces*, 2016, **8**(21), 13262–13269.

50 Q. Zhang, *et al.*, Tumor Microenvironment Activated Chemodynamic–Photodynamic Therapy by Multistage Self-Assembly Engineered Protein Nanomedicine, *Adv. Funct. Mater.*, 2022, **32**(17), 2112251.

51 H. Xiang, *et al.*, Self-assembled organic nanomedicine enables ultrastable photo-to-heat converting theranostics in the second near-infrared biowindow, *Nat. Commun.*, 2021, **12**(1), 218.

52 L. Lu, *et al.*, Constructing nanocomplexes by multicomponent self-assembly for curing orthotopic glioblastoma with synergistic chemo-photothermal therapy, *Biomaterials*, 2021, **279**, 121193.

53 Y. Li, *et al.*, Chemotherapeutic drug-photothermal agent co-self-assembling nanoparticles for near-infrared fluorescence and photoacoustic dual-modal imaging-guided chemo-photothermal synergistic therapy, *J. Controlled Release*, 2017, **258**, 95–107.

54 L. Huang, *et al.*, Quantitative self-assembly of photoactivatable small molecular prodrug cocktails for safe and potent cancer chemo-photodynamic therapy, *Nano Today*, 2021, **36**, 101030.

55 Y. Guo, *et al.*, A Small Molecule Nanodrug by Self-Assembly of Dual Anticancer Drugs and Photosensitizer for Synergistic near-Infrared Cancer Theranostics, *ACS Appl. Mater. Interfaces*, 2017, **9**(50), 43508–43519.

56 C. Cui, *et al.*, A generic self-assembly approach towards phototheranostics for NIR-II fluorescence imaging and phototherapy, *Acta Biomater.*, 2022, **140**, 601–609.

57 Y. Gao, *et al.*, Selectively enhancing radiosensitivity of cancer cells via in situ enzyme-instructed peptide self-assembly, *Acta Pharm. Sin. B*, 2020, **10**(12), 2374–2383.

58 A. Arul, *et al.*, Fabrication of self-assembled nanostructures for intracellular drug delivery from diphenylalanine analogues with rigid or flexible chemical linkers, *Nanoscale Adv.*, 2021, **3**(21), 6176–6190.

59 J. Song, *et al.*, Double-Layered Plasmonic–Magnetic Vesicles by Self-Assembly of Janus Amphiphilic Gold–Iron (II,III) Oxide Nanoparticles, *Angew. Chem., Int. Ed.*, 2017, **56**(28), 8110–8114.

60 A. Nandi, *et al.*, Cisplatin-induced self-assembly of graphene oxide sheets into spherical nanoparticles for damaging sub-cellular DNA, *Chem. Commun.*, 2017, **53**(8), 1409–1412.

61 X. Han, *et al.*, A hierarchical carbon Fiber@MXene@ZnO core-sheath synergistic microstructure for efficient microwave absorption and photothermal conversion, *Carbon*, 2021, **183**, 872–883.

62 B. L. Li, *et al.*, Directing Assembly and Disassembly of 2D MoS2 Nanosheets with DNA for Drug Delivery, *ACS Appl. Mater. Interfaces*, 2017, **9**(18), 15286–15296.

63 B. Zhang and T. Cui, High-performance and low-cost lung cancer sensor array based on self-assembled graphene. in 2015 28th IEEE International Conference on Micro Electro Mechanical Systems (MEMS). 2015.

64 C. Lan, *et al.*, Self-assembled nanoporous graphene quantum dot-Mn3O4 nanocomposites for surface-enhanced Raman scattering based identification of cancer cells, *RSC Adv.*, 2017, **7**(30), 18658–18667.

65 D. Zhang, *et al.*, The design of Janus black phosphorus quantum dots@metal–organic nanoparticles for simultaneously enhancing environmental stability and photodynamic therapy efficiency, *Mater. Chem. Front.*, 2019, **3**(4), 656–663.

66 M. Liu, *et al.*, In situ assembly of magnetic nanocrystals/graphene oxide nanosheets on tumor cells enables efficient cancer therapy, *Nano Res.*, 2020, **13**(4), 1133–1140.

67 P. Mandal, *et al.*, Time-dependent self-assembly of magnetic particles tethered branched block copolymer for potential biomedical application, *Appl. Surf. Sci.*, 2020, **527**, 146649.

68 L. L. Osorno, *et al.*, Review of Contemporary Self-Assembled Systems for the Controlled Delivery of Therapeutics in Medicine, *Nanomaterials*, 2021, **11**(2), 4–6.

69 K. A. Athanasiou, *et al.*, Self-Organization and the Self-Assembling Process in Tissue Engineering, *Annu. Rev. Biomed. Eng.*, 2013, **15**, 115–136.

70 G. A. Ozin, *et al.*, Nanofabrication by self-assembly, *Mater. Today*, 2009, **12**(5), 12–23.

71 R. Thiruvengadathan, *et al.*, Nanomaterial processing using self-assembly-bottom-up chemical and biological approaches, *Rep. Prog. Phys.*, 2013, **76**(6), 066501.

72 T. Misteli, The concept of self-organization in cellular architecture, *J. Cell Biol.*, 2001, **155**(2), 181–185.

73 B. Zhang, Chapter 5 - Principles, Methods, Formation Mechanisms, and Structures of Nanomaterials Prepared via Self-Assembly, in *Physical Fundamentals of Nanomaterials*, ed. B. Zhang, William Andrew Publishing, Boston, 2018, pp. 177–210.

74 D. Philp and J. F. Stoddart, Self-assembly in natural and unnatural systems, *Angew. Chem., Int. Ed. Engl.*, 1996, **35**(11), 1154–1196.

75 S. Yadav, A. K. Sharma and P. Kumar, Nanoscale Self-Assembly for Therapeutic Delivery, *Front. Bioeng. Biotechnol.*, 2020, **8**, 2–16.

76 A. H. Gröschel and A. H. E. Müller, Self-assembly concepts for multicompartment nanostructures, *Nanoscale*, 2015, **7**(28), 11841–11876.

77 M. Whitesides George and M. Boncheva, Beyond molecules: Self-assembly of mesoscopic and macroscopic components, *Proc. Natl. Acad. Sci. U. S. A.*, 2002, **99**(8), 4769–4774.

78 R. Klajn, J. M. Bishop Kyle and A. Grzybowski Bartosz, Light-controlled self-assembly of reversible and irreversible nanoparticle suprastructures, *Proc. Natl. Acad. Sci. U. S. A.*, 2007, **104**(25), 10305–10309.

79 G. F. Swiegers, S. Balakrishnan and J. Huang, Assemblies and Self-Assembly, in *Reference Module in Chemistry, Molecular Sciences and Chemical Engineering*, 2016, Elsevier.

80 Y.-P. Pang, How neocarcerand Octacid4 self-assembles with guests into irreversible noncovalent complexes and what accelerates the assembly, *Commun. Chem.*, 2022, **5**(1), 9.

81 H. H. Gatzen, V. Saile and J. Leuthold, Nanofabrication by Self-Assembly, in *Micro and Nano Fabrication: Tools and Processes*, ed. H. H. Gatzen, V. Saile and J. Leuthold, Springer Berlin Heidelberg, Berlin, Heidelberg, 2015, pp. 409–423.

82 B. Ziaie, A. Baldi and M. Z. Atashbar, Introduction to Micro/Nanofabrication, in *Springer Handbook of Nanotechnology*, ed. B. Bhushan, 2004, Springer Berlin Heidelberg, Berlin, Heidelberg, p. 147–184.

83 Y. Zheng, 3 - Fabrication on bioinspired surfaces, in *Bioinspired Design of Materials Surfaces*, ed. Y. Zheng, Elsevier, 2019, pp. 99–146.

84 K. Ramasamy and A. Gupta, Routes to self-assembly of nanorods, *J. Mater. Res.*, 2013, **28**(13), 1761–1776.

85 Z. Nie, A. Petukhova and E. Kumacheva, Properties and emerging applications of self-assembled structures made from inorganic nanoparticles, *Nat. Nanotechnol.*, 2010, **5**(1), 15–25.

86 A. B. Cook and T. D. Clemons, Bottom-Up versus Top-Down Strategies for Morphology Control in Polymer-Based Biomedical Materials, *Adv. NanoBiomed Res.*, 2022, **2**(1), 2100087.

87 A. Bashir*et al.*, *Chapter 3 - Interfaces and surfaces*, in *Chemistry of Nanomaterials*, ed. T. I. Awan, A. Bashir and A. Tehseen, 2020, Elsevier. p. 51–87.

88 E. V. Amadi, A. Venkataraman and C. Papadopoulos, Nanoscale self-assembly: concepts, applications and challenges, *Nanotechnology*, 2022, **33**(13), 132001.

89 V. I. Timonen Jaakko, *et al.*, Switchable Static and Dynamic Self-Assembly of Magnetic Droplets on Superhydrophobic Surfaces, *Science*, 2013, **341**(6143), 253–257.

90 F. Martínez-Pedrero, *et al.*, Static and Dynamic Self-Assembly of Pearl-Like-Chains of Magnetic Colloids Confined at Fluid Interfaces, *Small*, 2021, **17**(25), 2101188.

91 M. A. Boles, M. Engel and D. V. Talapin, Self-assembly of colloidal nanocrystals: From intricate structures to functional materials, *Chem. Rev.*, 2016, **116**(18), 11220–11289.

92 A. F. Demirors and L. Alison, Electric field assembly of colloidal superstructures, *J. Phys. Chem. Lett.*, 2018, **9**(15), 4437–4443.

93 M. Grzelczak, *et al.*, Directed self-assembly of nanoparticles, *ACS Nano*, 2010, **4**(7), 3591–3605.

94 Z. Chai, A. Childress and A. A. Busnaina, Directed assembly of nanomaterials for making nanoscale devices and structures: Mechanisms and applications, *ACS Nano*, 2022, **16**(11), 17641–17686.

95 X. Li, Z. Wang and H. Xia, Ultrasound reversible response nanocarrier based on sodium alginate modified mesoporous silica nanoparticles, *Front. Chem.*, 2019, **7**, 59.

96 L. Isa, *et al.*, Particle lithography from colloidal self-assembly at liquid– liquid interfaces, *ACS Nano*, 2010, **4**(10), 5665–5670.

97 X. Fu, *et al.*, Top-down fabrication of shape-controlled, monodisperse nanoparticles for biomedical applications, *Adv. Drug Delivery Rev.*, 2018, **132**, 169–187.

98 R. A. Hughes, E. Menumerov and S. Neretina, When lithography meets self-assembly: a review of recent advances in the directed assembly of complex metal nanostructures on planar and textured surfaces, *Nanotechnology*, 2017, **28**(28), 282002.

99 Z. Cui and Z. Cui, *Nanofabrication by Self-Assembly. Nanofabrication: Principles, Capabilities and Limits*, 2008, pp. 295–333.

100 Z. Li, Q. Fan and Y. Yin, Colloidal self-assembly approaches to smart nanostructured materials, *Chem. Rev.*, 2021, **122**(5), 4976–5067.

101 L. Zhao and X. Yan, Supramolecular self-assembly: A facile way to fabricate protein and peptide nanomaterials, in *Artificial Protein and Peptide Nanofibers*, Elsevier, 2020, pp. 3–21.

102 Y. Lin and C. Mao, Bio-inspired supramolecular self-assembly towards soft nanomaterials, *Front. Mater. Sci.*, 2011, **5**, 247–265.

103 J. J. Richardson, *et al.*, Innovation in layer-by-layer assembly, *Chem. Rev.*, 2016, **116**(23), 14828–14867.

104 K. Ariga, *et al.*, Layer–by–layer assembly: recent progress from layered assemblies to layered nanoarchitectonics, *Chem. – Asian J.*, 2019, **14**(15), 2553–2566.

105 T. Liu, *et al.*, Biomedical applications of layer–by–layer self–assembly for cell encapsulation: Current status and future perspectives, *Adv. Healthcare Mater.*, 2019, **8**(1), 1800939.

106 C. J. Brinker, Evaporation-induced self-assembly: functional nanostructures made easy, *MRS Bull.*, 2004, **29**(9), 631–640.

107 D. Grosso, *et al.*, Fundamentals of mesostructuring through evaporation–induced self–assembly, *Adv. Funct. Mater.*, 2004, **14**(4), 309–322.

108 K. Ariga, *et al.*, 25th Anniversary article: What can be done with the Langmuir–Blodgett method? Recent developments and its critical role in materials science, *Adv. Mater.*, 2013, **25**(45), 6477–6512.

109 J. Polte, Fundamental growth principles of colloidal metal nanoparticles–a new perspective, *CrystEngComm*, 2015, **17**(36), 6809–6830.

110 T. Hegmann, H. Qi and V. M. Marx, Nanoparticles in liquid crystals: synthesis, self-assembly, defect formation and potential applications, *J. Inorg. Organomet. Polym. Mater.*, 2007, **17**, 483–508.

111 D. Herschlag and M. M. Pinney, Hydrogen Bonds: Simple after All?, *Biochemistry*, 2018, **57**(24), 3338–3352.

112 P. Li, M. R. Ryder and J. F. Stoddart, Hydrogen-Bonded Organic Frameworks: A Rising Class of Porous Molecular Materials, *Acc. Mater. Res.*, 2020, **1**(1), 77–87.

113 S. C. C. van der Lubbe and C. Fonseca Guerra, The Nature of Hydrogen Bonds: A Delineation of the Role of Different Energy Components on Hydrogen Bond Strengths and Lengths, *Chem. – Asian J.*, 2019, **14**(16), 2760–2769.

114 R. P. Sijbesma and E. W. Meijer, Self-assembly of well-defined structures by hydrogen bonding, *Curr. Opin. Colloid Interface Sci.*, 1999, **4**(1), 24–32.

115 F. B. Ilhami, *et al.*, Hydrogen Bond Strength-Mediated Self-Assembly of Supramolecular Nanogels for Selective and Effective Cancer Treatment, *Biomacromolecules*, 2021, **22**(10), 4446–4457.

116 R. Thakuria, N. K. Nath and B. K. Saha, The Nature and Applications of π–π Interactions: A Perspective, *Cryst. Growth Des.*, 2019, **19**(2), 523–528.

117 D. Yang, *et al.*, The π–π stacking-guided supramolecular self-assembly of nanomedicine for effective delivery of antineoplastic therapies, *Nanomedicine*, 2018, **13**(24), 3159–3177.

118 Y. Liang, *et al.*, The effect of π-Conjugation on the self-assembly of micelles and controlled cargo release, *Artif. Cells, Nanomed., Biotechnol.*, 2020, **48**(1), 525–532.

119 J.-H. Deng, *et al.*, π-π stacking interactions: Non-negligible forces for stabilizing porous supramolecular frameworks, *Sci. Adv.*, 2020, **6**(2), eaax9976.

120 G. Caputo and N. Pinna, Nanoparticle self-assembly using π–π interactions, *J. Mater. Chem. A*, 2013, **1**(7), 2370–2378.

121 S. Kawai, *et al.*, van der Waals interactions and the limits of isolated atom models at interfaces, *Nat. Commun.*, 2016, **7**(1), 11559.

122 B. Choi, *et al.*, van der Waals Solids from Self-Assembled Nanoscale Building Blocks, *Nano Lett.*, 2016, **16**(2), 1445–1449.

123 H.-Y. Gao, *et al.*, In-plane van der Waals interactions of molecular self-assembly monolayer, *Appl. Phys. Lett.*, 2015, **106**(8), 081606.

124 J. Hermann, R. A. DiStasio and A. Tkatchenko, First-Principles Models for van der Waals Interactions in Molecules and Materials: Concepts, Theory, and Applications, *Chem. Rev.*, 2017, **117**(6), 4714–4758.

125 T. Morawietz, *et al.*, How van der Waals interactions determine the unique properties of water, *Proc. Natl. Acad. Sci. U. S. A.*, 2016, **113**(30), 8368–8373.

126 H. Duan and K. K. Berggren, Directed self-assembly at the 10 nm scale by using capillary force-induced nanocohesion, *Nano Lett.*, 2010, **10**(9), 3710–3716.

127 H. Huang and E. Ruckenstein, The bridging force between colloidal particles in a polyelectrolyte solution, *Langmuir*, 2012, **28**(47), 16300–16305.

128 C. H. Li and J. L. Zuo, Self–healing polymers based on coordination bonds, *Adv. Mater.*, 2020, **32**(27), 1903762.

129 N. Maldonado and P. Amo-Ochoa, Advances and novel perspectives on colloids, hydrogels, and aerogels based on coordination bonds with biological interest ligands, *Nanomaterials*, 2021, **11**(7), 1865.

130 U. Anand, *et al.*, Hydration layer-mediated pairwise interaction of nanoparticles, *Nano Lett.*, 2016, **16**(1), 786–790.

131 S. L. Thomä, *et al.*, Atomic insight into hydration shells around facetted nanoparticles, *Nat. Commun.*, 2019, **10**(1), 995.

132 Z. Shen, *et al.*, Surface chemistry affects the efficacy of the hydration force between two ZnO $(10\bar{1}0)$ surfaces, *J. Phys. Chem. C*, 2018, **122**(23), 12259–12266.

133 S. F. Tan, *et al.*, Direct observation of interactions between nanoparticles and nanoparticle self-assembly in solution, *Acc. Chem. Res.*, 2017, **50**(6), 1303–1312.

134 X. Li, X. Liu and X. Liu, Self-assembly of colloidal inorganic nanocrystals: nanoscale forces, emergent properties and applications, *Chem. Soc. Rev.*, 2021, **50**(3), 2074–2101.

135 J. W. Ciszek, *et al.*, Assembly of nanorods into designer superstructures: The role of templating, capillary forces, adhesion, and polymer hydration, *ACS Nano*, 2010, **4**(1), 259–266.

136 Y. S. Lee, Self-Assembly at Interfaces, in *Self–Assembly and Nanotechnology*, 2008, pp. 125–147.

137 I. Choi and W. S. Yeo, Self–Assembled Monolayers with Dynamicity Stemming from (Bio) Chemical Conversions: From Construction to Application, *ChemPhysChem*, 2013, **14**(1), 55–69.

138 Q. Feng, *et al.*, Self-Assembly of Gold Nanoparticles Shows Microenvironment-Mediated Dynamic Switching and Enhanced Brain Tumor Targeting, *Theranostics*, 2017, **7**(7), 1875–1889.

139 Y. Tao, *et al.*, Engineered, self-assembled near-infrared photothermal agents for combined tumor immunotherapy and chemo-photothermal therapy, *Biomaterials*, 2014, **35**(24), 6646–6656.

140 Y. Yu, *et al.*, Lysosomal activable Vorinostat carrier-prodrug self-assembling with BPQDs enables photothermal oncotherapy to reverse tumor thermotolerance and metastasis, *Int. J. Pharm.*, 2022, **617**, 121580.

141 C.-Q. Li, *et al.*, A self-assembled nanoplatform based on Ag2S quantum dots and tellurium nanorods for combined chemo-photothermal therapy guided by H_2O_2-activated near-infrared-II fluorescence imaging, *Acta Biomater.*, 2022, **140**, 547–560.

142 S. Georgitsopoulou, *et al.*, Self-assembled Janus graphene nanostructures with high camptothecin loading for increased cytotoxicity to cancer cells, *J. Drug Delivery Sci. Technol.*, 2022, **67**, 102971.

143 L. a. Yan, *et al.*, A Versatile Activatable Fluorescence Probing Platform for Cancer Cells in Vitro and in Vivo Based on Self-Assembled Aptamer/Carbon Nanotube Ensembles, *Anal. Chem.*, 2014, **86**(18), 9271–9277.

144 A. Kolokithas-Ntoukas, *et al.*, Condensed Clustered Iron Oxides for Ultrahigh Photothermal Conversion and In

Vivo Multimodal Imaging, *ACS Appl. Mater. Interfaces*, 2021, **13**(25), 29247–29256.

145 Y. Cao, *et al.*, Gold nanorods/polydopamine-capped hollow hydroxyapatite microcapsules as remotely controllable multifunctional drug delivery platform, *Powder Technol.*, 2020, **372**, 486–496.

146 Z. Wang, *et al.*, Biomimetic nanoflowers by self-assembly of nanozymes to induce intracellular oxidative damage against hypoxic tumors, *Nat. Commun.*, 2018, **9**(1), 3334.

147 D.-K. Ji, *et al.*, Targeted Intracellular Production of Reactive Oxygen Species by a 2D Molybdenum Disulfide Glycosheet, *Adv. Mater.*, 2016, **28**(42), 9356–9363.

148 L. Narashimhan Ramana, R. J. Mudakavi and A. M. Raichur, Self-assembled albumin decorated MoS2 aggregates and photo-stimuli induced geometrical switching for enhanced theranostics applications, *Mater. Adv.*, 2020, **1**(8), 3000–3008.

149 A. Vadivelmurugan, *et al.*, Pluronic F127 self-assembled MoS2 nanocomposites as an effective glutathione responsive anticancer drug delivery system, *RSC Adv.*, 2019, **9**(44), 25592–25601.

150 Y. Zhang, *et al.*, Near-infrared triggered Ti3C2/g-C3N4 heterostructure for mitochondria-targeting multimode photodynamic therapy combined photothermal therapy, *Nano Today*, 2020, **34**, 100919.

151 Y. Cao, *et al.*, N+ implantation induce cytocompatibility of shape-controlled three-dimensional self-assembly graphene, *Nanomedicine*, 2017, **12**(18), 2245–2255.

152 R. K. Thapa, *et al.*, Easy on-demand self-assembly of lateral nanodimensional hybrid graphene oxide flakes for near-infrared-induced chemothermal therapy, *NPG Asia Mater.*, 2017, **9**(8), e416–e416.

153 D. Li, *et al.*, Self-Assembled Hydroxyapatite-Graphene Scaffold for Photothermal Cancer Therapy and Bone Regeneration, *J. Biomed. Nanotechnol.*, 2018, **14**(12), 2003–2017.

154 X. Zhang, *et al.*, Self-assembled thermosensitive luminescent nanoparticles with peptide-Au conjugates for cellular imaging and drug delivery, *Chin. Chem. Lett.*, 2020, **31**(3), 859–864.

155 J. Li, *et al.*, Cycloruthenated Self-Assembly with Metabolic Inhibition to Efficiently Overcome Multidrug Resistance in Cancers, *Adv. Mater.*, 2022, **34**(1), 2100245.

156 Y. Wu, *et al.*, Self-assembled MXene-based Schottky-junction upon Transition metal oxide for regulated tumor microenvironment and enhanced CDT/PTT/MRI activated by NIR irradiation, *Chem. Eng. J.*, 2022, **427**, 131925.

157 B. Zhu, *et al.*, In situ self-assembly of sandwich-like Ti3C2 MXene/gold nanorods nanosheets for synergistically enhanced near-infrared responsive drug delivery, *Ceram. Int.*, 2021, **47**(17), 24252–24261.

158 Y. Huang, *et al.*, Self-Assembly of Multi-nanozymes to Mimic an Intracellular Antioxidant Defense System, *Angew. Chem., Int. Ed.*, 2016, **55**(23), 6646–6650.

159 Y. Zhao, *et al.*, Passivation of Black Phosphorus via Self-Assembled Organic Monolayers by van der Waals Epitaxy, *Adv. Mater.*, 2017, **29**(6), 1603990.

160 C. Qian, *et al.*, Facile preparation of self-assembled black phosphorus-based composite LB films as new chemical gas sensors, *Colloids Surf., A*, 2021, **608**, 125616.

161 S. Azevedo, *et al.*, Advances in carbon nanomaterials for immunotherapy, *Appl. Mater. Today*, 2022, **27**, 101397.

162 X. Q. Wang, F. Gao and X. Z. Zhang, Initiator–loaded gold nanocages as a light–induced free–radical generator for cancer therapy, *Angew. Chem., Int. Ed.*, 2017, **56**(31), 9029–9033.

163 V. Lenders, *et al.*, Biomedical nanomaterials for immunological applications: ongoing research and clinical trials, *Nanoscale Adv.*, 2020, **2**(11), 5046–5089.

164 G. Yang, *et al.*, Degradability and clearance of inorganic nanoparticles for biomedical applications, *Adv. Mater.*, 2019, **31**(10), 1805730.

165 S. Bayda, *et al.*, Inorganic nanoparticles for cancer therapy: a transition from lab to clinic, *Curr. Med. Chem.*, 2018, **25**(34), 4269–4303.

166 R. Mohammadpour, *et al.*, Subchronic and chronic toxicity evaluation of inorganic nanoparticles for delivery applications, *Adv. Drug Delivery Rev.*, 2019, **144**, 112–132.

167 H. Huang, *et al.*, Inorganic nanoparticles in clinical trials and translations, *Nano Today*, 2020, **35**, 100972.

168 W. R. Wagner, *et al.*, *Biomaterials science: an introduction to materials in medicine*, 2020, Academic Press.

169 K. Zarschler, *et al.*, Ultrasmall inorganic nanoparticles: State-of-the-art and perspectives for biomedical applications, *Nanomedicine*, 2016, **12**(6), 1663–1701.

170 P. R. Riley and R. J. Narayan, Recent advances in carbon nanomaterials for biomedical applications: A review, *Curr. Opin. Biomed. Eng.*, 2021, **17**, 100262.

171 M. Mohajeri, B. Behnam and A. Sahebkar, Biomedical applications of carbon nanomaterials: Drug and gene delivery potentials, *J. Cell. Physiol.*, 2019, **234**(1), 298–319.

172 M. Gaur, *et al.*, Biomedical applications of carbon nanomaterials: fullerenes, quantum dots, nanotubes, nanofibers, and graphene, *Materials*, 2021, **14**(20), 5978.

173 M. Jiao, *et al.*, Recent advancements in biocompatible inorganic nanoparticles towards biomedical applications, *Biomater. Sci.*, 2018, **6**(4), 726–745.